

การวิเคราะห์โครงหลังคาเหล็กแบบไม่เชิงเส้นภายใต้การเกิดเพลิงไหม้



นาย ปฐมศ ผาณิตพจมาน

สถาบันวิทยบริการ  
จุฬาลงกรณ์มหาวิทยาลัย

วิทยานิพนธ์นี้เป็นส่วนหนึ่งของการศึกษาตามหลักสูตรปริญญาวิศวกรรมศาสตรมหาบัณฑิต

สาขาวิศวกรรมโยธา ภาควิชาวิศวกรรมโยธา  
คณะวิศวกรรมศาสตร์ จุฬาลงกรณ์มหาวิทยาลัย

ปีการศึกษา 2548

ISBN : 974-17-4331-9

ลิขสิทธิ์ของจุฬาลงกรณ์มหาวิทยาลัย

NONLINEAR ANALYSIS OF STEEL ROOF FRAMES UNDER FIRE



Mr. Pattamad Panedpojaman

สถาบันวิทยบริการ

จุฬาลงกรณ์มหาวิทยาลัย

A Thesis Submitted in Partial Fulfillment of the Requirements  
for the Degree of Master of Engineering Program in Civil Engineering

Department of Civil Engineering

Faculty of Engineering

Chulalongkorn University

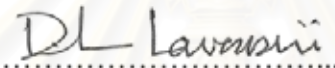
Academic Year 2005

ISBN : 974-17-4331-9

Thesis Title            Nonlinear Analysis of Steel Roof Frames under Fire  
By                         Mr. Pattamad Panedpojaman  
Field of study         Civil Engineering  
Thesis Advisor        Assistant Professor Thanyawat Pothisiri, Ph.D.

---

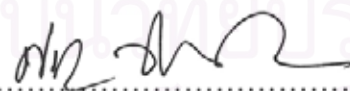
Accepted by the Faculty of Engineering, Chulalongkorn University in  
Partial Fulfillment of Requirements for the Master's Degree

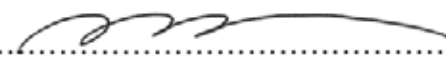
  
..... Dean of Faculty of Engineering  
(Professor Direk Lavansiri , Ph.D.)

THESIS COMMITTEE

  
..... Chairman  
(Professor Thaksin Thepchatri, Ph.D.)

  
..... Thesis Advisor  
(Assistant Professor Thanyawat Pothisiri, Ph.D.)

  
..... Member  
(Mr. Pichaya Chantranuwat)

  
..... Member  
(Assistant Professor Chadchart Sittipunt, Ph.D.)

ปฐมเมศ ภาณิตพจมาน : การวิเคราะห์โครงหลังคาเหล็กแบบไม่เชิงเส้นภายใต้การเกิดเพลิงไหม้  
(NONLINEAR ANALYSIS OF STEEL ROOF FRAMES UNDER FIRE) อาจารย์ที่ปรึกษา :  
ผู้ช่วยศาสตราจารย์ ดร.ธัญวัฒน์ โพธิศิริ, 116 หน้า, ISBN : 974-17-4331-9.

งานวิจัยนี้ศึกษาความสามารถในการทนไฟของโครงสร้างหลังคาเหล็กสำหรับอาคาร โกดังเก็บสินค้า โดยวิธีอิงพฤติกรรม ซึ่งจำลองสถานการณ์การเกิดเพลิงไหม้ต่างๆโดยใช้โปรแกรม Fire Dynamics Simulator (FDS) การจำลองการเกิดเพลิงไหม้พิจารณาให้ตำแหน่งของจุดต้นเพลิง ชนิดของเชื้อเพลิงและความสูงของโครงหลังคาอาคาร โกดังเก็บสินค้าเป็นค่าตัวแปร จากนั้นทำการวิเคราะห์โครงหลังคาแบบไม่เชิงเส้นภายใต้สถานการณ์การเกิดเพลิงไหม้ที่จำลองขึ้นในรูปแบบต่างๆ โดยคำนึงถึงปัจจัยด้านการเปลี่ยนแปลงคุณสมบัติของเหล็กภายใต้การเกิดเพลิงไหม้ทั้งกรณีที่มีและไม่มีกำบังกันไฟ

จากผลการจำลองการเกิดเพลิงไหม้พบว่าชนิดของเชื้อเพลิงเป็นตัวแปรหลักที่ส่งผลต่อพฤติกรรมการเกิดเพลิงไหม้ที่จำลองขึ้น ในด้านการลุกไหม้และการลุกลามของเปลวเพลิง กรณีเชื้อเพลิงพลาสติกให้พฤติกรรมการลามไฟอย่างรวดเร็วเนื่องจากผลการสะท้อนความร้อนจากเปลวเพลิง สำหรับกรณีเชื้อเพลิงไม้การลามไฟเกิดได้ช้า เนื่องจากเป็นผลจากการแผ่รังสีโดยตรงสู่เชื้อเพลิงใกล้เคียง จากผลการศึกษาพบว่าการวิบัติของโครงสร้างเกิดจากสามสาเหตุหลัก ได้แก่ การเพิ่มขึ้นของหน่วยแรงอัด การลดลงของคุณสมบัติเชิงกลของเหล็ก และ ผลกระทบจากแรงเยื้องศูนย์ กรณีเชื้อเพลิงพลาสติกพบว่าระยะเวลาการวิบัติของโครงหลังคาอยู่ระหว่าง 1100-1500 วินาที และ 330-400 วินาที สำหรับกรณีที่มีกำบังกันไฟและไม่มีกำบังกันไฟตามลำดับ กรณีเชื้อเพลิงไม้พบว่าระยะเวลาการวิบัติต่ำสุดที่ 1750 วินาที สำหรับกรณีที่ไม่มีกำบังกันไฟ และระยะเวลาวิบัติสูงสุดมากกว่า 7200 วินาที (ระยะเวลาการจำลองเพลิงไหม้สูงสุด) สำหรับกรณีที่มีกำบังกันไฟ

ผลจากการศึกษานี้สามารถนำมาประยุกต์ใช้ในการประเมินระยะเวลาปลอดภัยในการอพยพจากโครงสร้างที่พิจารณา และใช้เป็นแนวทางสำหรับออกแบบระบบป้องกันไฟที่เหมาะสม รวมทั้งเป็นแนวทางเบื้องต้นในการประเมินความเสี่ยงจากเพลิงไหม้ของโครงสร้างที่มีรูปแบบใกล้เคียงกันตามข้อกำหนดเรื่องความปลอดภัยจากอัคคีภัย

ภาควิชา วิศวกรรมโยธา ลายมือชื่อนิสิต ปฐมเมศ ภาณิตพจมาน  
สาขาวิชา วิศวกรรมโยธา ลายมือชื่ออาจารย์ที่ปรึกษา ธัญวัฒน์  
ปีการศึกษา 2548

# # 4370449021

MAJOR CIVIL ENGINEERING

KEYWORDS : FIRE MODELING / NONLINEAR ANALYSIS / STEEL STRUCTURES

PATTAMAD PANEDPOJAMAN : NONLINEAR ANALYSIS OF STEEL ROOF FRAMES UNDER FIRE. THESIS ADVISOR : ASSISTANT PROFESSOR THANYAWAT POTHISIRI, Ph.D., 116 pp. ISBN : 974-17-4331-9.

The current study investigates the fire resistance of the steel roof structure for a typical warehouse using the performance-based approach. Various fire scenarios are simulated using the Fire Dynamics Simulator (FDS) program. The simulation considers the location of the ignition source, the fuel type and the clearance height of the warehouse as the varying parameters. For each of the modeled fire scenarios, the behavior of the roof structure is examined using nonlinear structural analysis, taking into account the varying properties of steel under fire, with and without fire protection.

Based on the fire modeling results, it is found that the fuel types significantly affect the behavior of the modeled fire in terms of the fire growth and the spread of flames. The plastic storage contents result in a rapid fire growth due to the significant feedback of heat from the flames. The wood storage contents result in a considerably slower fire growth that occurs through direct radiation from the flames to nearby objects. It is observed that the failure of the roof structure is due to three key factors: the increasing axial compression; the significant drop of the mechanical properties of steel; and the  $P-\Delta$  effects. For the cases of plastic storage contents, the time to failure is in the range of 1100-1500 seconds and 330-400 seconds for the roof structure with and without fire protection, respectively. For the cases of the wood storage contents, the minimum time to failure is 1750 seconds for the roof structure without fire protection and the maximum time to failure is longer than 7200 seconds (the maximum burning time) when the roof structure is fire-protected.

The outcome of the current study can be used to assess the safe egress time for the structure under consideration, to establish a guideline for proper design of the fire protection systems, as well as to set an initial step towards the fire risk assessment of similar structures in accordance with the national fire safety regulations.

Department CIVIL ENGINEERING  
 Field of study CIVIL ENGINEERING  
 Academic year 2005

Student's signature

Advisor's signature

ฐกรณ์ พานิชิต ๒๕๔๗ ๑๔  
 Thanyawat Pothisiri

## ACKNOWLEDGEMENTS

The author wishes to express his deep appreciation and sincere gratitude to his thesis advisor, Assistant Professor Thanyawat Pothisiri, Ph.D., for his guidance, assistance and constant support throughout his study at Chulalongkorn University. Grateful acknowledgements are due to Professor Thaksin Thepchatri, Ph.D., Mr. Pichaya Chantranuwat and Associate Professor Chadchart Sittipunt, Ph.D. for their invaluable comments and recommendations. Special thanks are also extended to those who have helped directly and indirectly in the preparation of this thesis. Finally, the author would like to thank his parents for their love and encouragement.



สถาบันวิทยบริการ  
จุฬาลงกรณ์มหาวิทยาลัย

## TABLE OF CONTENTS

	Page
Abstract (Thai) .....	iv
Abstract (English) .....	v
Acknowledgements .....	vi
Table of Contents .....	vii
List of Tables .....	ix
List of Figures .....	x
<b>CHAPTER I: INTRODUCTION</b> .....	<b>1</b>
1.1 Introduction.....	1
1.2 Literature Review.....	1
1.3 Research Objectives.....	3
1.4 Scope of Research Works.....	3
1.5 Research Methodology .....	4
<b>CHAPTER II: THEORETICAL BACKGROUND</b> .....	<b>6</b>
2.1 Introduction.....	6
2.2 Fire Modeling.....	6
2.3 Fire Modeling using FDS Program.....	8
2.3.1 Combustion Analysis .....	8
2.3.2 Boundary Condition Analysis .....	10
2.3.3 Radiation Transport Analysis .....	11
2.3.4 Fire Modeling Parameters .....	12
2.4 Calculation of Steel Temperature .....	13
2.4.1 Steel without Fire Protection .....	14
2.4.2 Steel with Fire Protection.....	15
2.5 Variation of Steel Properties with Temperature.....	16
2.5.1 Variation of Mechanical Properties of Steel with Temperature.....	17
2.5.2 Variation of Thermal Properties of Steel with Temperature.....	18



2.6 Nonlinear Finite Element Analysis of Steel Frames Subjected to Varying Temperatures.....	18
2.7 ANSI/AISC 360-05 Buckling Analysis.....	25
<b>CHAPTER III: PRELIMINARY SIMULATION STUDIES .....</b>	<b>29</b>
3.1 Introduction.....	29
3.2 Fire Tests of the Roofing System for the Passenger Terminal Building of the Second Bangkok International Airport.....	29
3.3 Analysis of Heat Transfer for Steel Sections: Lumped Mass Approach and Finite Element Method.....	38
<b>CHAPTER IV: SIMULATION STUDIES .....</b>	<b>44</b>
4.1 Introduction.....	44
4.2 Fire Modeling Parameters .....	44
4.3 Structural Modeling Parameters and Criteria for Structural Analysis.....	48
4.4 Fire Modeling Results .....	55
4.5 Structural Analysis .....	76
<b>CHAPTER V: CONCLUSIONS .....</b>	<b>103</b>
<b>REFERENCES.....</b>	<b>104</b>
<b>APPENDIX: FDS RESULTS .....</b>	<b>106</b>
<b>VITA.....</b>	<b>116</b>



## LIST OF TABLES

Table 2.1	Mechanical properties of A36 steel with respect to varying temperature.....	17
Table 2.2	Formulas of stress components for rectangular and pipe sections.....	24
Table 2.3	Limiting width-thickness ratios for compression elements.....	25
Table 3.1	Varying input parameters for FDS model.....	33
Table 3.2	Various steel sections in the structural model.....	39
Table 4.1	Thermal properties of wood and plastic content .....	44
Table 4.2	Various fire scenarios investigated in the simulation studies .....	46
Table 4.3	Section properties for buckling calculations .....	50
Table 4.4	Buckling strength and plastic moment of pipe sections.....	51
Table 4.5	Buckling strength and moment of purlins sections.....	52
Table 4.6	Summary of structural failure mode and time .....	102

## LIST OF FIGURES

Figure 1.1	Framework of research.....	5
Figure 2.1	Subdivision of physical space in CFD model.....	9
Figure 2.2	Input parameters in fire modeling.....	13
Figure 2.3	Nonlinear structural analysis process.....	19
Figure 2.4	Degrees of freedom of the circular pipe element.....	20
Figure 2.5	Displacements of the circular pipe element.....	20
Figure 2.6	Stress components for the circular pipe element.....	24
Figure 3.1	Simulated membrane roofing system.....	30
Figure 3.2	Fire test setup .....	30
Figure 3.3	Location of thermocouples on the bottom layer of the roofing system and above the wood crib.....	31
Figure 3.4	FDS model of fire test.....	31
Figure 3.5	Fire growths from FDS model.....	32
Figure 3.6	Fire test temperature measurements vs. FDS results.....	32
Figure 3.7	FDS temperature results for scenario A.....	35
Figure 3.8	FDS temperature results for scenario B.....	35
Figure 3.9	FDS temperature results for scenario C.....	36
Figure 3.10	FDS temperature results for scenario D.....	36
Figure 3.11	FDS temperature results for scenario E.....	37
Figure 3.12	FDS temperature results for scenario F.....	37
Figure 3.13	Location of point A .....	39
Figure 3.14	2D finite element models for different sections with and without fire protection.....	39
Figure 3.15	Comparison of the variation of steel temperatures with respect to time for Cases II-AL and II-BL using the lumped mass approach and 2D finite element models.....	40
Figure 3.16	3D finite element model .....	41
Figure 3.17	Comparison of the variation of temperatures for steel without fire protection with respect to time for Cases II-AL and II-BL using the lumped mass approach and 3D finite element models.....	42

Figure3.18	Comparison of the variation of temperatures for steel with fire protection with respect to time for Cases II-AL and II-BL using the lumped mass approach and 3D finite element models.....	43
Figure 4.1	FDS simulated warehouse.....	45
Figure 4.2	Various locations of the ignition source.....	45
Figure 4.3	Coding representation of varying parameters .....	46
Figure 4.4	Grids of FDS simulated warehouse .....	47
Figure 4.5	FDS model of the roof frames.....	47
Figure 4.6	Roof structure model of the typical warehouse.....	49
Figure 4.7	Element and node of the structure model.....	50
Figure 4.8	Flame spread and enclosure temperature at different time steps for Case II-AL.....	56
Figure 4.9	Flame spread and enclosure temperature at different time steps for Case II-BL.....	57
Figure 4.10	Heat release rate of the plastic and wood fuel.....	58
Figure 4.11	Zone areas in the structure plan.....	58
Figure 4.12	Temperature distribution for Case I-AL.....	60
Figure 4.13	Temperature distribution for Case II-AL.....	61
Figure 4.14	Temperature distribution for Case III-AL.....	62
Figure 4.15	Temperature distribution for Case IV-AL.....	63
Figure 4.16	Temperature distribution for Case I-AH.....	64
Figure 4.17	Temperature distribution for Case II-AH.....	65
Figure 4.18	Temperature distribution for Case Iii-AH.....	66
Figure 4.19	Temperature distribution for Case IV-AH.....	67
Figure 4.20	Temperature distribution for Case I-BL.....	68
Figure 4.21	Temperature distribution for Case II-BL.....	69
Figure 4.22	Temperature distribution for Case III-BL.....	70
Figure 4.23	Temperature distribution for Case IV-BL.....	71
Figure 4.24	Temperature distribution for Case I-BH.....	72
Figure 4.25	Temperature distribution for Case II-BH.....	73
Figure 4.26	Temperature distribution for Case Iii-BH.....	74

Figure 4.27	Temperature distribution for Case IV-BH.....	75
Figure 4.28	Location of the ignition source for Case I-AHP.....	77
Figure 4.29	Location of member failure and temperature distribution at different time steps for Case I-AHP.....	78
Figure 4.30	Distribution of stresses and bending moments at different time steps for Case I-AHP.....	79
Figure 4.31	Longitudinal and transverse thermal expansion of the roof structure for Case I-AHP at 1400 seconds.....	80
Figure 4.32	P- $\Delta$ effects for the main roof frame.....	80
Figure 4.33	Variation of reaction in $X$ -direction at pin supports of the main roof frames with respect to temperature for Case I-AHP.....	80
Figure 4.34	Sequence of failure for the structural members and temperature distribution of the structure at failure for Case I-ALP.....	81
Figure 4.35	Sequence of failure for the structural members and temperature distribution of the structure at failure for Case I-BLU.....	81
Figure 4.36	Sequence of failure for the structural members and temperature distribution of the structure at failure for Case I-AHU.....	82
Figure 4.37	Sequence of failure for the structural members and temperature distribution of the structure at failure for Case I-ALU.....	82
Figure 4.38	The sequence of the failure for the structural members and the temperature distribution of the structure at 7200 seconds for Case I-BHP.....	83
Figure 4.39	The sequence of the failure for the structural members and the temperature distribution of the structure at 7200 seconds for Case I-BHU.....	83
Figure 4.40	The sequence of the failure for the structural members and the temperature distribution of the structure at 7200 seconds for Case I-BLP.....	83
Figure 4.41	Location of the ignition source for Case II-AHP.....	84
Figure 4.42	Location of member failure and temperature distribution at different time steps for Case II-AHP.....	85
Figure 4.43	Distribution of axial stresses and bending moments at different time steps for Case II-AHP.....	86

Figure 4.44	Sequence of failure for the structural members and temperature distribution of the structure at failure for Case II-ALP.....	87
Figure 4.45	Sequence of failure for the structural members and temperature distribution of the structure at failure for Case II-AHU.....	87
Figure 4.46	Sequence of failure for the structural members and temperature distribution of the structure at failure for Case II-BHU .....	87
Figure 4.47	Sequence of failure for the structural members and temperature distribution of the structure at failure for Case II- BLU.....	88
Figure 4.48	Sequence of failure for the structural members and temperature distribution of the structure at failure for Case II-ALU.....	88
Figure 4.49	The sequence of the failure for the structural members and the temperature distribution of the structure at 7200 seconds for Case II-BHP.....	89
Figure 4.50	The sequence of the failure for the structural members and the temperature distribution of the structure at 7200 seconds for Case II-BLP .....	89
Figure 4.51	Location of the ignition source for Case III-AHP.....	90
Figure 4.52	Location of member failure and temperature distribution at different time steps for Case III-AHP.....	91
Figure 4.53	Distribution of axial stresses and bending moments at different time steps for Case III-AHP.....	92
Figure 4.54	Sequence of failure for the structural members and temperature distribution of the structure at failure for Case III-ALP .....	93
Figure 4.55	Sequence of failure for the structural members and temperature distribution of the structure at failure for Case III-AHU .....	93
Figure 4.56	Sequence of failure for the structural members and temperature distribution of the structure at failure for Case III-ALU .....	93
Figure 4.57	Sequence of failure for the structural members and temperature distribution of the structure at failure for Case III-BHU .....	94
Figure 4.58	Sequence of failure for the structural members and temperature distribution of the structure at failure for Case III-BLU .....	94

Figure 4.59	The sequence of the failure for the structural members and the temperature distribution of the structure at 7200 seconds for Case III-BHP .....	95
Figure 4.60	The sequence of the failure for the structural members and the temperature distribution of the structure at 7200 seconds for Case III-BLP.....	95
Figure 4.61	Location of the ignition source for Case IV-AHP.....	96
Figure 4.62	Location of member failure and temperature distribution at different time steps for Case IV-AHP.....	97
Figure 4.63	Distribution of axial stresses and bending moments at different time steps for Case IV-AHP.....	98
Figure 4.64	Sequence of failure for the structural members and temperature distribution of the structure at failure for Case IV-ALU.....	99
Figure 4.65	Sequence of failure for the structural members and temperature distribution of the structure at failure for Case IV-AL.....	99
Figure 4.66	Sequence of failure for the structural members and temperature distribution of the structure at failure for Case IV-BHU.....	100
Figure 4.67	Sequence of failure for the structural members and temperature distribution of the structure at failure for Case IV-BLU.....	100
Figure 4.68	The sequence of the failure for the structural members and the temperature distribution of the structure at 7200 seconds for Case IV-BHP .....	101
Figure 4.69	The sequence of the failure for the structural members and the temperature distribution of the structure at 7200 seconds for Case IV-BLP .....	101



# CHAPTER I

## INTRODUCTION

### 1.1 Introduction

The use of structural steel sections in construction has continuously increased because of the advantages of steel in terms of short erection time as well as high ductility and strength/weight ratio. The types of structures in which the structural steel sections are typically used include long-span bridges and roofs for industrial buildings. Even with the increasing popularity, steel structures have been well known to suffer from exposure to high temperature. Under the high-temperature conditions (i.e., fire), certain properties of the structural steel, e.g. the yield and the ultimate strength, Young's modulus, etc., would drop significantly while the coefficient of expansion would simultaneously increase. This poses a direct threat to the load-carrying capacity of the steel structures that are designed to be used in the normal temperature conditions, or unprotected steel structures.

To design structures for fire resistance using the performance-based approach—as an alternative to the traditional prescriptive requirement—fire modeling is the key to obtaining the design parameters. Fire modeling depends up on various factors, such as fuel load and location, building geometry, etc., which are crucial to understanding the actual structural response under the actual fire in addition to the standard testing procedures (i.e. ASTM-E119).

In the current study, specific fire scenarios for a typical warehouse with a steel roof structure is simulated in order to assess the safe egress time from the structure prior to its failure. It is expected that the outcome of the analysis can more or less be used to set an initial step towards fire risk assessment of similar structures in accordance with the national fire regulations.

### 1.2 Literature Review

Gilvery and Dexter (1997) have investigated the possibility of using a computer program to compute the fire resistance time and the load capacity of certain structures subjected to fire, instead of conducting the full-scale furnace tests. The key objective was to determine whether computer modeling could accurately predict the behavior of the structural members under fire, and therefore to save the cost of testing. A range of possible approaches—from simple calculations to sophisticated numerical simulations—were evaluated. Simple calculations were found to be sufficient for the structural members with uniform temperature distribution. For the members with non-uniform temperature distribution, sophisticated computer modeling is required.



Feeney (1998) has examined the design of a multistory steel-frame building without applying protective coatings, using the performance-based design. In this study, the background on loadings was provided from a structural perspective and the fire loading was treated in a similar way. A detailed description was given to determine the maximum steel temperatures during a fire using the ISO fire and a 'real' fire as determined from the Annex to Eurocode 1. The structural performance was evaluated based on the effects of the increasing temperature on the steel strength, load sharing between members of the structure and the design load likely to be present during a fire. A case study of an apartment building in Auckland was illustrated to estimate the loads and temperatures during a fire and the expected strength. A hotel building in Auckland was also examined. It was shown that the performance-based design can eliminate the requirements of passive protection, thus reducing the cost of the building. Nonetheless, the maximum temperature of steel was found to be within 2 °C of the limiting temperature which is not very conclusive given the assumptions made and variability of steel beam sizes and in-place properties.

Milke (1999) has provided a background on the requirements in which the structural members must uphold during a fire. The fire exposure to the structural members needs to be characterized and the heat transfer coefficients and temperature needs to be specified for different scenarios. The properties of steel at elevated temperatures can change from that of the ambient conditions and this affects the thermal response, and the structural analysis. Included in this paper is an overview of the heat transfer and structural analysis methods including moment analyses for beams and slabs and stability analyses for columns and walls.

Quintier *et al.* (2002) have examined the temperature of the steel rods in the World Trade Center towers subjected to a fire based on the building ventilation factor. The CIB correlation was used for the fire. Conduction analyses were performed taking into account the varying properties of steel and insulation. A structural failure model was described based on compression buckling of the steel rods due to a reduction of Young's modulus. The time to failure or incipient collapse of the floors in both towers was computed for WTC 1 (north) and for WTC 2 (south), compared to the actual collapse time from the aircraft impact.

Sakumoto *et al.* (2002) have investigated analytically the fire resistance of the World Trade Center steel frames and the precautions to be taken in designing skyscrapers. In the analysis, the temperature increase of the steel columns (perimeter and core columns) and the floor trusses of the World Trade Center, when subjected to heating by hydrocarbon fire and standard fire, was calculated for the cases in which the steel members were adequately fire-protected and unprotected (or in case the fire protection was blown off), respectively. The fire resistance of these steel members was also verified by a thermal deformation analysis. The analysis revealed that the floor trusses, even with or without fire protection, experienced a temperature increase at a more rapid pace, inducing restraints upon thermal deformation and thereby causing the steel members to buckle and eventually leading to the failure of the floor trusses at a relatively low temperature. The use of steel with superior heat resistance was recommended to improve the fire resistance

of the steel frames. This does not mean that the fire protection can be deleted, but that given the same or similar protection, the length of time that the steel can tolerate fire is extended. Or, if the fire protection system is destroyed, the unprotected steel will be able to sustain a longer survival time.

### **1.3 Research Objectives**

The key objective of this research is to investigate the fire resistance of the steel roof structures for industrial warehouses. A typical warehouse is employed herein as a case study to provide the key insight to the structural behavior under fire. The investigation adopts the performance-based approach whereby fire is simulated to represent the actual fire incidents and the structure is analyzed under the varying temperature conditions resulted from the modeled fire.

The objectives of the current research can be summarized as follows:

- 1.3.1 To examine the use of fire modeling to represent the actual fire incidents and the structural performance under fire.
- 1.3.2 To investigate the factors affecting the temperature variation within a specified enclosure in fire modeling.
- 1.3.3 To investigate the behavior of a specified steel roof structure of a typical warehouse for the cases in which the steel members are fire-protected and unprotected.
- 1.3.4 To evaluate the fire resistance of the specified steel roof structure.

The outcome of the current research is expected to help understand the behavior of the steel roof structure of a typical warehouse under various fire scenarios and recognize the fire hazards in order to improve the fire protection system of similar warehouses. Furthermore, the framework of this research can more or less be used as a guideline towards fire risk assessment of similar structures in accordance with the national fire safety regulations.

### **1.4 Scope of Research Works**

The current research is aimed to investigate the effect of fire upon a specific steel roof frame, with and without fire protection, of a typical warehouse. The structural analysis is performed using a nonlinear finite element method by incorporating the fire loads from fire modeling. Because of the limitations of the computer software used in fire modeling, certain assumptions on the parameters of the modeled fire are adopted as well as the assumptions on the temperature distribution and heat transfer of the structural members from the surrounding fire. The assumptions employed in the current study are listed below:

- 1.4.1 For the current study, fire is modeled by using the Fire Dynamic Simulator (FDS) program, which adopts the computational fluid dynamics (CFD) model of fire-driven fluid flow.
- 1.4.2 The current study investigates the effects on the variation of the following parameters in fire modeling:
- Fuel types (i.e., warehouse contents), ranging from plastics (fast growing fire) to woods (slow growing fire)
  - The clearance height of the roof structure above ground in the range of 8 – 10 meters
  - The source of ignition (location)
- The variation of each of these parameters essentially characterizes the distinct fire scenarios.
- 1.4.3 The comparison of the structural performance under different fire scenarios is based upon the same initiating time line, i.e. the instant in which the fuel reaches its flaming point. This is done through the modification of the source of ignition to allow the fuel to become flammable instantly.
- 1.4.5 The FDS output for the current study is mainly the temperature distribution of air inside the specified enclosure. To model the heat transfer from air to the structural steel members, the lumped mass approach is employed.
- 1.4.6 The specified steel roof structure is analyzed under the different fire scenarios taking into account the effect of sustained dead loads and the changes in the mechanical properties of steel, i.e. Young's modulus, tensile strength, and coefficient of expansion.
- 1.4.7 The Newton-Raphson iterative method is used to solve the nonlinear equations in the structural analyses.

## 1.5 Research Methodology

In order to understand the behavior of fire as well as the behavior of the steel roof structure subjected to fire, the current research adopts the FDS program to simulate different fire scenarios and employs the nonlinear finite element method to analyze the structure. The framework of the current research can be illustrated schematically in Figure 1.1. The process shown in Figure 1.1 can be summarized as follows:

- 1.5.1 Simulate the various fire scenarios using the FDS program. The various parameters, e.g. enclosures/openings, ventilation, fuel types and locations, ignition sources, etc. are taken into account in fire modeling.
- 1.5.2 Run the FDS program to obtain the air temperature distribution within the specified enclosure (i.e., a typical warehouse).
- 1.5.3 Analyze the transfer of heat into the members of the steel roof structure due to the rising temperature of the surrounding fire.
- 1.5.4 Create a finite-element model for the steel roof structure taking into account the various parameters, e.g. degrees of freedom, connections, loading and support conditions, etc.

- 1.5.5 Create the incremental temperature input for each structural member in the finite-element model.
- 1.5.6 Perform a nonlinear structural analysis of the steel roof structure subjected to the incremental temperature input under sustained loading.
- 1.5.7 Examine the structural analysis results in terms of failure mode and time for each of the distinct fire scenarios under consideration.
- 1.5.8 Discussion and conclusion.

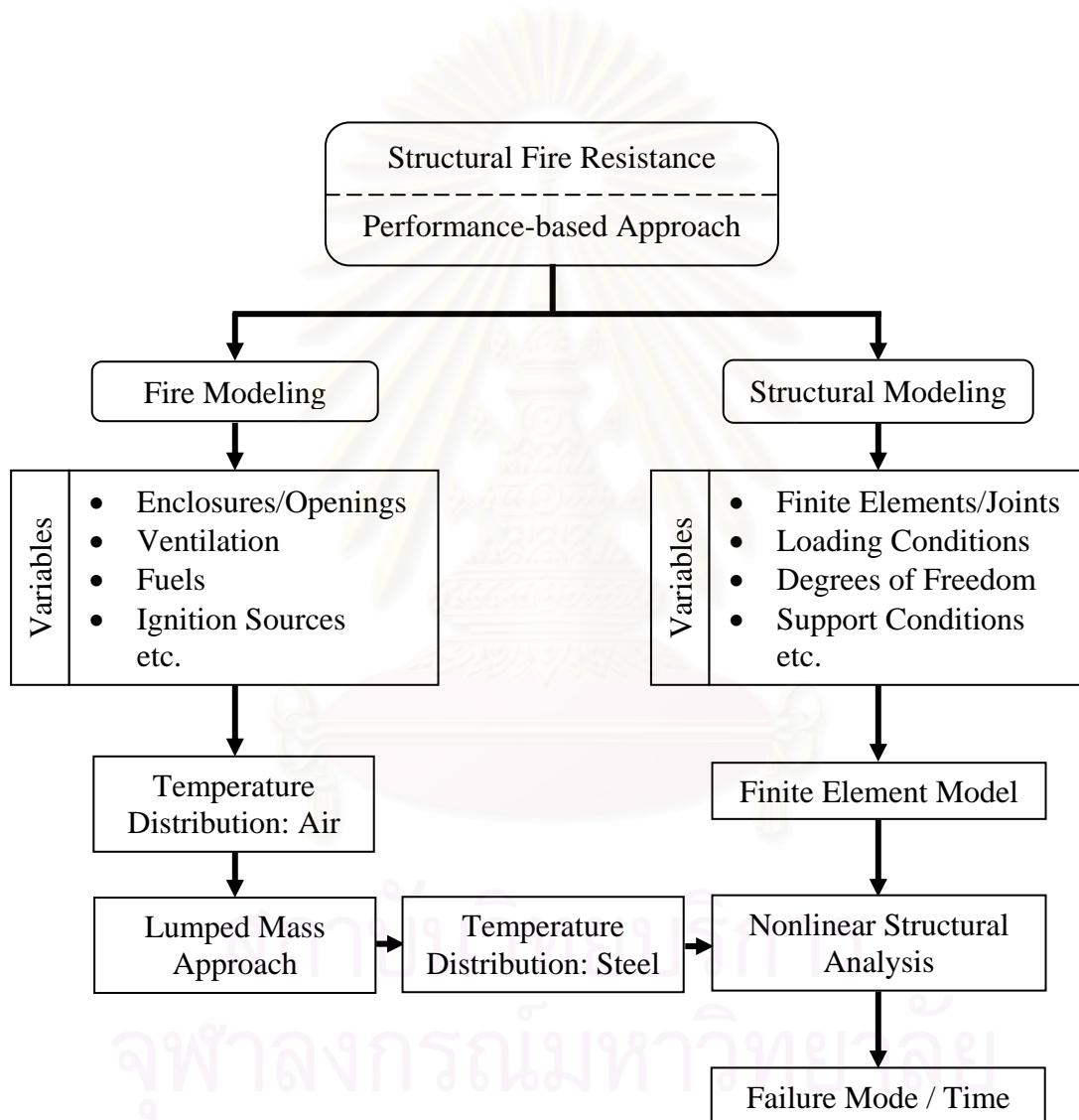


Figure 1.1 Research Framework

## CHAPTER II

### THEORETICAL BACKGROUND

#### 2.1 Introduction

The performance-based approach can be used to achieve a more economical design of steel structures for fire resistance. However, this approach requires a thorough understanding of the behavior of the fire as well as the exposed structures. The related subjects include fire modeling, air-steel heat transfer, variation of mechanical properties of steel with respect to temperature, and nonlinear finite element analysis of steel structures.

Fire modeling is the key to investigating the fire behavior. In general, the output of a fire model is the temperature distribution of air within a specified enclosure due to the simulated fire scenario which depends upon the various parameters of fire initiation (e.g. ignition source, fuel, etc.) and fire growth (e.g. ventilation, compartment openings, heat release rate of the fuel, etc.). In order to assess the effect of the varying air temperature, which is obtained from fire modeling, upon the structural performance, an analytical model of heat transfer between the surrounding air and the structural steel members is required. Once the temperature distribution of each steel member is obtained, the nonlinear finite element analysis can be employed to evaluate the structural behavior taking into account the varying mechanical properties of steel due to the enclosing fire.

#### 2.2 Fire Modeling

The rate of heat release from a pool of liquid or a solid item (e.g. furniture, etc.) burning in the open depends upon the rate at which heat from the flames can evaporate or pyrolyse the remaining fuel, and the rate at which oxygen can mix with the unburned fuel vapor to form diffusion flames. Normally, a plume of smoke and hot gases rises directly above the fire, cooling as it rises because of the large amount of surrounding air entrained into the plume. When an object is ignited and allowed to burn, the heat release rate tends to increase exponentially as the flames get larger and thus radiate more heat back to the fuel. Fire then spreads to other objects by radiation from the flames attached to the original burning item.

In small compartments, the unburned objects may ignite nearly simultaneously. This situation is referred to as “flashover.” In large compartments, it is more likely that the objects will ignite sequentially. The sequence of ignition depends on the fuel arrangement and composition, as well as the ventilation available for the combustion of the fuels. In the burning process, the peak heat release rate is first reached, followed by a steady-state burning and eventually a decay due to insufficient ventilation. The effective parameters that characterize the flames in an enclosure are as follows:



**Source of Ignition:** A different size of ignition source can produce different flames. Typically, the source with higher energy tends to induce a quicker fire growth. The low-energy source may initiate smoldering combustion, which may continue for a long time before flaming occurs. The location of the ignition source may also cause a rapid upward flame spread when it is positioned at the lower end of an opening.

**Fuel:** The thermal property of fuels is the key factor in determining the fire development in an enclosure. When the materials with low thermal inertia are exposed to heating, the surface temperature would increase rapidly so that these materials ignite instantaneously. For a given fire load, the rooms lined with low thermal-inertia materials will experience higher temperatures compared with the rooms lined with higher thermal-inertia materials. In addition, the materials with low thermal diffusivity will conduct more heat than the materials with high thermal diffusivity, when subjected to increasing surface temperatures in unsteady-state conductive heat transfer. The geometry of the fuel is another factor affecting the fire development. For example, a heavy wood fuel can cause a slow fire growth but can also keep burning for a long time.

**Enclosure Geometry:** The hot air layer within the enclosure generally radiates toward the burning fuel. The heat transfer to the fuel for a room with low ceiling will be greater than the room with high ceiling. The flame may reach the ceiling and spread horizontally underneath. This results in a considerable increase in the feedback of heat to the fuel and a very rapid fire growth. For enclosures with high ceiling and large floor area, the flames may not reach the ceiling and the feedback to the fuel may be negligible. The fire growth in this case rather occurs through direct radiation from the flame to nearby objects, where the spacing of the combustibles becomes important.

**Compartment Openings:** The fire requires access to oxygen for continuing development. In compartments of moderate volume that are closed, the fire may rapidly become oxygen-starved and may self-extinguish or continue to burn at a slow rate, depending upon the availability of oxygen. During the growth phase of the fire, before it becomes ventilation-controlled, the opening may act as an exhaust for the hot gases, if its height or position is such that the hot gases can be effectively removed from the enclosure. This will decrease the thermal feedback to the fuel and cause a slower fire growth.

When the fire becomes controlled by the availability of oxygen, the rate of burning depends on the ventilation factor,  $A_0\sqrt{H_0}$  (Huggett 1980), in which  $A_0$  is the area of the opening and  $H_0$  is the height. The rate of burning is controlled by the rate at which air can flow into the compartment. An increase in the factor  $A_0\sqrt{H_0}$  will lead to an equal increase in the burning rate.

**Properties of Bounding Surfaces:** The materials constituting the bounding surfaces of an enclosure can affect the hot gas temperature and the heat flux to the burning fuel. Certain bounding materials that are designed to conserve energy will limit the amount of heat flow to the surfaces so that the hot gases will retain most of their energy.

## 2.3 Fire Modeling Using FDS Program

As previously mentioned in Chapter 1, the current study uses the FDS program to simulate different fire scenarios. Fire modeling in FDS employs the computational fluid dynamics (CFD) model of fire-driven fluid flow. The analysis is performed numerically in the form of Navier-Stokes equations appropriate for low-speed, thermally-driven flow with an emphasis on smoke and heat transport from fires. The equations describing the transport of mass, momentum, and energy by the fire induced flows must be simplified so that they can be efficiently solved for the fire scenarios of interest. The general equations of fluid dynamics describe a rich variety of physical processes, many of which have nothing to do with fires. Retaining this generality would lead to an enormously complex computational task that would shed very little additional insight on fire dynamics. The simplified equations, developed by Rehm and Baum (1978) are solved numerically by dividing the physical space where the fire is to be simulated into a large number of rectangular cells as illustrated in Figure 2.1. Within each cell the gas velocity, temperature, etc., are assumed to be uniform; changing only with time. The accuracy with which the fire dynamics can be simulated depends upon the number of cells that can be incorporated into the simulation.

The FDS fire model consists of geometry, hydrodynamic, combustion, radiation transport, and boundary condition analyses. The current study focuses only upon the combustion, the boundary condition, and the radiation transport analyses. The geometry and hydrodynamic analyses emphasize upon the building geometry and smoke behavior.

### 2.3.1 Combustion Analysis

When the fuels reach the ignition temperature, combustion is initiated. For the FDS program, several combustion models are used to characterize the fuel combustion.

The mixture fraction combustion model is based on the assumption that the large-scale convection and radiation transport phenomena can be simulated directly, but the physical processes occurring at small length and time scales must be represented in an approximate manner (FDS 2002). The nature of the approximations employed are essentially a function of the spatial and temporal resolution limits of the computation, as well as the current understanding of the phenomena involved.

The actual chemical rate processes that control the combustion energy release are often unknown in fire scenarios. Even if they were known, the spatial and temporal resolution limits imposed by both present and foreseeable computer resources place a detailed description of combustion processes beyond reach. Thus, the model adopted in FDS is based on the assumption that the combustion is mixing-controlled. This implies that all species of interest can be described in terms of a mixture fraction,  $Z(\mathbf{x}, t)$ , where  $\mathbf{x} = (x, y, z)$  is the position vector in the Cartesian coordinates and  $t$  is the time.



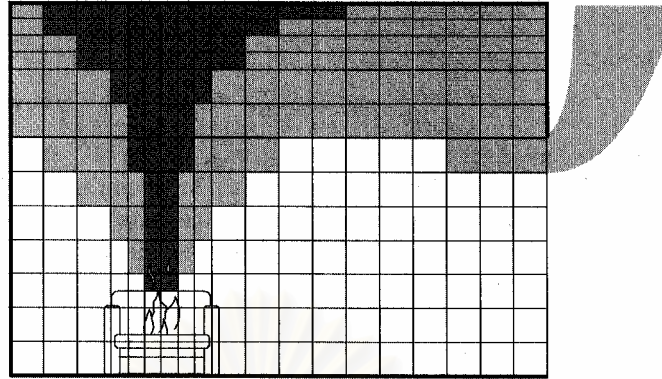


Figure 2.1 Subdivision of physical space in CFD model

The mixture fraction is a conserved quantity representing the fraction of material at a given point that originates as fuel. The relations between the mass fraction of each species and the mixture fraction are known as “state relations.” The state relation for the oxygen mass fraction provides the information needed to calculate the local oxygen mass consumption rate. The form of the state relation that emerges from classical laminar diffusion flame theory is a piecewise linear function. This leads to a “flame sheet” model, where the flame is a two-dimensional surface embedded in a three-dimensional space. The local heat release rate is computed from the local oxygen consumption rate at the flame surface, assuming that the heat release rate is directly proportional to the oxygen consumption rate, independent of the fuel involved. This relation, originally proposed by Huggett (1980), is the basis of oxygen calorimetry.

Let us consider the most general form of the combustion reaction process:



in which the numbers  $v_F$ ,  $v_O$ ,  $v_P$  are the stoichiometric coefficients of fuel, oxygen, and product, respectively, for the overall combustion process that react fuel with oxygen to produce a number of products “P”.

An expression for the local heat release rate can be derived from the conservation equations and the state relation for oxygen. The heat release rate is computed as a function of the oxygen consumption:

$$\dot{q}''' = \Delta H_o \dot{m}_o''' \quad (2.2)$$

in which

- $\dot{q}'''$  is the heat release rate per unit volume;
- $\Delta H_o$  is the heat release rate per unit mass of the oxygen consumed; and
- $\dot{m}_o'''$  is the mass consumption rate for oxidizer per unit volume.

### 2.3.2 Boundary Condition Analysis

The type of thermal boundary condition applied at any given surface depends on whether the surface is to heat up and burn, whether the burning rate will simply be prescribed, or whether there is to be any burning at all.

#### 2.3.2.1 Pyrolysis and Conduction Heat Transfer

Heat conduction is an important factor in the ignition of solid surfaces, and in the fire resistance of barriers and structural members. A solid surface that heats up due to radiative and convective heat transfer from the surrounding gas can be either thermally-thick or thermally-thin. Several material properties are needed for heat transfer and ignition calculations in solid materials. A fire can be basically modeled as the ejection of pyrolysed fuel from a solid surface or vent that burns when mixed with oxygen. This is the default mixture fraction analysis of combustion in the FDS program.

If the surface material is assumed to be thermally-thick, a one-dimensional heat conduction equation for the material temperature,  $T_s(\mathbf{n}, t)$ , is applied in the direction pointing into the air/solid interface,  $\mathbf{n} = \mathbf{0}$ , where  $\mathbf{n}$  is the spatial coordinate pointing into the solid (FDS 2002).

$$\rho_s c_s \frac{\partial T_s}{\partial t} = k_s \frac{\partial^2 T_s}{\partial n^2}; \quad -k_s \frac{\partial T_s}{\partial n}(0, t) = \dot{q}_c'' + \dot{q}_r'' - \dot{m}'' \Delta H_v \quad (2.3)$$

in which

- $\rho_s$  is the density of the material;
- $c_s$  is the specific heat of the material;
- $k_s$  is the conductivity of the material;
- $\dot{q}_c''$  is the convection heat flux at the surface;
- $\dot{q}_r''$  is the (net) radiation heat flux at the surface;
- $\dot{m}''$  is the mass loss rate of the fuel; and
- $\Delta H_v$  is the heat of vaporization.

For the FDS program it is assumed that the fuel pyrolysis takes place at the surface, thus the heat required to vaporize the fuel is extracted from the incoming energy flux. The pyrolysis rate is expressed as

$$\dot{m}'' = A e^{-E/RT} \quad (2.4)$$

in which  $A$  is the fixed value of the pre-exponential factor;  $R$  is the universal gas constant; and  $E$  is an adjustable variable such that the material burns in the neighborhood of a prescribed temperature.

The actual burning rate is governed by the overall energy balance in the solid. These parameters are often difficult to obtain for real fuels; the intent of using the given expression for the mass loss rate is to simulate the behavior of burning objects when details of their pyrolysis mechanisms are unknown.

If the surface material is assumed to be thermally-thin, that is, its temperature,  $T_s(t)$ , is assumed to be uniform across its width, and is affected by gains and losses due to convection, radiation, and pyrolysis. The thermal lag of the material is a function of the product of its density ( $\rho_s$ ), specific heat ( $c_s$ ), and thickness ( $\delta$ ), and is computed as

$$\frac{dT_s}{dt} = \frac{\dot{q}_c'' + \dot{q}_r'' - \dot{m}''\Delta H_v}{\rho_s c_s \delta} \quad (2.5)$$

The convection and radiation heat fluxes are summed over the front and back surfaces of the thin fuel. Unless otherwise specified, the back surface is assumed to face an ambient temperature void. Note that the individual values of the parameters  $\rho_s$ ,  $c_s$ , and  $\delta$  are not as important as their product,  $\rho_s c_s \delta$ , thus often in the literature and in the FDS program, the three values are lumped together as a product. The pyrolysis rate for a thermally-thin fuel is the same as for a thermally-thick one (Equation 2.4).

### 2.3.2.2 Convection Heat Transfer

The heat fluxes to a solid surface consist of gains and losses from convection and radiation. In a large eddy simulation (LES) calculation, the convection heat flux to the surface is obtained from a combination of natural and forced convection correlations

$$\dot{q}_c'' = h\Delta T; \quad h = \max \left[ C|\Delta T|^{\frac{1}{3}}, \frac{k}{L} 0.37 \text{Re}^{\frac{4}{5}} \text{Pr}^{\frac{1}{3}} \right] \quad (2.6)$$

in which

- $h$  is the heat transfer coefficient;
- $\Delta T$  is the difference between the surface and the gas temperature (taken at the center of the grid cell of the surface);
- $C$  is the coefficient for natural convection (1.43 for a horizontal surface and 0.95 for a vertical surface);
- $L$  is a characteristic length related to the size of the physical obstruction;
- $k$  is the thermal conductivity of the gas;
- $\text{Re}$  is the Reynolds number based on the gas flowing past the obstruction; and
- $\text{Pr}$  is the Prandtl number based on the gas flowing past the obstruction.

Since the Reynolds number is proportional to the characteristic length,  $L$ , the heat transfer coefficient is weakly related to  $L$ . For this reason,  $L$  is taken to be 1m for most calculations.

### 2.3.3 Radiation Transport Analysis

Radiation heat transfer is included in the FDS model via the solution of the radiation transport equation (RTE) for a non-scattering gray gas, and in some limited cases using a wide band model (RadCal 1993). The equation is solved using a technique similar to the finite volume methods for convection transport. To obtain the discretized form of the

RTE, the unit sphere is divided into a finite number of solid angles. In each grid cell a discretized equation is derived by integrating the RTE in case of a non-scattering gas over the cell and the control angle,  $d\Omega$ . The radiant heat flux vector,  $\mathbf{q}_r$ , is defined as

$$\mathbf{q}_r(\mathbf{x}) = \int_{\Omega} \mathbf{s}I(\mathbf{x},\mathbf{s})d\Omega \quad (2.7)$$

The radiation loss term in the energy equation is computed as

$$-\nabla \mathbf{q}_r(\mathbf{x}) = \kappa(\mathbf{x})[U(\mathbf{x}) - 4\pi I_b(\mathbf{x})]; \quad U(\mathbf{x}) = \int_{4\pi} I(\mathbf{x},\mathbf{s})d\Omega \quad (2.8)$$

in which

- $I$  is the radiation intensity;
- $I_b$  is the radiation blackbody intensity;
- $\mathbf{s}$  is the unit vector in the direction of the radiation intensity; and
- $\kappa$  is the absorption coefficient.

Assuming that the radiation intensity  $I(\mathbf{x},\mathbf{s})$  is constant on each of the cell faces, the surface integral can be approximated by a sum over the cell faces. In other words, the net radiant energy gained by a grid cell is the difference between that which is absorbed and that which is emitted.

### 2.3.4 Fire Modeling Parameters

As previously mentioned, the current study adopts the FDS program to model various fire scenarios. All of the parameters that describe a given fire scenario are typed into a text file that will be referred to as the “data” or “input” file. The input file provides the program with the parameters to describe the scenario under consideration. The parameters are organized into groups of related variables. Details of the input parameters and the modeling outcome are shown in Figure 2.2.

สถาบันวิทยบริการ  
จุฬาลงกรณ์มหาวิทยาลัย

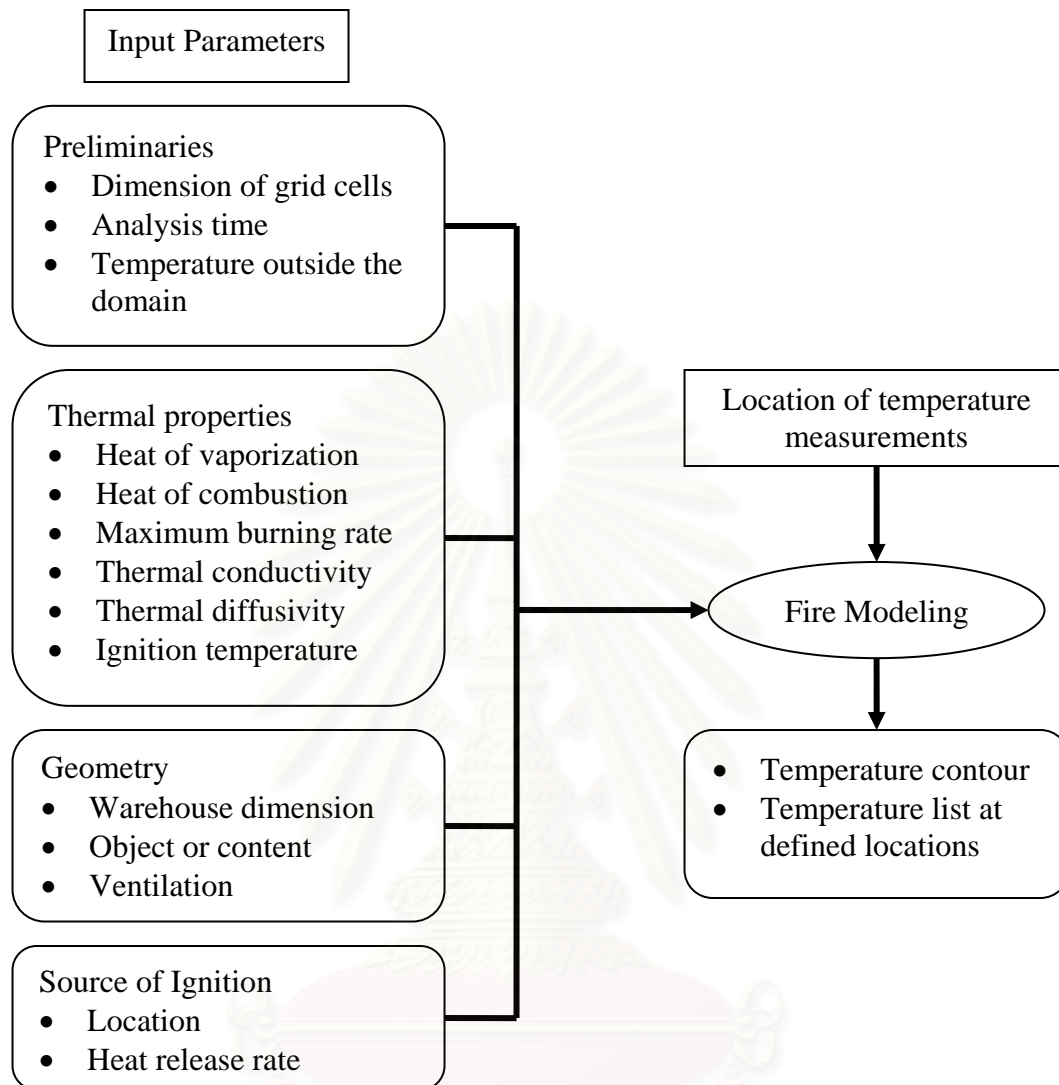


Figure 2.2 Input parameters in fire modeling

#### 2.4 Calculation of Steel Temperature

For the current study we employ the spreadsheet method of predicting the temperature of a steel member using the principles of heat transfer to estimate the energy being transferred to the steel member, and thus the rate of temperature rise. The methods for protected and unprotected steel members are basically the same, with different formulas to allow the effect of the protection on the rate of heating of the steel. The method has been recommended by the European Convention for Constructional Steelwork (ECCS 1993) as a procedure for calculating the fire resistance of elements of construction exposed to the standard fire.



The method is a one-dimensional heat flow analysis that accounts for the properties of the insulation as well as the perimeter/area ratio,  $H_p/A$ , of the steel section (Gamble 1989). The temperature of the section can be calculated at each time step, by considering the energy that the section is subjected to during the previous time interval. The duration of the time step does not significantly affect the calculated temperatures. Petterson *et al.* (1976) have suggested a time step so that there are 10 to 20 time steps until the limiting temperature of the steel is reached whereas Gamble (1989) has recommended using a time step of 10 minutes. For the analyses in the current study, a time step of 1 minute is used for the majority of the calculations as the speed and capabilities of modern computers requires very little more effort to decrease the time step period to this value.

The spreadsheet method assumes that the steel member is of constant thickness governed by the  $H_p/A$  value. This is called a lumped mass approach as no regard is given for the actual geometry of the cross section. Constant values for the thermal properties of the steel, such as the specific heat and density, are generally used to simplify the method and to reduce the number of variables in the spreadsheet. The values for the thermal properties of the steel and geometry of the shape are average values and not necessarily exactly what the member will be when constructed in place. This means that high accuracy is unnecessary and often inappropriate when many other factors, such as the temperature of the fire are also estimated (Lewis 2000).

The advantages of the spreadsheet program are that the required computer software is basically a spreadsheet program, such as Microsoft Excel, which is installed in most office computers. For other computer programs, such as SAFIR, additional files such as the section sizes are required as well as the units of the program. With the estimations and assumptions made in fire design and analysis, the 5 % difference found between the two methods was insufficient to show that one is more accurate than the other (Lewis 2000). Since the spreadsheet method usually gives higher temperatures than SAFIR and other computer programs, the results are acceptable for use in design with four-sided exposure and are considered conservative.

#### 2.4.1 Steel without Fire Protection

The temperature of the unprotected steel can be obtained based upon the difference in the temperature of steel over a time step  $\Delta t$  (Buchanan 1999):

$$\Delta T_s = \left( \frac{H_p}{A} \right) \left( \frac{h_t}{\rho_s c_s} \right) (T_f - T_s) \quad (2.9)$$

in which

$H_p/A$  is the section factor of the steel section ( $\text{m}^{-1}$ );

$\rho_s$  is the density of steel ( $\text{kg}/\text{m}^3$ );

$c_s$  is the specific heat of steel ( $\text{J}/\text{kg}\cdot\text{K}$ );

$h_t$  is the sum of the radiation and convection heat transfer coefficients;

- $T_f$  is the temperature of the surrounding fire within the specified time step  $\Delta t$ ; and  
 $T_s$  is the temperature of steel at the beginning of the time step  $\Delta t$ .

The value of the convection heat transfer coefficient used in the current study is 25 W/m<sup>2</sup>-K as recommended by the Eurocode for standard fires (Buchanan 1999). Since the radiation heat transfer depends on the temperatures of the steel member and its surroundings, this component of the total heat transfer coefficient must be calculated at each time step, using the following formula:

$$h_t = 25 + \sigma \varepsilon \left( \frac{T_f^4 - T_s^4}{T_f - T_s} \right) \quad (2.10)$$

in which

- $\sigma$  is the Stefan-Boltzman constant ( $5.67 \times 10^{-8}$  kW/m<sup>2</sup>-K<sup>4</sup>); and  
 $\varepsilon$  is the emissivity of the fire.

The Eurocode recommends using a value of 0.56 for the emissivity,  $\varepsilon$ , but for the current study  $\varepsilon = 0.5$  is used as recommended by Martin and Purkiss (1992).

#### 2.4.2 Steel with Fire Protection

The method for determining the temperature of steel sections with fire protection is similar to the unprotected sections, but with a different formula to account for the effect of the insulation on the rise of the steel temperature. By assuming that the exterior surface of the insulation has the same temperature as the surroundings, i.e. the fire, the heat transfer coefficient is not required. It is also assumed that the steel is at the same temperature as the internal surface of the insulation. As such, the change in the temperature of the protected steel over a time period can be computed as:

$$\Delta T_s = \left( \frac{H_p}{A} \right) \left( \frac{k_i}{d_i \rho_s c_s} \right) \left\{ \frac{\rho_s c_s}{\rho_s c_s + \frac{H_p}{2A} d_i \rho_i c_i} \right\} (T_f - T_s) \Delta t \quad (2.11)$$

in which

- $d_i$  is the thickness of the insulation (m);  
 $\rho_i$  is the density of the insulation (kg/m<sup>3</sup>);  
 $c_i$  is the specific heat of the insulation (J/kg-K); and  
 $k_i$  is the thermal conductivity of the insulation (W/m-K).

EC3 (1995) has recommended a slightly different formula from Equation (2.11), where a 3 is used instead of the 2 in the brackets {}, and also an extra term is included to account for the increase in fire temperature over the time step  $\Delta t$  (Buchanan 1999). To determine whether the protection will absorb much heat as to significantly affect the temperature of the steel, ECCS (1985) has suggested calculating whether the heat



capacity of the insulation is more than half the heat capacity of the steel, using the following formula:

$$\rho_s c_s A_s > 2\rho_i c_i A_i \quad (2.12)$$

in which  $A_i$  and  $A_s$  are the cross sectional area of the insulation and steel, respectively.

If the above equation is true then the insulation can be considered 'light' and the heavy insulation term in the brackets { } can be omitted to simplify the equation. Another method, as recommended by ECCS, for heavy insulation uses the following expression:

$$\Delta T_s = \left( \frac{H_p}{A} \right) \left( \frac{k_i}{d_i \rho_s c_s} \right) \frac{(T_f - T_s) \Delta t}{(1 + \phi/2)} - \frac{\Delta T_f}{(1 + \phi/2)} \quad (2.13)$$

where

$$\phi = \left( \frac{H_p}{A} \right) d_i \left( \frac{\rho_i c_i}{\rho_s c_s} \right) \quad (2.14)$$

and the time step  $\Delta t$  is limited by the following inequation:

$$\Delta t \leq \frac{25000}{\left( \frac{H_p}{A} \right)} \quad (2.15)$$

EC3 (ENV 1993-1-2) has proposed another formula which has been derived by Wickstrom:

$$\Delta T_s = \left( \frac{H_p}{A} \right) \left( \frac{k_i}{d_i \rho_s c_s} \right) \frac{(T_f - T_s) \Delta t}{(1 + \phi/3)} - \left( e^{\left( \frac{\phi}{10} \right)} - 1 \right) \Delta T_f \quad (2.16)$$

where  $\phi$  is defined in Equation (2.14), and  $\Delta T_f$  is the change in fire temperature over the time step. The time step (in seconds) for this case is defined as:

$$\Delta t = \left( \frac{H_p}{A} \right) \left( \frac{\rho_s c_s}{k_i} \right) \left( 1 + \left( \frac{\phi}{3} \right) \right) < 60 \quad (2.17)$$

The current study adopts the Eurocode 3 (ENV 1993-1-2) method for calculating the temperature of steel with fire protection.

## 2.5 Variation of Steel Properties with Temperature

Various literature searches show that all agree that the thermal and mechanical properties of steel change with varying temperatures. Under high-temperature conditions (i.e., fire), certain properties of the structural steel, e.g. the yield and the ultimate strength, the modulus of elasticity, etc., would drop significantly while the coefficient of expansion would increase. The thermal properties of the steel are generally assumed to stay constant for simplicity in calculations. The specific heat, density and thermal conductivity do

however vary with temperature, and although the difference does not usually effect the temperature of the steel found from the analyses significantly, the differences should still be noted.

### 2.5.1 Variation of Mechanical Properties of Steel with Temperature

The variation of the mechanical properties of steel poses a direct threat to the load-carrying capacity of the steel structures that are designed to be used in normal temperature conditions. The drop of the mechanical properties and the increase of the coefficient of expansion are the keys to the failure of steel structures at high temperatures. The expansion from the increasing temperature leads to excessive displacements of the structures, magnifying the eccentricity of loads, particularly the axial compression forces, upon the structural members.

The current study adopts the properties of A36 steel. The mechanical properties of A36 steel with respect to the varying temperatures in the range of 20 – 600°C are listed in Table 2.1 (ANSI/AISC 360-05).

Table 2.1 Mechanical properties of A36 steel with respect to varying temperatures

Temperature (°C)	Modulus of elasticity, $E$ (kg/m <sup>2</sup> )	Yield strength, $F_y$ (kg/m <sup>2</sup> )	Coefficient of thermal expansion (1/°C)
20	2.10E+10	2.40E+07	1.40E-05
93	2.10E+10	2.40E+07	1.40E-05
204	1.89E+10	2.40E+07	1.40E-05
316	1.64E+10	2.40E+07	1.40E-05
399	1.47E+10	2.40E+07	1.40E-05
427	1.41E+10	2.26E+07	1.40E-05
538	1.03E+10	1.58E+07	1.40E-05
649	4.62E+09	8.40E+06	1.40E-05
760	2.31E+09	3.84E+06	1.40E-05
871	1.47E+09	1.68E+06	1.40E-05

## 2.5.2 Variation of Thermal Properties of Steel with Temperature

For the thermal properties of steel, the specific heat has the largest deviation from a constant value. For the analyses performed in the current study, and in most fire situations (Lewis 2000), the equations used are taken from ENV 1993-1-2, as follows:

$$\begin{aligned}
 c_s &= 425 + 0.773T_s + 1.69 \times 10^{-3}T_s^2 + 2.22 \times 10^{-6}T_s^3 & 20 \leq T_s < 600^\circ\text{C} \\
 c_s &= 666 - \frac{13002}{T_s - 739} & 600 \leq T_s < 735^\circ\text{C} \\
 c_s &= 545 + \frac{17820}{T_s - 731} & 735 \leq T_s < 900^\circ\text{C} \\
 c_s &= 650 & 900 \leq T_s < 1200^\circ\text{C}
 \end{aligned} \tag{2.18}$$

The thermal conductivity of steel varies slightly for different grades of steel, and with changes in the steel temperature. The difference between the grades of steel is not significant. ENV 1993-1-2 has suggested the following equation for the thermal conductivity of steel

$$\begin{aligned}
 k_s &= 54 - 0.0333T_s & T_s \leq 800^\circ\text{C} \\
 k_s &= 27.3 & 800^\circ\text{C} < T_s
 \end{aligned} \tag{2.19}$$

Nevertheless, the thermal conductivity of steel is not used in the current study because the steel temperature is computed using the lump mass approach.

## 2.6 Nonlinear Finite Element Analysis of Steel Frames Subjected to Varying Temperatures

As previously mentioned, the nonlinear finite element analysis is employed in the current study to investigate the behavior of the steel roof structure subjected to varying temperatures. Figure 2.3 summarizes the process and the parameters involved in the analysis. In modeling the steel structures, the properties of A36 steel with respect to temperature in Table 2.1 are adopted. In the process of structural analysis, the Newton-Raphson iterative method is used to solve the system of nonlinear equations for each temperature increment. The displacement, strain, and stress components resulting from the imposed temperature variation are computed continuously until the structural failure, at which the failure mode and time can be identified.

At each temperature increment in the nonlinear finite element analysis process, the structure is checked for buckling of compressive elements and yielding of tensile elements. This is referred to as the element failure check in Figure 2.3. If the stress level within an element exceeds its specified limit, that element will be eliminated from the structural system before the next analysis step. For the current study the failure of the structure is deemed to occur when the top or bottom chords of the main roof frames fail.

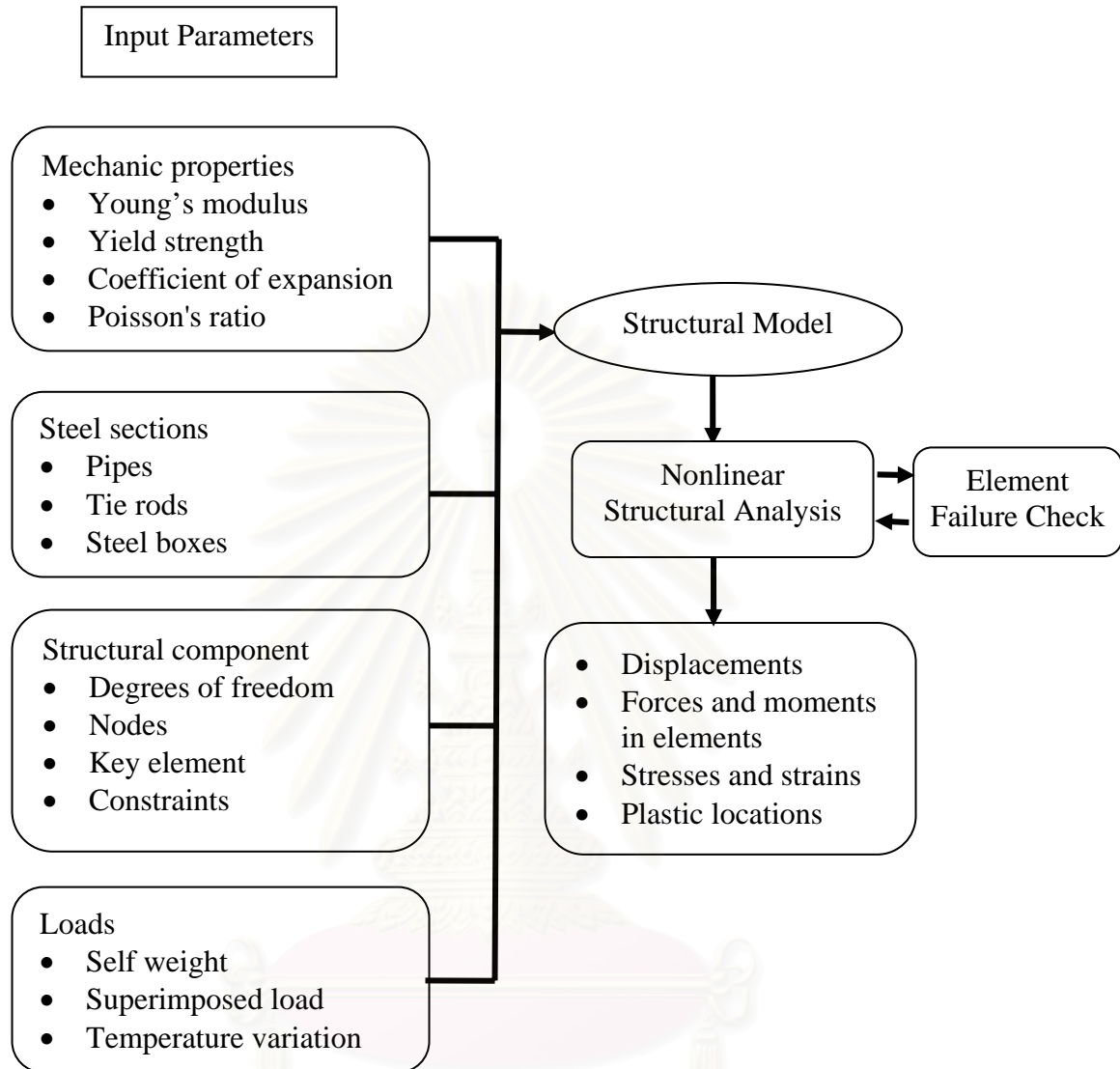


Figure 2.3 Nonlinear structural analysis process

The structural element examined in the current study is a circular pipe consisting of six degrees of freedom (DOF) at each node: nodal translations in the local  $x$ ,  $y$ , and  $z$  directions, and rotations about the  $x$ ,  $y$ , and  $z$  axes. The local  $x$ -axis is oriented from node I towards node J as shown in Figure 2.4. The local  $y$ -axis is parallel to the global  $X$ - $Y$  plane.

In a finite-element model, a structure is discretized into an assemblage of finite elements interconnected at nodal points on the element boundaries. The displacement field within each element is assumed to be a function of the displacements at the element nodal points. The displacement functions for the circular pipe elements are shown in Equation (2.12) and the corresponding displacement components are illustrated in Figure 2.5.

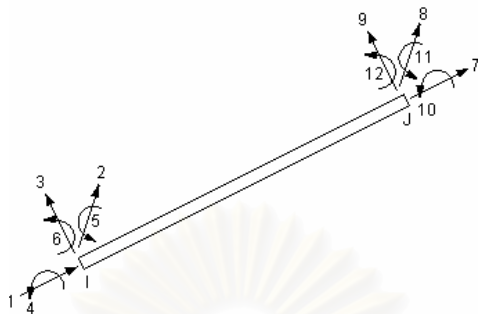


Figure 2.4 Degrees of freedom of the circular pipe element

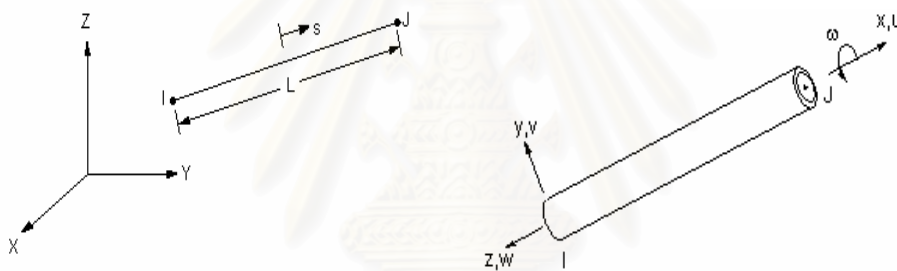


Figure 2.5 Displacements of the circular pipe element

$$\mathbf{u}_m(s) = \mathbf{N}_m(s) \mathbf{u}_\ell$$

$$\begin{bmatrix} u \\ v \\ w \\ \theta_x \end{bmatrix} = \begin{bmatrix} a & b & 0 & 0 & 0 & 0 & 0 & 0 & 0 & 0 & 0 & 0 \\ 0 & 0 & c & d & 0 & 0 & 0 & 0 & 0 & e & -f & 0 \\ 0 & 0 & 0 & 0 & c & d & 0 & 0 & -e & f & 0 & 0 \\ 0 & 0 & 0 & 0 & 0 & 0 & a & b & 0 & 0 & 0 & 0 \end{bmatrix} \begin{bmatrix} u_i \\ u_j \\ v_i \\ v_j \\ w_i \\ w_j \\ \theta_{xi} \\ \theta_{xj} \\ \theta_{yi} \\ \theta_{yj} \\ \theta_{zi} \\ \theta_{zj} \end{bmatrix} \tag{2.12}$$

in which

$$\begin{aligned} a &= \frac{(1-s)}{2} & b &= \frac{(1+s)}{2} \\ c &= \frac{1}{2} - \frac{s}{4}(3-s^2) & d &= \frac{1}{2} + \frac{s}{4}(3-s^2) \\ e &= \frac{L}{8}(1-s^2)(1-s) & f &= \frac{L}{8}(1-s^2)(1+s) \end{aligned}$$

where

- $\mathbf{u}_m(s)$  is the vector of displacement functions for the pipe element  $m$  expressed in terms of the local coordinate  $s$  ;
- $\mathbf{u}_\ell$  is the vector of local displacements at nodes I and J;
- $\mathbf{N}_m(s)$  is the matrix of displacement interpolation or shape functions

Note that the formulation of the circular pipe element neglects the lateral torsional buckling effect, and thus  $\theta_y$  and  $\theta_z$  are not considered.

The varying temperature from the simulated fire scenarios causes the structural elements to elongate. Because the thermal elongation is restrained by the interconnected elements within the structure, the thermal force arises within the element which can be expressed as

$$F_{thermal} = E_T A \alpha_T (\Delta T) \quad (2.13)$$

in which

- $F_{thermal}$  is the thermal force;
- $E_T$  is the modulus of elasticity at temperature  $T$  ;
- $A$  is the cross-sectional area of the element;
- $\alpha_T$  is the coefficient of thermal expansion at temperature  $T$  ; and
- $\Delta T$  is the temperature increment.

The thermal force is the key to the stability of the structure. The temperature variation is input in terms of the nodal temperature and is assumed to vary linearly along the length of the element. The value of the input nodal temperature is computed using the lumped mass approach.

The thermal force in Equation (2.13) is assembled to the element load vector, which can be converted to the external force vector of the element using the following relationship

$$\mathbf{F}_\ell = \mathbf{T}_R (\mathbf{K}_e \Delta \mathbf{u}_e - \mathbf{F}_e) \quad (2.14)$$

in which

- $\mathbf{F}_\ell$  is the vector of external member forces;
- $\mathbf{T}_R$  is the local to global transformation matrix;
- $\mathbf{K}_e$  is the element stiffness matrix;
- $\Delta \mathbf{u}_e$  is the element incremental displacement vector; and
- $\mathbf{F}_e$  is the element load vector from thermal and Newton-Raphson restoring force effects.









where

$$l_x = \cos \alpha_x; m_x = \cos \beta_x; n_x = \cos \gamma_x$$

$$l_y = \cos \alpha_y; m_y = \cos \beta_y; n_y = \cos \gamma_y$$

$$l_z = \cos \alpha_z; m_z = \cos \beta_z; n_z = \cos \gamma_z$$

The stress components, as illustrated in Figure 2.6, are computed using the formulas provided in Table 2.2.

Table 2.2 Formulas of stress components for rectangular and pipe sections

	Rectangular Section	Pipe Section
The centroidal stress, $\sigma^{\text{dir}}$	$\sigma^{\text{dir}} = \frac{F_x}{A}$	$\sigma^{\text{dir}} = \frac{F_x}{A}$
The bending stresses, $\sigma^{\text{bend}}$	$\sigma_z^{\text{bend}} = \frac{M_y t_z}{2I_y}$ $\sigma_y^{\text{bend}} = \frac{M_z t_y}{2I_z}$	$\sigma^{\text{bend}} = \frac{M_b r}{I}$
The lateral-force shear stress, $\sigma^{\text{lat}}$	$\sigma_y^{\text{lat}} = \frac{2F_y}{A}$ $\sigma_z^{\text{lat}} = \frac{2F_z}{A}$	$\sigma^{\text{lat}} = \frac{2F_s}{A}$
The torsional shear stress, $\sigma^{\text{tor}}$	$\sigma_z^{\text{tor}} = \frac{M_x t_z}{J}$ $\sigma_y^{\text{tor}} = \frac{M_x t_y}{J}$	$\sigma^{\text{tor}} = \frac{M_x r}{J}$

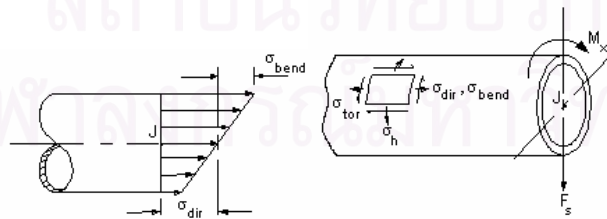


Figure 2.6 Stress components for the circular pipe element

In Table 2.2,


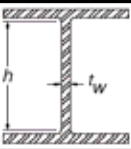

- $F_x$  is the axial force;
- $F_y$  is the shear force in the element  $x$ -axis;
- $F_z$  is the shear force in the element  $z$ -axis;
- $F_s$  is the total shear force,  $F_s = \sqrt{F_y^2 + F_z^2}$  ;
- $M_x$  is the moment about the element  $x$ -axis;
- $M_y$  is the moment about the element  $y$ -axis;
- $M_z$  is the moment about the element  $z$ -axis;
- $M_b$  is the total bending moment,  $M_b = \sqrt{M_y^2 + M_z^2}$  ;
- $r$  is the outside radius of the pipe section;
- $t_z$  is the thickness of the element in  $z$ -direction; and
- $t_y$  is the thickness of the element in  $y$ -direction.

## 2.7 ANSI/AISC 360-05 Buckling Analysis

According to ANSI/AISC 360-05, sections are classified as compact, noncompact, or slender-element sections. For a section to qualify as compact its flanges must be continuously connected to the web or webs and the width-thickness ratios of its compression elements must not exceed the limiting width-thickness ratios  $\lambda_p$  shown in Table 2.3. If the width-thickness ratio of one or more compression elements exceeds  $\lambda_p$ , but does not exceed  $\lambda_r$  in Table 2.3, the section is noncompact. If the width-thickness ratio of any element exceeds  $\lambda_r$ , the section is referred to as a slender-element section.

For the compact and noncompact sections that are used in the current study, the local buckling effect is not taken into account. The present analyses involve three types of buckling in which the compression strength of the sections can be summarized below:

Table 2.3 Limiting width-thickness ratios for compression elements  
(Sect.B4, 16-18 ANSI/AISC 360-05)

Description of Element	Width Thickness Ratio	Limiting Width-Thickness Ratios		Example
		$\lambda_p$ (compact)	$\lambda_r$ (noncompact)	
Flexure in flanges of rolled I-shaped sections and channels	$b/t$	$0.38\sqrt{E/F_y}$	$1.0\sqrt{E/F_y}$	
Flexure in webs of doubly symmetric I-shaped sections and channels	$h/t_w$	$3.76\sqrt{E/F_y}$	$5.70\sqrt{E/F_y}$	
Circular hollow sections In uniform compression	$D/t$	NA	$0.11 E/F_y$	
In flexure	$D/t$	$0.07 E/F_y$	$0.31 E/F_y$	

2.7.1 For uniformly compressed elements, the flexural buckling strength,  $F_{cr}$ , when using compression members with compact and noncompact sections, is determined as follows:

a) When  $\frac{KL}{r} \leq 4.71 \sqrt{\frac{E}{F_y}}$

$$F_{cr} = \left[ 0.658 \frac{F_y}{F_e} \right] F_y \quad (2.20)$$

b) When  $\frac{KL}{r} > 4.71 \sqrt{\frac{E}{F_y}}$

$$F_{cr} = 0.877 F_e \quad (2.21)$$

in which

$$F_e = \frac{\pi^2 E}{\left( \frac{KL}{r} \right)^2}$$

whereas

- $L$  is the laterally unbraced length of the member (cm);
- $r$  is the governing radius of gyration (cm); and
- $K$  is the effective length factor.

2.7.2 The limit state of flexural-torsional and torsional buckling for singly symmetric members where  $y$  is the axis of symmetry, can be computed as follows:

$$F_e = \left( \frac{F_{ey} + F_{ez}}{2H} \right) \left[ 1 - \sqrt{1 - \frac{4F_{ey}F_{ez}H}{(F_{ey} + F_{ez})^2}} \right] \quad (2.22)$$

in which

$$\bar{r}_o^2 = x_o^2 + y_o^2 + \frac{I_x + I_y}{A_g}$$

$$H = 1 - \frac{x_o^2 + y_o^2}{\bar{r}_o^2}$$

$$F_{ex} = \frac{\pi^2 E}{\left( \frac{K_x L}{r_x} \right)^2}$$

$$F_{ey} = \frac{\pi^2 E}{\left( \frac{K_y L}{r_y} \right)^2}$$

$$F_{ez} = \left( \frac{\pi^2 EC_w}{(K_z L)^2} + GJ \right) \frac{1}{A_g \bar{r}_o^2}$$

whereas

$A_g$  is the gross area of member (cm<sup>2</sup>);

$C_w$  is the warping constant (cm<sup>6</sup>);

$I_x, I_y$  are the moments of inertia about the principal axes (cm<sup>4</sup>);

$J$  is the torsional constant (cm<sup>4</sup>);

$K_z$  is the effective length factor for torsional buckling;

$x_0, y_0$  are the coordinates of shear center with respect to the centroid (cm);

$\bar{r}_0$  is the polar radius of gyration about the shear center (cm); and

$r_y$  is the radius of gyration about y-axis (cm).

2.7.3 The lateral-torsional buckling moment for doubly symmetric I-shaped members and channels bent about their major axis, having compact webs and compact or noncompact flanges is computed as follows:

a) When  $L_p < L_b \leq L_r$ ,

$$M_n = C_b \left[ M_p - (M_p - 0.7F_y s_x) \left( \frac{L_b - L_p}{L_r - L_p} \right) \right] \leq M_p \quad (2.23)$$

b) When  $L_b > L_r$ ,

$$M_n = F_{cr} s_x \leq M_p \quad (2.24)$$

where the limiting lengths  $L_p$  and  $L_r$  are determined as follows:

$$L_p = 1.76 r_y \sqrt{\frac{E}{F_y}} \quad (2.25)$$

$$L_r = \pi r_{ts} \sqrt{\frac{E}{0.7F_y}} \quad (2.26)$$

$$r_{ts}^2 = \frac{\sqrt{I_y C_w}}{s_x} \quad (2.27)$$

Note that Equation (2.26) is extremely conservative.

in which

$L_b$  is the length between points that are either braced against lateral displacement of compression flange or braced against twist of the cross section (cm);

$J$  is the torsional constant (cm<sup>4</sup>);

$s_x$  is the elastic section modulus taken about the x-axis (cm<sup>3</sup>); and

$C_b$  is the permitted to be conservatively taken as 1.0 for all cases.

The interaction of flexure and compression in doubly symmetric members and singly symmetric members is governed by (AISC 2005)

$$\frac{P_r}{P_c} + \frac{8}{9} \left( \frac{M_{rx}}{M_{cx}} + \frac{M_{ry}}{M_{cy}} \right) \leq 1 \quad \text{for } P_r / P_c \geq 0.2 \quad (2.26)$$

$$\frac{P_r}{2P_c} + \left( \frac{M_{rx}}{M_{cx}} + \frac{M_{ry}}{M_{cy}} \right) \leq 1 \quad \text{for } P_r / P_c < 0.2 \quad (2.27)$$

in which

- $P_r$  is the required axial compressive strength from nonlinear analysis;
- $P_c$  is the available axial compressive strength from buckling analysis;
- $M_r$  is the required flexural strength from nonlinear analysis;
- $M_c$  is the available flexural strength from buckling analysis;
- $x$  is the subscript relating symbols to strong axis bending; and
- $y$  is the subscript relating symbols to weak axis bending.



## CHAPTER III

### PRELIMINARY SIMULATION STUDIES

#### 3.1 Introduction

As previously mentioned in Chapter 2 that various parameters are involved in fire modeling, Chapter 3 is thus aimed to investigate the sensitivity of these parameters on the fire modeling results obtained from using the FDS program. For the current study we focus upon the characteristics of fuel by using the results obtained from fire tests of the roofing system for the Passenger Terminal Building of the Second Bangkok International Airport (Troitzsch 2004) as our case study. The various characteristics of fuel investigated herein are the specific heat, the ignition temperature, the density, the heat of vaporization, the heat of combustion and the ignition source. Even though certain assumptions are made in this preliminary model, the key objective is to illustrate the capability of FDS in predicting the temperature distribution within a specified enclosure and the effects of the varying fuel characteristics on the fire modeling outputs.

The second part of Chapter 3 involves a simulation study of air-to-steel heat transfer. In this section, the computer program ANSYS is used to examine the accuracy of the lumped mass approach (the spreadsheet method). It is investigated whether the spreadsheet method can be used with the same confidence as for the finite element computer program to compute the changing temperatures of steel subjected to fire.

#### 3.2 Fire Tests of the Roofing System for the Passenger Terminal Building of the Second Bangkok International Airport

To simulate usage of the roofing system for the Passenger Terminal Building under real-life conditions, a series of large-scale fire tests were conducted with a simulated membrane roofing system in a steel frame system of 2.5 m by 2.5 m using 50 kg wood cribs (Troitzsch 2004). The frame system is composed of three single frames which were screwed together as illustrated in Figure 3.1. For the current study, only the fire test in which the frame system was arranged in the horizontal position ( $0^\circ$  with horizontal plane) is examined.

Sets of thermocouples were installed on the external, medium and internal layers of the simulated roofing system and over the fire source (the 50 kg wood crib) for temperature measurement and connected to a computer for recording and registration. The expertise and material support in terms of temperature measuring equipment were provided by the Fire Safety Research Center, Chulalongkorn University.

The 50 kg wood crib consisting of wood club layers with a total height of around 40 cm was positioned in the geometrical middle under the roofing system. During the test wind velocity measurements were made with an anemometer. The wind was steady with a measured velocity of approximately 0.3 m/s. The wind direction was mainly from left to right on the test arrangement. Figure 3.2 illustrates the overall setup of the fire test.

The temperature measurements obtained from the fire test are used to compare with the results obtained from fire modeling using the FDS program. In particular, the temperature distribution within the enclosure underneath the internal (lowest) layer is examined. The locations of the thermocouples installed underneath the internal layer and over the 50 kg wood crib are shown in Figure 3.3.

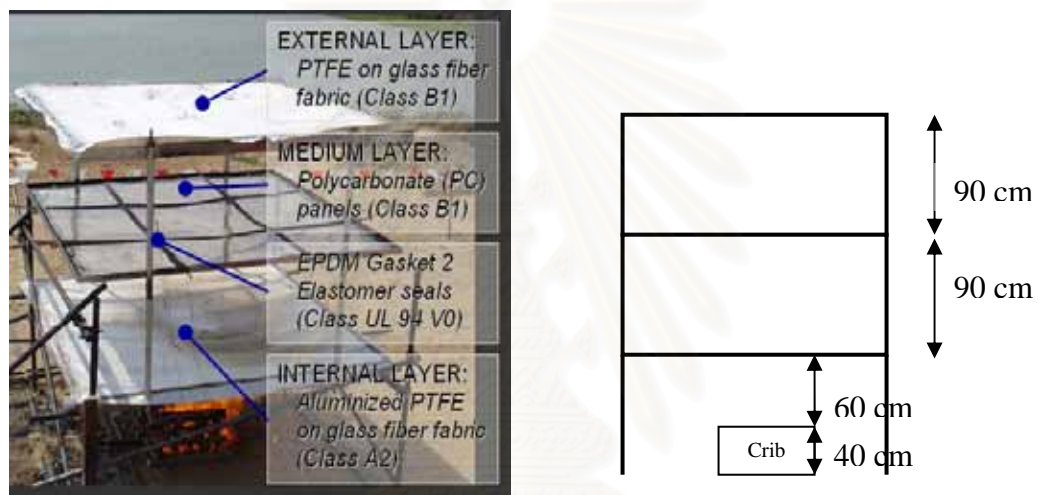


Figure 3.1 Simulated membrane roofing system



Figure 3.2 Fire test setup

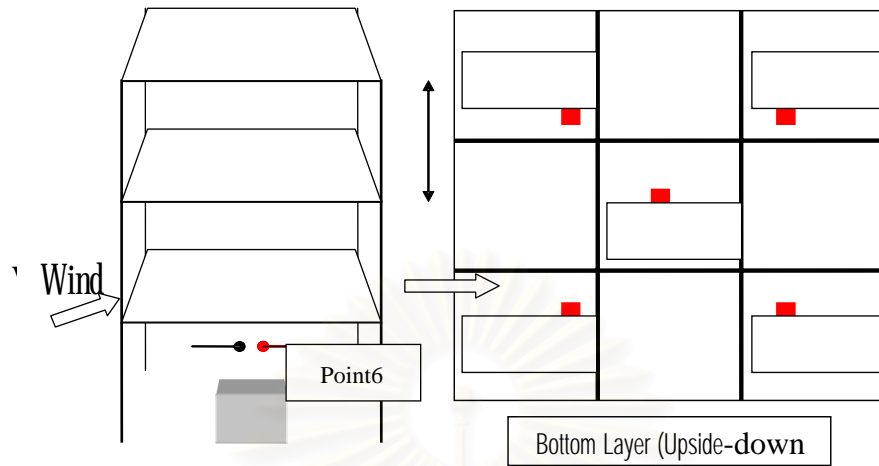


Figure 3.3 Location of thermocouples on the bottom layer of the roofing system and above the wood crib

In modeling with FDS, the key input parameters are

- Roofing system geometry: As shown in Figure 3.4
- Thermal properties of the ignition source (wood crib)
 

Specific heat:	2.57	kJ/kg-K
Ignition temperature:	300	°C
Density:	600	kg/m <sup>3</sup>
Heat of vaporization:	1800	kJ/kg
Heat of combustion:	12000	kJ/kg
- Heat release rate from the ignition source: 400 kW/m<sup>2</sup>
- Wind velocity: 0.3 m/s

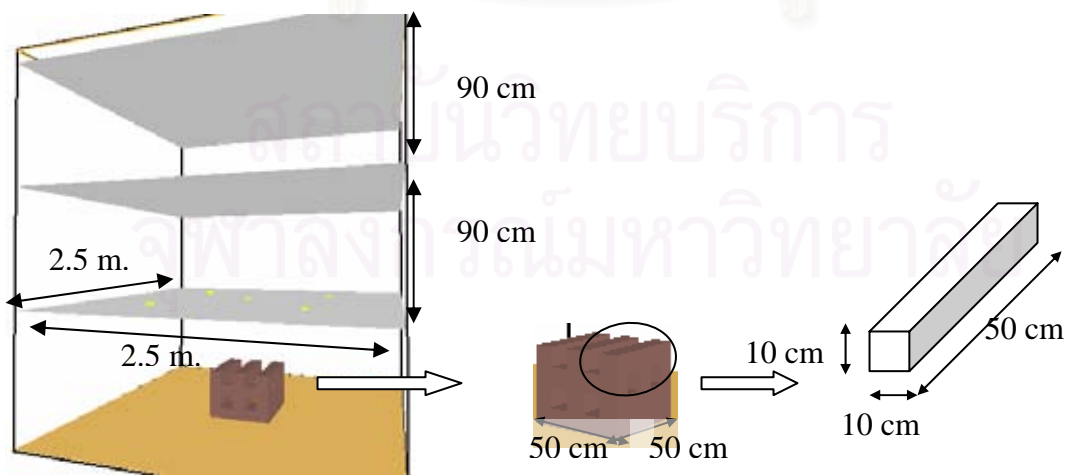


Figure 3.4 FDS model

The temperature collection points defined in the FDS model correspond with the locations of the thermocouples that properly functioned during the test (i.e., Points 2, 3, 5 and 6). Figure 3.5 shows the sequences of fire growths obtained from fire modeling with FDS. In Figure 3.6, the FDS temperature results are plotted in comparison with the measured temperatures from the fire test.

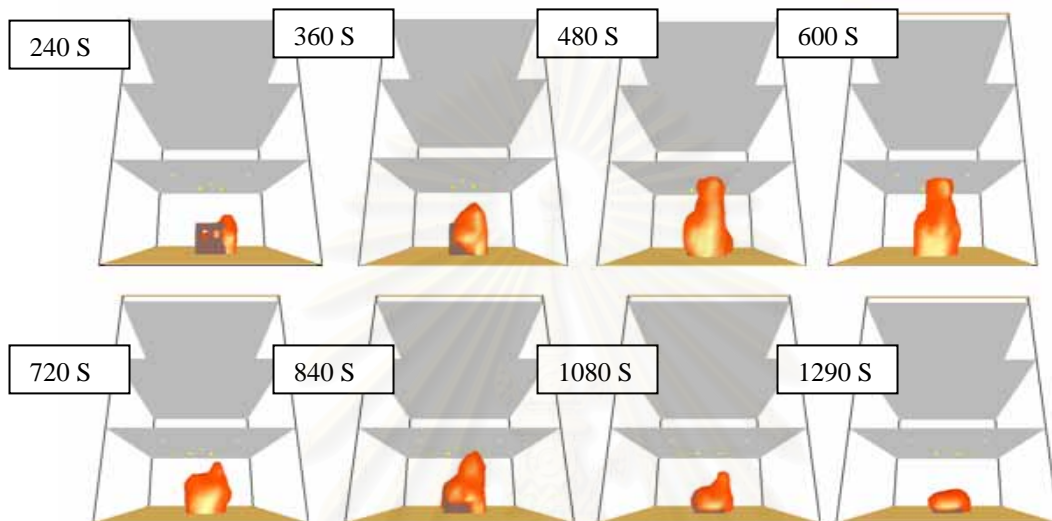


Figure 3.5 Fire growths from FDS model

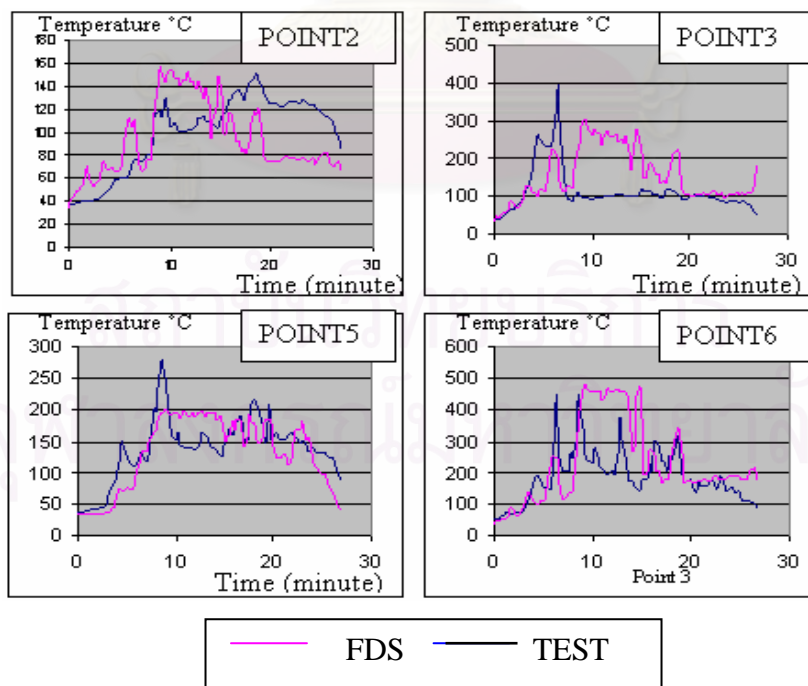


Figure 3.6 Fire test temperature measurements vs. FDS results

It is seen from Figure 3.6 that by using the above set of input parameters the FDS temperature results at the specified locations correspond with the measured temperatures from the fire test to a certain level.

In order to investigate the sensitivity of the fuel characteristics in the FDS model, the thermal properties of the wood cribs, i.e. specific heat, ignition temperature, heat of vaporization and heat of combustion, are varied in comparison with the previous model. Table 3.1 summarizes the varying input parameters for each of the investigated scenarios. The results for each of the scenarios listed in Table 3.1 are illustrated in Figures 3.7-3.12.

Table 3.1 Varying input parameters for FDS model

Scenario	Input Parameter					
	Specific heat (kJ/kg-K)	Ignition temperature (°C)	Density (kg/m <sup>3</sup> )	Heat of vaporization (kJ/kg)	Heat of combustion (kJ/kg)	Ignition source (kW/m <sup>2</sup> )
<b>A</b>	1.50 2.57 3.50	300	600	1800	12000	400
<b>B</b>	2.57	250 300 320 350	600	1800	12000	400
<b>C</b>	2.57	300	500 600 700	1800	12000	400
<b>D</b>	2.57	300	600	1200 1800 2200 2400	12000	400
<b>E</b>	2.57	300	600	1800	10000 11000 12000 14000	400
<b>F</b>	2.57	300	600	1800	12000	100 200 300



It is seen from Figure 3.7 that the increasing specific heat results in a lower heat release rate of the fuel, as observed from the more gradual rise in the temperature-time curves at all the measurement points. Nevertheless, the maximum temperature of the burning fuel measured at all points remains comparably unchanged with respect to the varying specific heat.

For the ignition temperature, Figure 3.8 also shows that the increase in the ignition temperature leads to a lower heat release rate of the fuel. It is seen that for the ignition source of  $400 \text{ kW/m}^2$  the fire cannot be initiated when the ignition temperature of the fuel is set to  $350^\circ\text{C}$ . Further, the maximum temperature of the resulting fire is not affected by the varying ignition temperature, as observed from Figure 3.8 for Point 3, the middle point, whereas the maximum temperatures at other points slightly fluctuate due to fire turbulence.

Figure 3.9 illustrates the FDS temperature results from varying the heat of vaporization for the fuel source. It is found that the heat of vaporization is inversely proportional to the heat release rate of the fuel. The ignition source of  $400 \text{ kW/m}^2$  fails to initiate the fire when the heat of vaporization for the fuel is set to  $2400 \text{ kJ/kg}$ . In other words, the ignition source cannot vaporize the fuel. It is also observed that the maximum temperature is lowered with respect to the increasing heat of vaporization. The maximum temperature is  $650^\circ\text{C}$  for the heat of vaporization of  $1200 \text{ kJ/kg}$ .

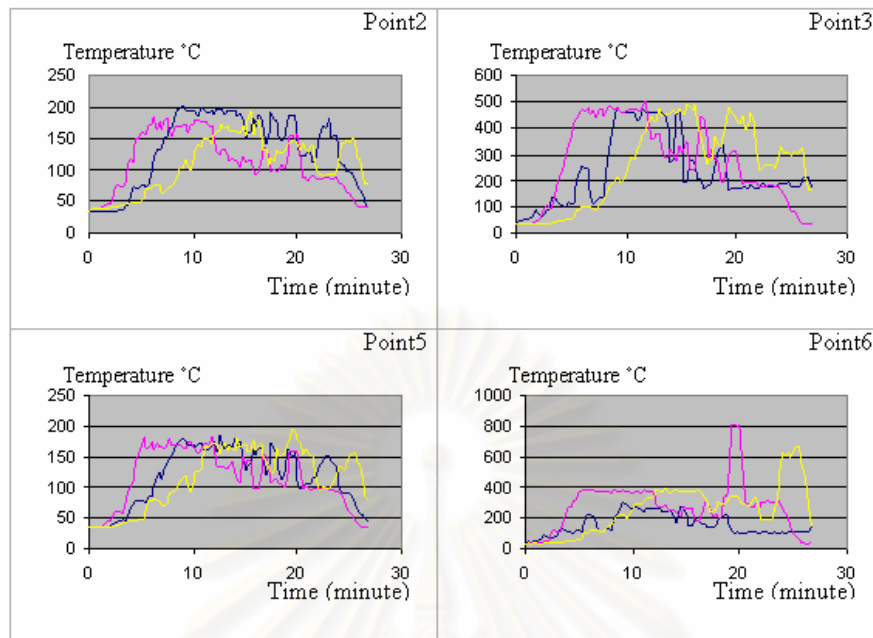
Figure 3.10 represents the scenario in which the heat of combustion for the fuel is varied. It is evident that the heat of combustion is directly proportional to the heat release rate of the fuel. The maximum temperature of the simulated fire, measured at point 3, is as high as  $565^\circ\text{C}$  for the heat of combustion of  $14000 \text{ kJ/kg}$ . Furthermore, the ignition source of  $400 \text{ kW/m}^2$  is not sufficient for fire initiation for the heat of combustion of  $10000 \text{ kJ/kg}$ .

The FDS temperature results for the variation of fuel density are shown in Figure 3.11. It is not clear upon the impact of the density because of the complicated effects from fuel disintegration when burning. If the fuel density is low, a quicker disintegration is expected and thus a high heat release rate at the early time. In any case, it is apparent from Figure 3.11 that the variation of the fuel density does not affect the maximum temperature from burning.

In Figure 3.12, the variation of the heat release rate of the ignition source is examined. It is found that the heat release rate of the ignition source has minor impacts upon the slope of the temperature-time curve as well as the maximum temperature.

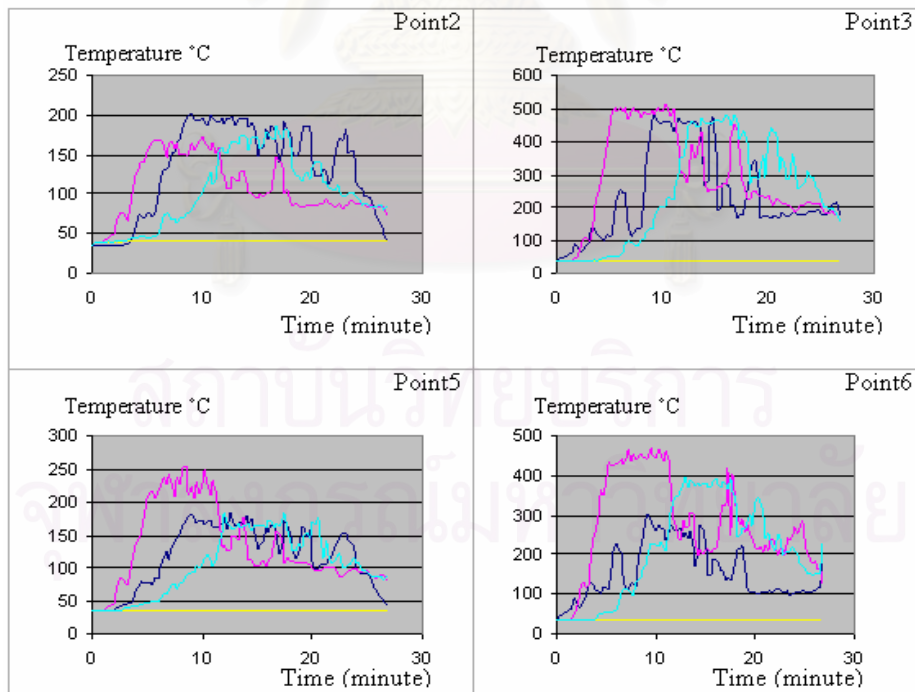
Based on the results of the preliminary simulation studies in this part, it can be concluded that the behavior of the modeled fire is sensitive to the FDS input parameters that govern the fuel characteristics. In the subsequent investigations, the values of these parameters are selected carefully to account for the sensitivities of the outcome of FDS due to these input parameters.





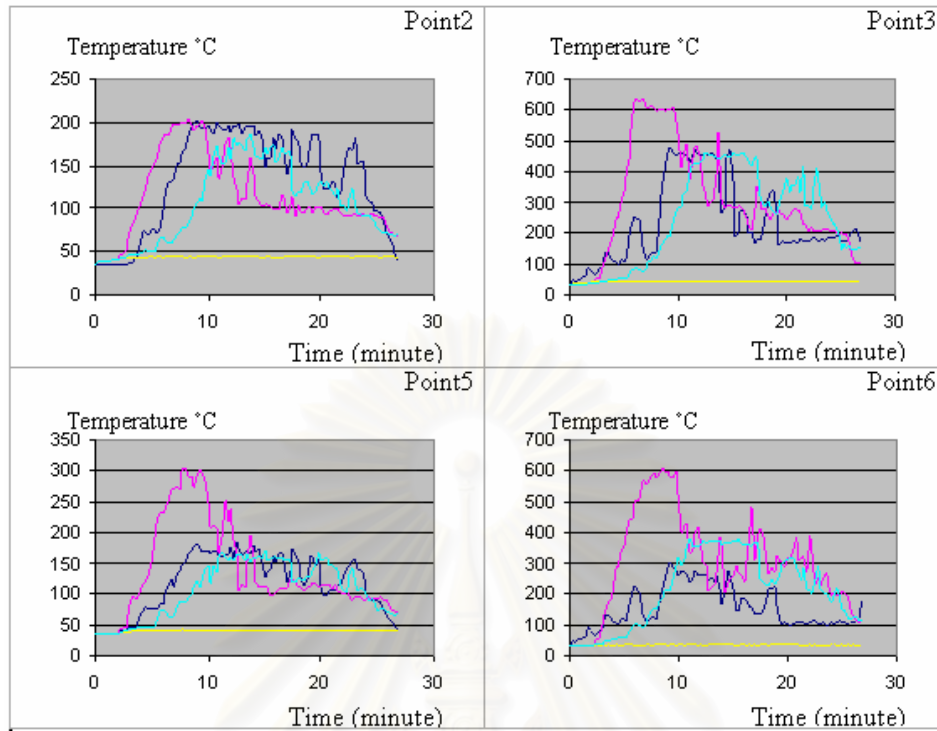
Specific heat: — 1.50 kJ/kg-K — 2.57 kJ/kg-K — 3.50 kJ/kg-K

Figure 3.7 FDS temperature results for scenario A



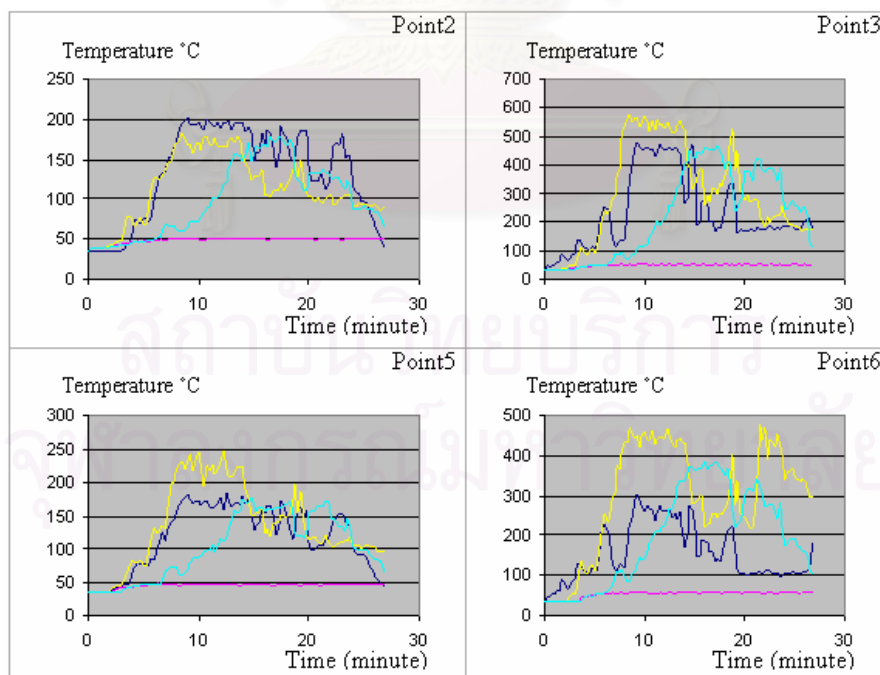
Ignition temperature: — 250 °C — 300 °C — 320 °C — 350 °C

Figure 3.8 FDS temperature results for scenario B



Heat of vaporization: — 1200kJ/kg — 1800kJ/kg — 2000kJ/kg — 2200kJ/kg

Figure 3.9 FDS temperature results for scenario C



Heat of combustion: — 10000kJ/kg — 11000kJ/kg — 12000kJ/kg — 14000kJ/kg

Figure 3.10 FDS temperature results for scenario D

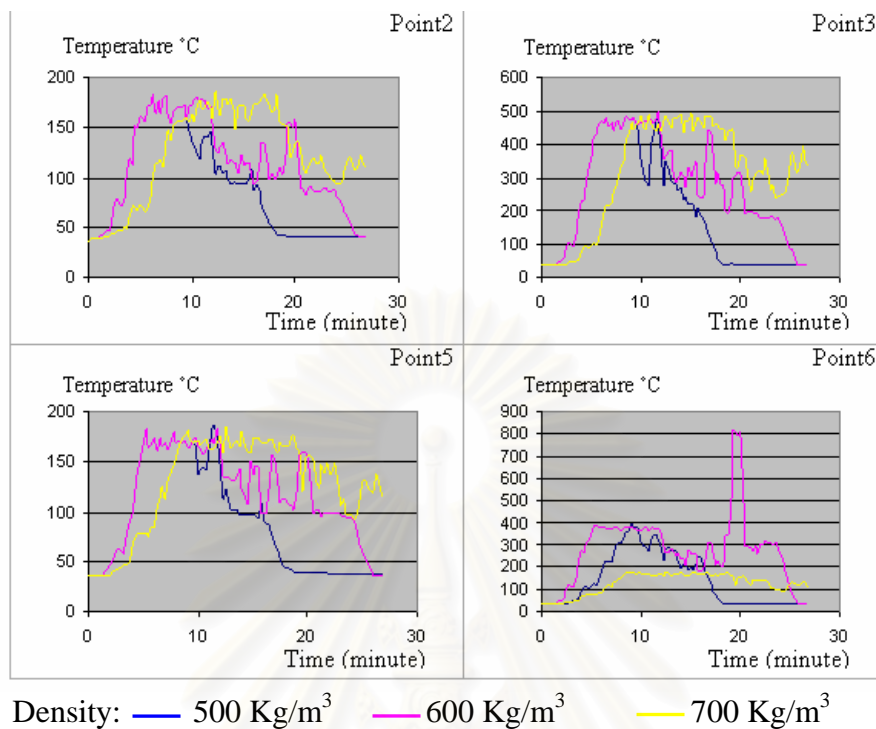


Figure 3.11 FDS temperature results for scenario E

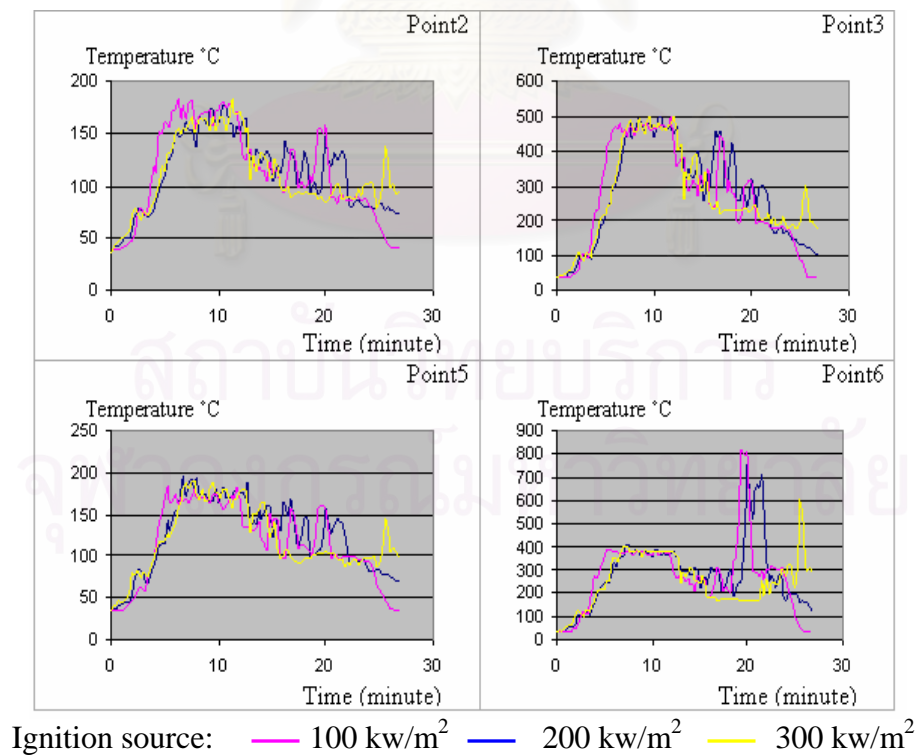


Figure 3.12 FDS temperature results for scenario F

### 3.3 Analysis of Heat Transfer for Steel Sections: Lumped Mass Approach and Finite Element Method

As mentioned in the previous chapter, the lumped mass approach is used to estimate the temperature of the steel sections composing the roof structure from the surrounding temperature obtained from the FDS program. The method is a one-dimensional heat flow analysis that accounts for the section factor,  $H_p/A$ , of the steel section as well as the properties of the insulation. The temperature values computed using the lumped mass approach are input at the nodal points of each element in the structural analysis process. The input element temperature is taken as the average of the nodal temperatures. Because only a single value of temperature can be input at each joint, the current study assumes the section factor for all elements interconnecting at a joint to be  $300 \text{ m}^{-1}$ —an average value of the different section factors of the key elements – for the calculation of the input temperature. The validity of this assumption will be further investigated.

The different steel sections used in the current study are summarized in Table 3.2. All steel sections are subjected to four-sided exposure to fire, except for the C-shape sections, with roofing elements on top, in which the three-sided exposure is considered. The steel temperatures are estimated by using Equations (2.9) and (2.16) for unprotected and protected steel, respectively.

For the current study the thermal properties of perlite-based material (Asthawud, 2002) are used in modeling the fire protection of steel. The thermal properties of steel and the fire protection can be summarized below.

#### Fire Protection

Specific heat	:	980	J/kg-K
Thermal conductivity	:	0.11	W/m-K
Density	:	900	kg/m <sup>3</sup>
Thickness	:	0.02	m

#### Steel

Specific heat	:	Equation (2.18)
Density	:	7850 kg/m <sup>3</sup>
Section factor ( $H_p/A$ )	:	300 m <sup>-1</sup>

The input temperatures from the surrounding fire in the present simulation studies are obtained using the FDS program with the fire modeling parameters specified in cases II-AL and II-BL of Table 4.1 (see Chapter 4). The temperature estimation using the spreadsheet method with section factor of the  $300 \text{ m}^{-1}$  is compared with 2D finite element models for sections 1-4 for the cases with and without fire protection. The temperature at point A in Figure 3.13 is employed as the input temperature. The 2D finite element models for the various steel sections investigated are illustrated in Figure 3.14.

Table 3.2 Various steel sections in the structural model

No.	Section	Dimension (mm)	Area, $A$ (cm <sup>2</sup> )	Perimeter, $H_p$ (cm)	Section factor, $H_p/A$ (m <sup>-1</sup> )
1	Pipe	89.1x4	10.68	27.97	261
2	Pipe	60.5x3.2	5.75	19.00	329
3	Pipe	48.6x3.2	4.56	15.26	334
4	C-shape	125x50x3.2	11.92	40.50	340

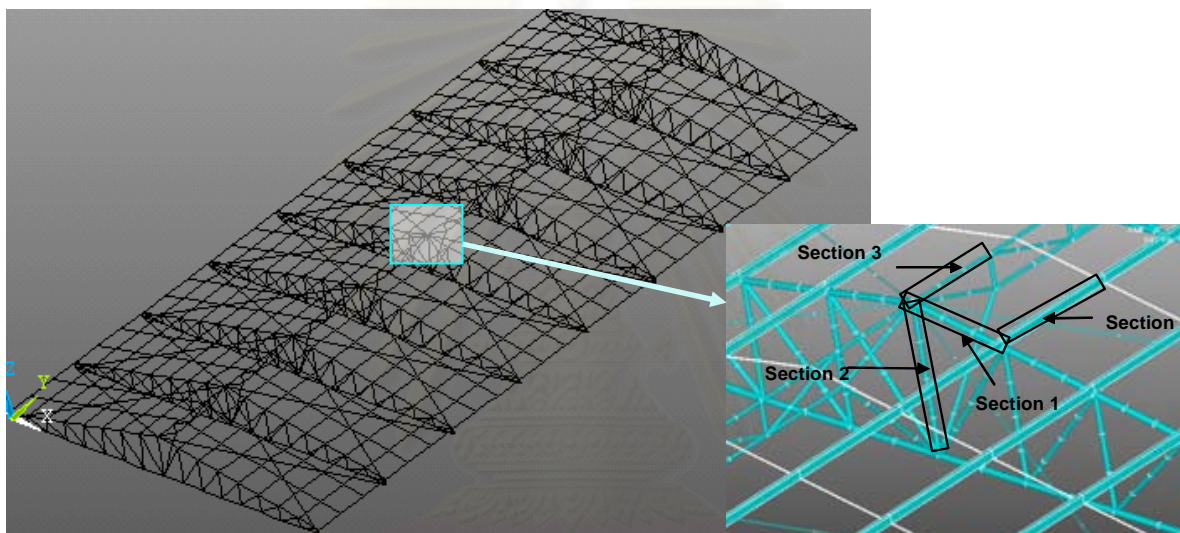


Figure 3.13 Location of point A

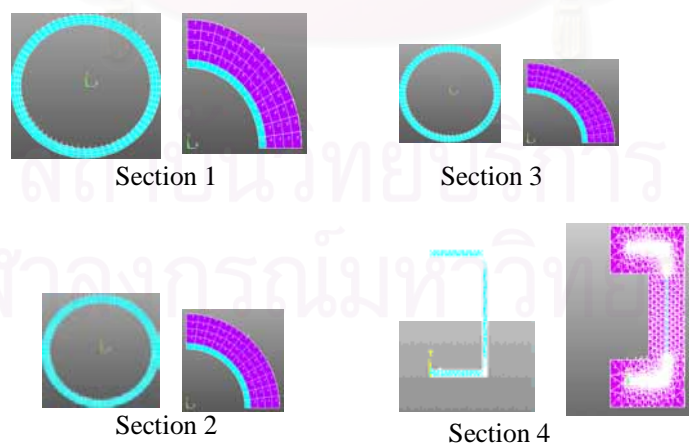


Figure 3.14 2D finite element models for different sections with and without fire protection



The temperature results obtained from using the lumped mass approach with  $H_p/A=300 \text{ m}^{-1}$  are plotted in comparison with the average steel temperatures from the 2D finite element models in Figure 3.15. The high  $H_p/A$  sections results in the high temperature at the same time for 2D finite element models. The deviation of the steel temperature computed using the lumped mass approach with  $H_p/A=300 \text{ m}^{-1}$  from those computed using the 2D finite element models at any time step is within 5% of the fire temperature for section 1-4, with and without fire protection.

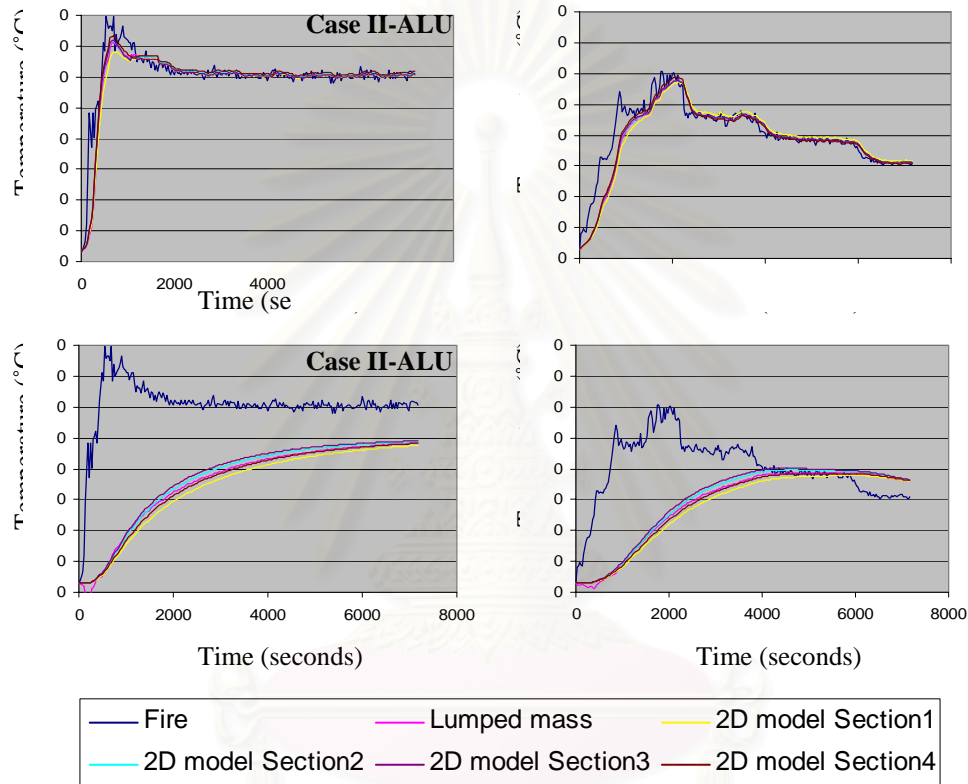


Figure 3.15 Comparison of the variation of steel temperatures with respect to time for Cases II-AL and II-BL using the lumped mass approach and 2D finite element models

To investigate the accuracy of computing the element temperature by averaging the temperature at nodal points, the 3D finite element models for the four steel sections are constructed in comparison with the lumped mass approach using  $H_p/A=300 \text{ m}^{-1}$ , Figure 3.16 illustrates example of the 3D finite element model. The temperature results obtained from using the lumped mass approach with  $H_p/A=300 \text{ m}^{-1}$  are plotted in comparison with the average steel temperatures from the 2D finite element models in Figure 3.17-3.18.



It is found that the deviations of the element temperature computed using the lumped mass approach from the average element temperature obtained from the 3D finite element models fall within 5% of the fire temperature at any time step for section 1, 2 and 3, with and without fire protection, while the deviations are 7% for section 4 with and without fire protection, respectively. This underestimation of the temperature of section 4 (i.e. purlins section) by the lumped mass approach is noted that it is viewed acceptable since section 4 is not considered the key component of the structural system.

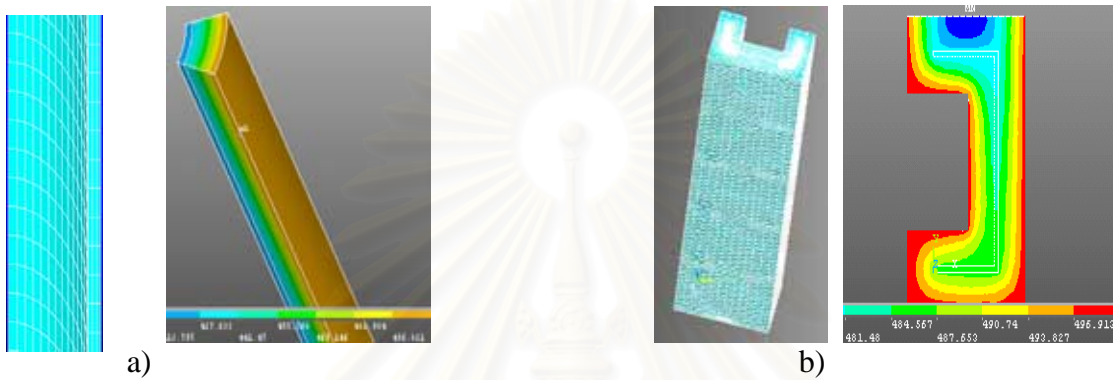


Figure 3.16 3D finite element model: a) Pipe section b) C-shape section

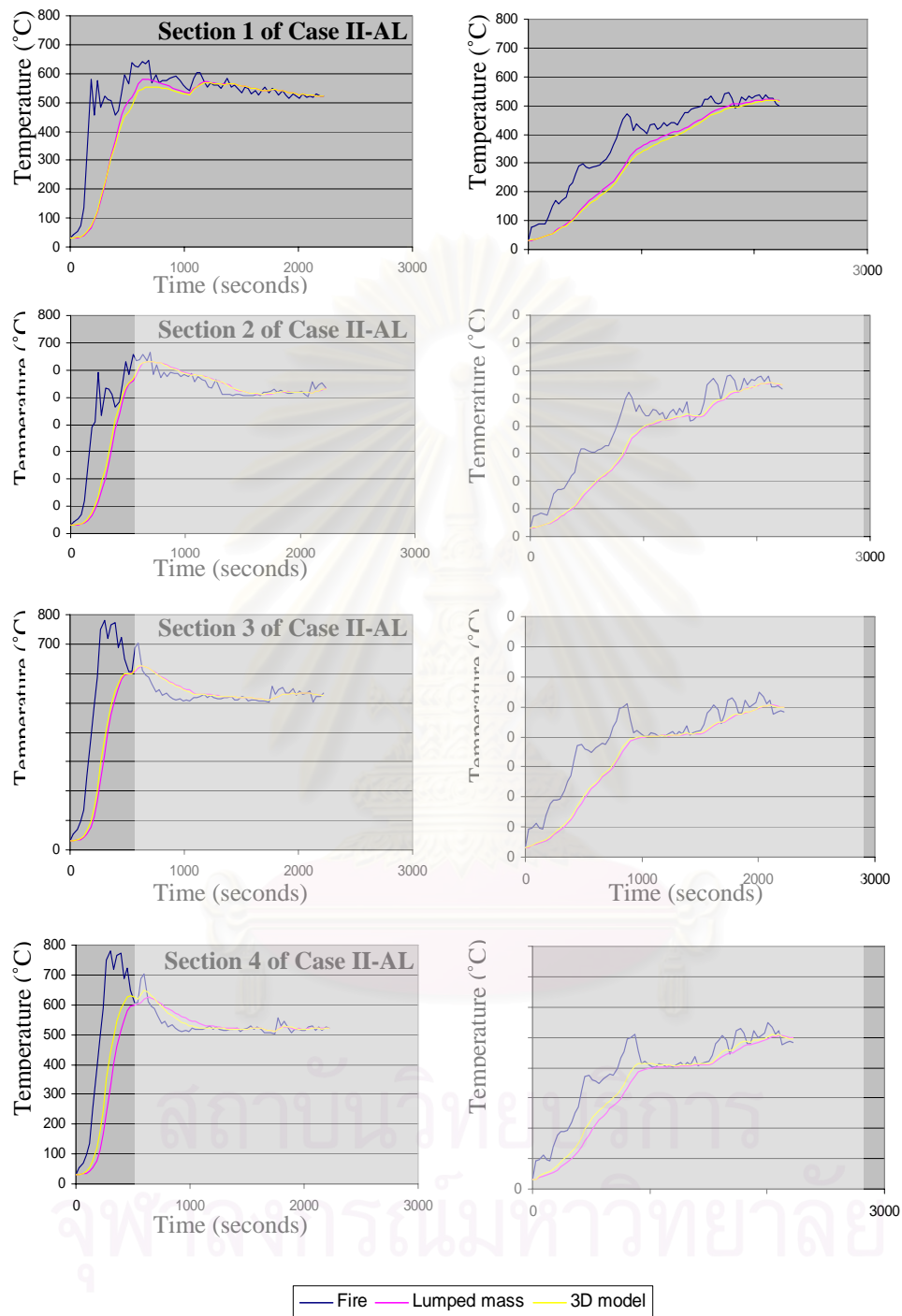


Figure 3.17 Comparison of the variation of temperatures for steel without fire protection with respect to time for Cases II-AL and II-BL using the lumped mass approach and 3D finite element models

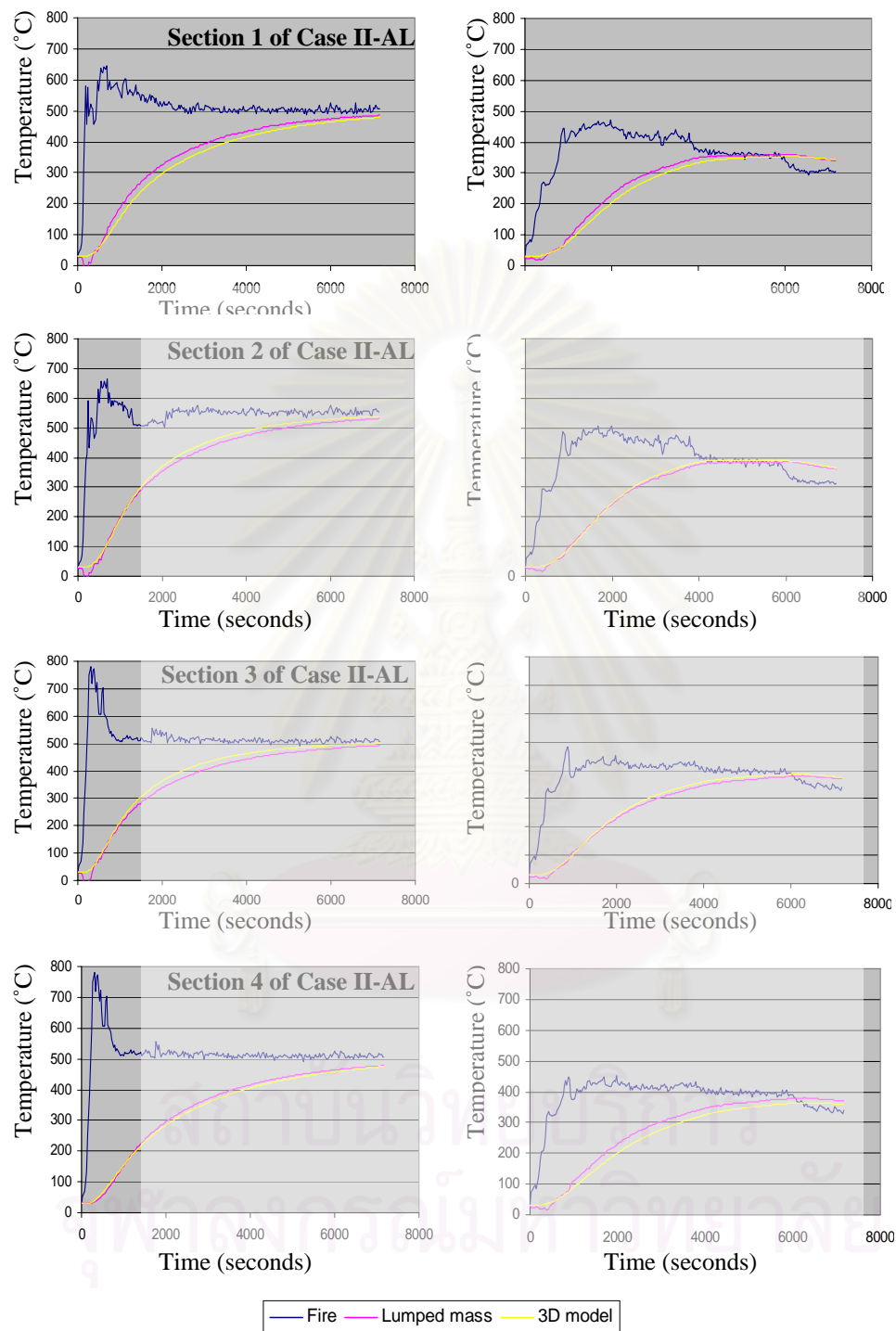


Figure 3.18 Comparison of the variation of temperatures for steel with fire protection with respect to time for Cases II-AL and II-BL using the lumped mass approach and 3D finite element models

## CHAPTER IV

### SIMULATION STUDIES

#### 4.1 Introduction

To investigate the effects of fire upon steel frames, various fire scenarios are simulated for a typical warehouse with a system of steel roof frames that are commonly found in most warehouse structures. The steel roof structure is analyzed with and without fire protection under the distinct fire scenarios investigated. The analysis links between fire modeling using the FDS program and the structural analysis using a nonlinear finite element method in order to assess the safe egress time from the structure prior to its failure. This chapter discusses the parameters involved in fire modeling and structural modeling as well as the assumptions and the limitations of the analyses. The results obtained from fire modeling and structural analyses are also examined.

#### 4.2 Fire Modeling Parameters

For the present simulation studies, a typical warehouse with a 20 m x 40 m layout is investigated. The warehouse contains 18 piles of storage contents. The dimensions of each storage pile are 4 m in width, 4 m in length and 3 m in height. The spacing between the storage piles is 2 m in both horizontal directions. The ventilation openings of the warehouse are located along the wall, taking up the area of 140 m<sup>2</sup>. Figure 4.1 illustrates the geometry of the warehouse as modeled by the FDS program.

The current study investigates two types of fuel (i.e., warehouse contents) in fire modeling: wood and plastic. The thermal properties of these two fuel types are obtained from the FDS database which can be summarized in Table 4.1. Note that the ambient temperature is set at 30 °C.

Table 4.1 Thermal properties of wood and plastic content

Plastic contents		Wood content	
Type:	Standard plastic commodity	Type:	Pine wood
Heat release rate	500 kJ/kg	Heat of vaporization	2500 kJ/kg
Specific heat	1.0 kJ/kg-K	Heat of combustion	12044 kJ/kg
Ignition temperature	370 °C	Thermal conductivity	0.14 W/m-K
		Thermal diffusivity	8.3E-8 m <sup>2</sup> /s
		Ignition temperature	390 °C

The values of the clearance height of the roof structure above ground are taken as 8 m and 10 m. The ignition source is considered to locate at different areas of the warehouse as illustrated in Figure 4.2

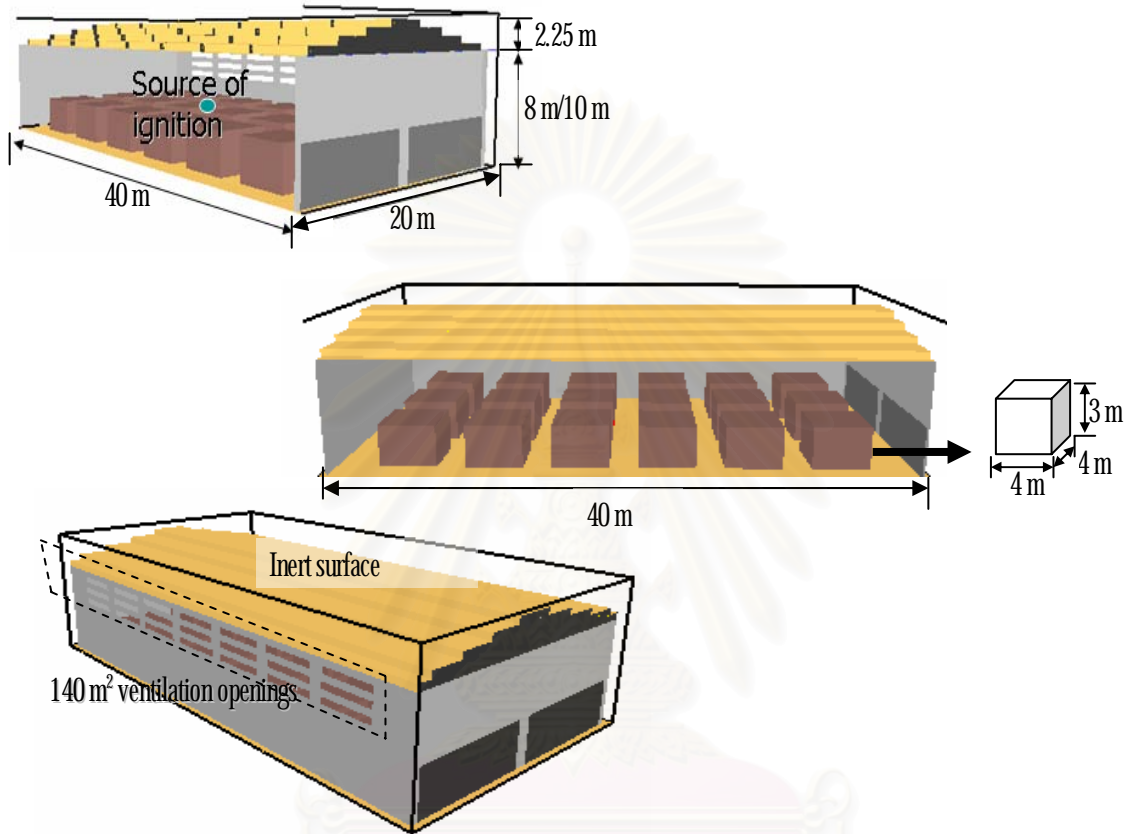


Figure 4.1 FDS simulated warehouse

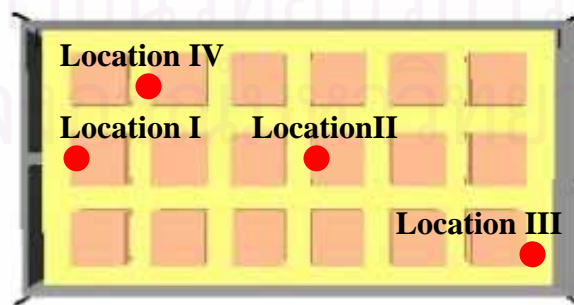


Figure 4.2 Various locations of the ignition source

The variation of each of the above parameters essentially characterizes the distinct fire scenarios investigated in the current simulation studies. These scenarios are summarized in Table 4.2 using the code illustrated in Figure 4.3

In modeling the fire scenarios, the enclosure within and outside of the warehouse is simulated using the FDS program. Because of the limitations of the computer program, all calculations must be performed within a domain that is made up of rectangular blocks, each with its own rectilinear grid. All obstructions and vents are thus forced to conform with the numerical grid(s) established by the user. In the current study a 0.5 m grid spacing is used, resulting in a model as shown in Figure 4.4. Therefore, the roof frames are modeled as thin plate obstructions with edges that align with the specified grid lines and the slope of the roof as shown in Figure 4.5.

Table 4.2 Various fire scenarios investigated in the simulation studies

Fire Protection		Protected				Unprotected			
		8 m		10m		8m		10m	
Height of Warehouse		Plastic	Wood	Plastic	Wood	Plastic	Wood	Plastic	Wood
Fuel Type		Plastic	Wood	Plastic	Wood	Plastic	Wood	Plastic	Wood
Locations of Ignition Source	I	I-ALP	I-BLP	I-AHP	I-BHP	I-ALU	I-BLU	I-AHU	I-BHU
	II	II-ALP	II-BLP	II-AHP	II-BHP	II-ALU	II-BLU	II-AHU	II-BHU
	III	III-ALP	III-BLP	III-AHP	III-BHP	III-ALU	III-BLU	III-AHU	III-BHU
	IV	IV-ALP	IV-BLP	IV-AHP	IV-BHP	IV-ALU	IV-BLU	IV-AHU	IV-BHU

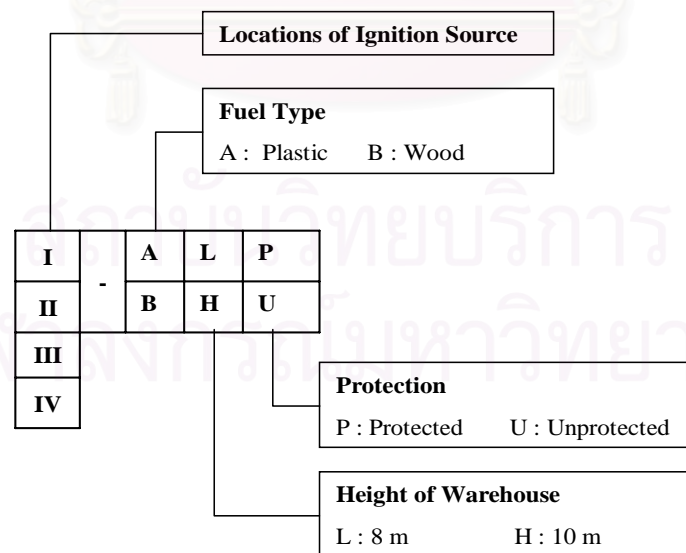


Figure 4.3 Coding representation of varying parameters



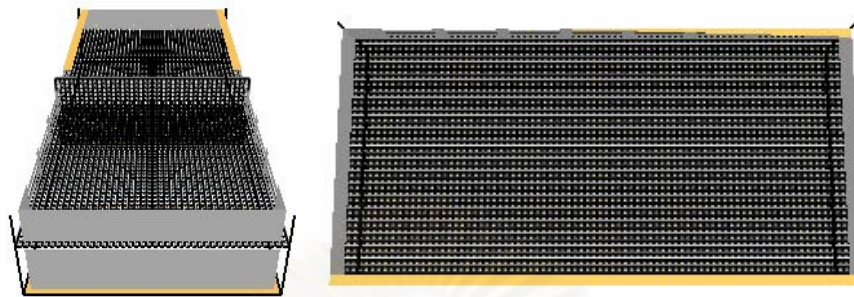


Figure 4.4 Grids of FDS simulated warehouse

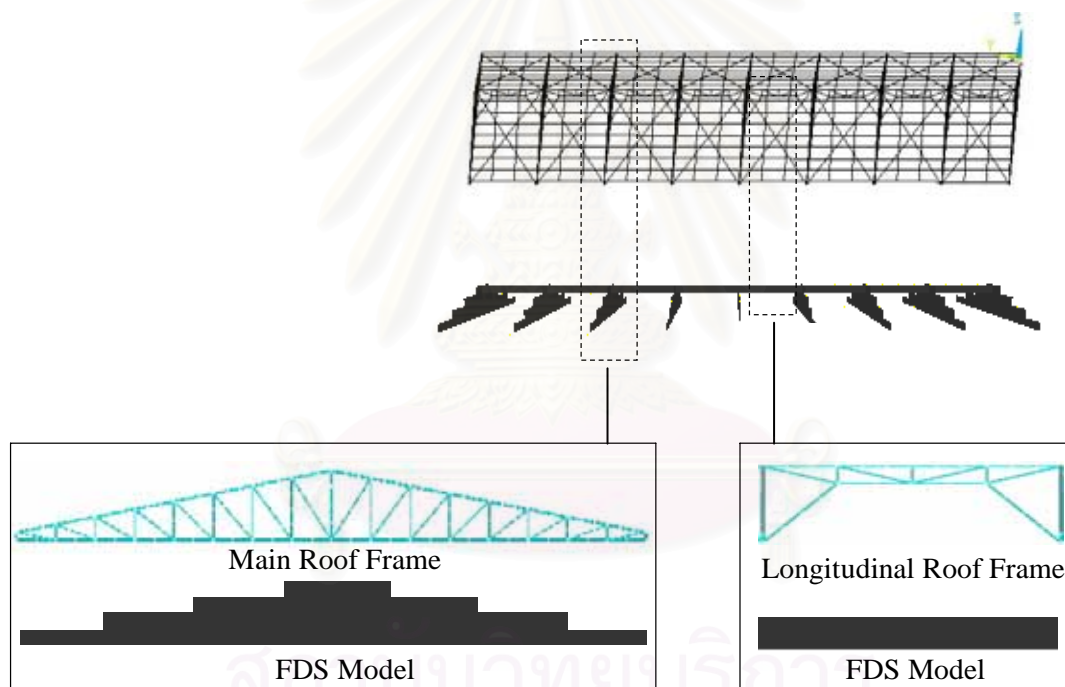


Figure 4.5 FDS model of the roof frames

The output of the FDS program is mainly the temperature distribution of air inside the specified enclosure. The temperature data are collected at the nodal points (i.e., joints) of all the members of the roof structure. Note that because the roof frames are modeled as thin plates the heat transfer in steel frames is not considered in the FDS model. The temperature data are taken at the surface of the thin plates, i.e. the air temperature. The heat transfer from the surrounding air to the structural steel members is computed using Equations (2.9) and (2.16) for members with and without fire protection, respectively.

The comparison of the structural performance under different fire scenarios is based upon the same initiating time line, i.e. the instant in which the fuel reaches its flaming point. This is done through the modification of the source of ignition to allow the fuel to become flammable instantly.

### 4.3 Structural Modeling Parameters and Criteria for Structural Analysis

The structural model of the steel roof that is used in the nonlinear finite element analysis is a frame structure consisting of steel pipes for the main span, steel rods for bracing members, and C-shape section for purlins. The supports of the main roof frames are hinges and  $X$ -direction rollers. For the current simulation studies, fire loading is imposed upon the structure in conjunction with the self weight and the  $30 \text{ kg/m}^2$  superimposed load. The average temperature of the joints at the end of each element is taken as the element temperature. The finite element model of the roof structure consist of, the roof elements are meshed to 2934 elements and 2935 nodes. Each of the element nodes is characterized by six degrees of freedom shown in Figure 2.4. The roof structure model, element and node of the structure are illustrated in Figure 4.6 and 4.7.

Under the high-temperature condition, the variation in the mechanical properties of steel, i.e. the modulus of elasticity and the coefficient of thermal expansion, as summarized in Table 2.1, are used in the analysis. Note that the strength hardening property of steel is excluded from the current analysis. And the compressive strength limitation by buckling applies ANSI/AISC 360-05.

From the limiting width-thickness ratios table, the pipe section and web of channels are classified as compact and the flange of channels is classified as noncompact. Thus the buckling examination in this research is considered as follows:

#### Circular pipe sections

- Compressive stress checks against for flexural buckling from Equations (2.20) and (2.21).

#### Purlins C-sections

- Compressive stress checks against for flexural buckling from Equations (2.20) and (2.21) and for torsional and flexural-torsional buckling from Equation (2.22).
- Moment checks against for Lateral-torsional buckling from Equations (2.23) and (2.24).

Table 4.3 shows the section properties required for buckling calculations. The compressive strength limitation is in Tables 4.4 and 4.5. The interaction of flexure and compression in doubly symmetric members and singly symmetric members shall be limited by Equations (2.26) and (2.27).

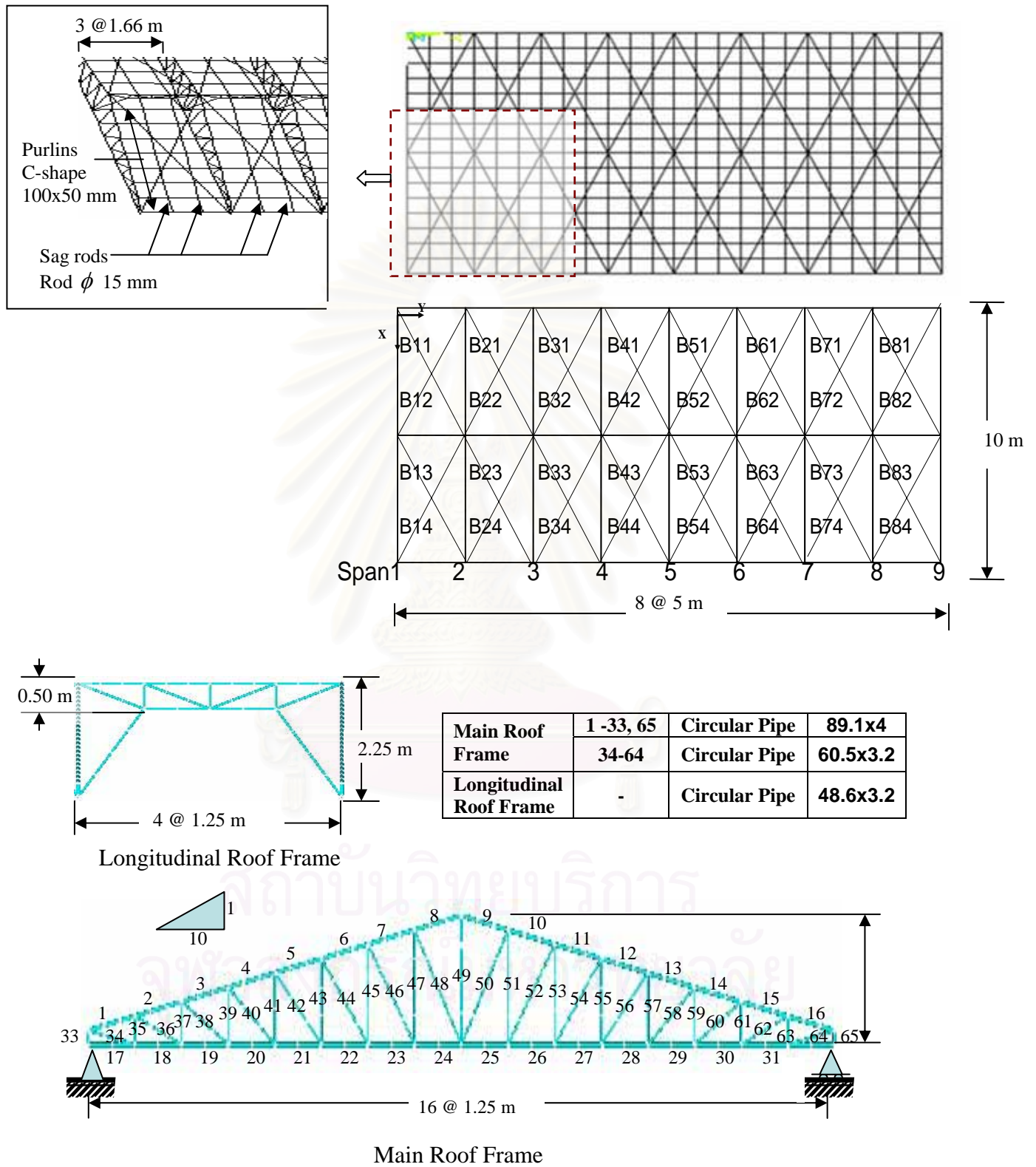


Figure 4.6 Roof structure model of the typical warehouse

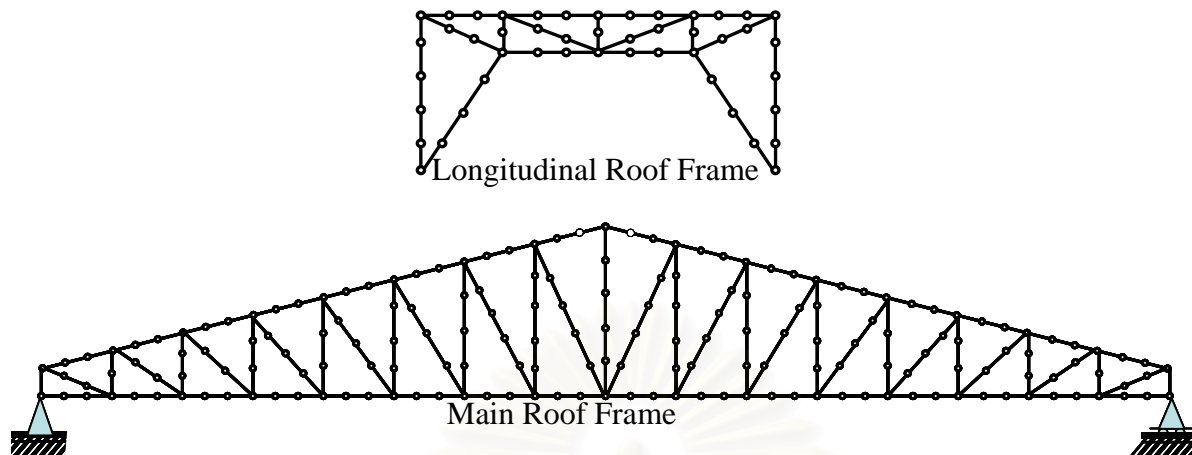


Figure 4.7 Element and node of the structure model

Table 4.3 Section properties for buckling calculations

	Circular Pipe			purlins
	89.1x4	60.5x3.2	48.6x3.2	100x50
$D/t$	22.27	18.90	15.19	-
$b/t$	-	-	-	6.67
$h/t_w$	-	-	-	20.00
$I_x$ (cm <sup>4</sup> )	96.97	23.70	11.81	189.00
$I_y$ (cm <sup>4</sup> )	96.97	23.70	11.81	26.90
$s_x$ (cm <sup>3</sup> )	21.77	7.83	4.86	37.80
$s_y$ (cm <sup>3</sup> )	21.77	7.83	4.86	7.82
$r_x$ (cm)	3.01	2.03	1.61	3.98
$r_y$ (cm)	3.01	2.03	1.61	1.50
$K$	0.65	0.65	0.65	1

Table 4.4 Buckling strength and plastic moment of circular pipe sections

Temp (°C)	$E$ (kg/m <sup>2</sup> )	$F_y$ (10 <sup>7</sup> kg/m <sup>2</sup> )	Flexural Buckling Stress $F_{cr}$ (10 <sup>7</sup> kg/m <sup>2</sup> )													Plastic Moment $M_p$ (10 <sup>2</sup> kg.m)		
			89.1x4		60.5x3.2								48.6x3.2			89.1x4	60.5x3.2	48.6x3.2
			L=0.25m	L=1.25m	L=0.5m	L=0.75m	L=1m	L=1.25m	L=1.5m	L=1.75m	L=2m	L=2.25m	L=2.25m	L=1.35m	L=2.15m	L=1.66m	L=1.66m	L=1.66m
20	2.1E+10	2.40	2.40	2.32	2.37	2.33	2.28	2.22	2.15	2.06	1.97	1.87	2.12	2.08	1.67	6.63	2.39	1.48
93	2.1E+10	2.40	2.40	2.32	2.37	2.33	2.28	2.22	2.15	2.06	1.97	1.87	2.12	2.08	1.67	6.63	2.39	1.48
204	1.89E+10	2.40	2.40	2.31	2.37	2.33	2.27	2.20	2.12	2.03	1.92	1.81	2.09	2.04	1.60	6.63	2.39	1.48
316	1.64E+10	2.40	2.40	2.29	2.36	2.32	2.25	2.17	2.08	1.97	1.86	1.74	2.05	2.00	1.50	6.63	2.39	1.48
399	1.47E+10	2.40	2.40	2.28	2.36	2.31	2.24	2.15	2.05	1.93	1.81	1.67	2.01	1.95	1.42	6.63	2.39	1.48
427	1.41E+10	2.26	2.25	2.15	2.22	2.17	2.10	2.02	1.93	1.82	1.71	1.58	1.90	1.84	1.35	6.24	2.25	1.39
538	1.03E+10	1.58	1.58	1.51	1.56	1.53	1.48	1.43	1.36	1.29	1.21	1.13	1.34	1.30	0.97	4.38	1.58	0.98
649	4.62E+09	0.84	0.84	0.79	0.82	0.80	0.78	0.74	0.70	0.66	0.61	0.56	0.69	0.67	0.47	2.32	0.84	0.52
760	2.31E+09	0.38	0.38	0.36	0.38	0.37	0.36	0.34	0.33	0.31	0.29	0.27	0.32	0.31	0.23	1.06	0.38	0.24
871	1.47E+09	0.17	0.17	0.16	0.17	0.16	0.16	0.16	0.15	0.14	0.14	0.13	0.15	0.15	0.12	0.46	0.17	0.10



Table 4.5 Buckling strength and moment of purlins sections

Temp (°C)	$E$ (kg/m <sup>2</sup> )	$F_y$ (10 <sup>7</sup> kg/m <sup>2</sup> )	$4.71\sqrt{\frac{E}{F_y}}$	$\frac{KL}{r_y}$	$L_b$ (cm)	$L_p$ (cm)	$L_r$ (cm)	FB	FTB	LTB
								$F_{cr}$ (10 <sup>7</sup> kg/m <sup>2</sup> )	$F_{cr}$ (10 <sup>7</sup> kg/m <sup>2</sup> )	$M_n$ (10 <sup>2</sup> kg.m)
20	2.1E+10	2.40	139.32	111.11	166.67	78.09	238.42	1.32	2.18	8.51
93	2.1E+10	2.40	139.32	111.11	166.67	78.09	238.42	1.32	2.18	8.51
204	1.89E+10	2.40	132.17	111.11	166.67	74.08	226.19	1.23	2.15	8.44
316	1.64E+10	2.40	123.05	111.11	166.67	68.97	210.57	1.11	2.12	8.33
399	1.47E+10	2.40	116.57	111.11	166.67	65.34	199.48	1.02	2.09	8.25
427	1.41E+10	2.26	117.62	111.11	166.67	65.93	201.29	0.97	1.97	7.77
538	1.03E+10	1.58	120.05	111.11	166.67	67.29	205.43	0.71	1.39	5.48
649	4.62E+09	0.84	110.46	111.11	166.67	61.91	189.03	0.32	0.72	2.86
760	2.31E+09	0.38	115.52	111.11	166.67	64.75	197.69	0.16	0.33	1.32
871	1.47E+09	0.17	139.32	111.11	166.67	78.09	238.42	0.09	0.15	0.60

FB = Compressive strength for flexural buckling without slender elements  
 FTB = Compressive strength for torsional and flexural-torsional buckling without slender elements  
 LTB = Lateral-torsional buckling



#### 4.4 Fire Modeling Results

Cases II-AL and II-BL are designed primarily to investigate the effect of the fuel type, i.e. plastic and wood contents, with the ignition source located in the middle area of warehouse. Figures 4.8 and 4.9 illustrate that in both cases the hot air layer within the enclosure radiates towards the burning fuel. In addition, the flames rise upward to the ceiling and spread horizontally. It is seen that for the Case II-AL the enclosure temperature rapidly rises in the area above the ignition source. The hot air then flows to the roof of the warehouse and gradually extends to the other parts of the roof. Subsequently, the hot air flows down to the lower layer of the warehouse enclosure, resulting in a considerable feedback of heat to the fuel and hence a rapid fire growth. It is also observed that high temperatures are concentrated near the ventilation openings because enormous amount of oxygen is consumed in these areas.

For Case II-BL, it is observed that the heat feedback from the growing fire is negligible. The fire growth in this case rather occurs through direct radiation from the flames to nearby objects, resulting in a slow fire growth in which the spacing and the surface of the combustibles become significant.

The feedback of heat can be considered from the heat release rate of the fuel as shown in Figure 4.10. The figure illustrates the significant difference of the heat release rate between the two fuel types. It is seen that the heat release rate tends to increase exponentially as the flames get larger and thus radiate more heat back to the fuel. In the burning process, the peak heat release rate is first reached, followed by a steady state due to sufficient ventilation.

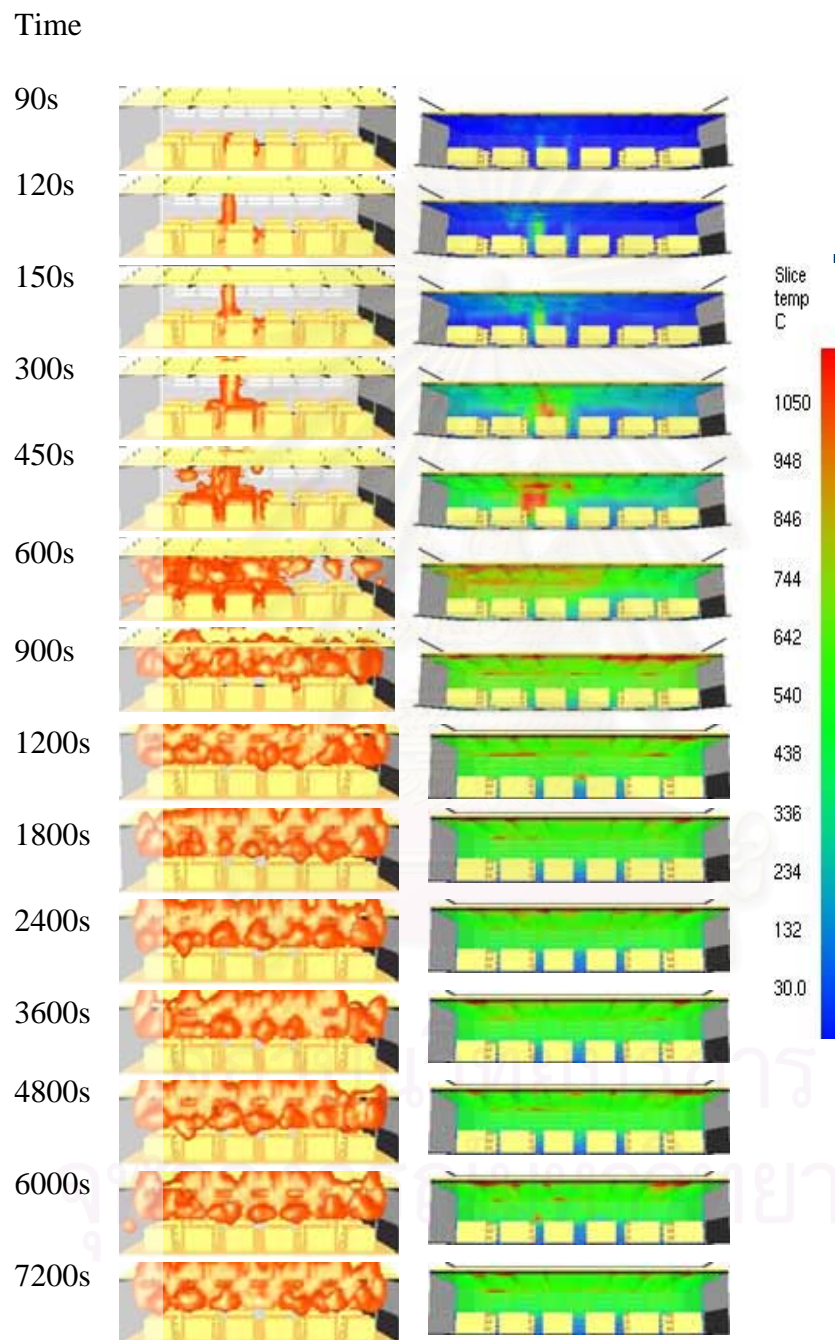


Figure 4.8 Flame spread and enclosure temperature at different time steps for Case II-AL

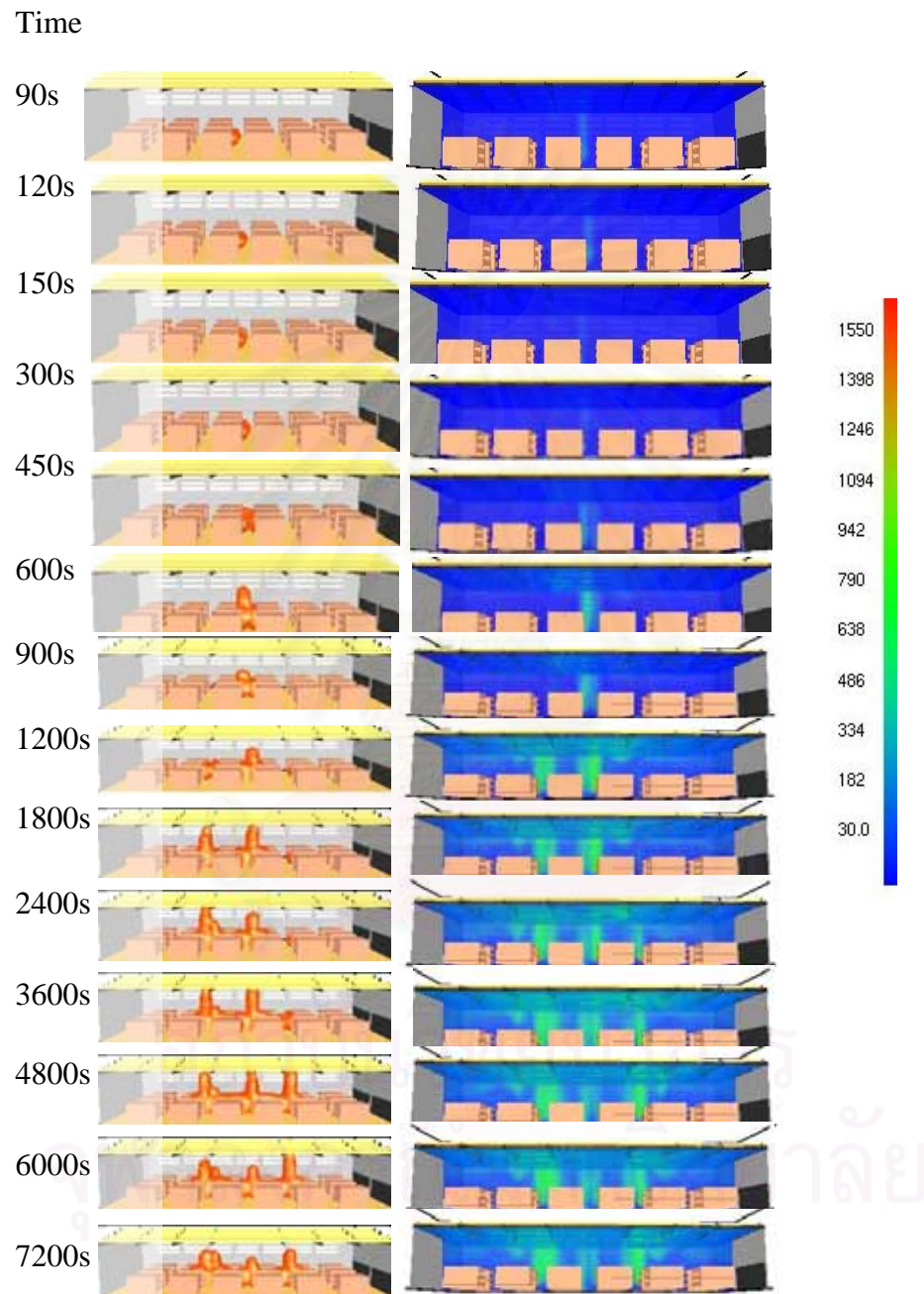


Figure 4.9 Flame spread and enclosure temperature at different time steps for Case II-BL

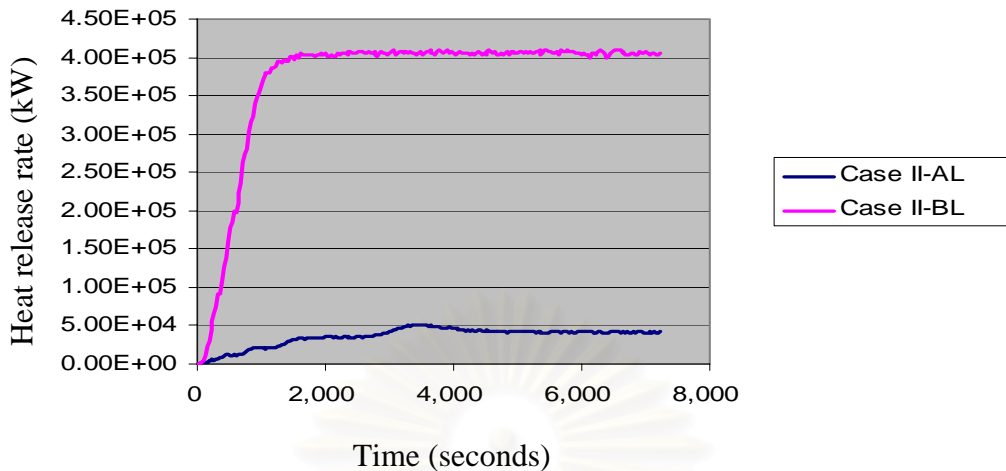


Figure 4.10 Heat release rate of the plastic and wood fuel

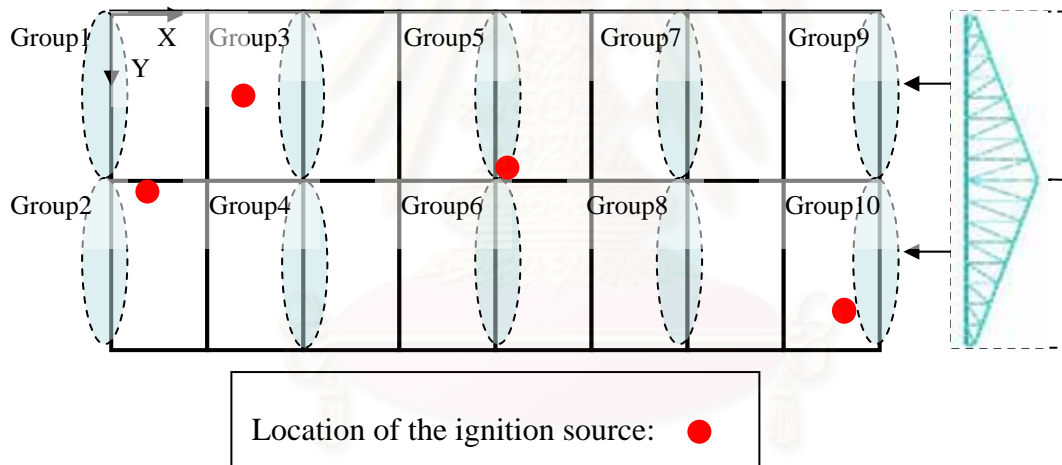


Figure 4.11 Zone areas in the structure plan

The FDS modeled fires at different time steps for the 16 fire scenarios are illustrated in Figures A1-A8. The variation of the average temperature of the different group members (see Figure 4.11) at the nodal points for each group of the roof frame members with respect to time is illustrated in Figures 4.12-4.27.

For the case of plastic storage contents, it is observed that different groups of storage piles located at various areas of the warehouse trend to ignite simultaneously after certain periods of time. This situation is referred to as the “localized flashover”. The area in which the localized flashover can be observed is related to the feedback of heat from the flames. It is found that the flames inside the warehouse with 8-m clearance height are able to rise upward to the roof and spread horizontally underneath, resulting in more feedback of heat and more rapid fire growth compared with the 10-m clearance height. In



addition, when the source of ignition is specified at Location II, the flames are able to spread to nearby objects, resulting in a substantially rapid fire growth and high level of heat feedback. In this case, simultaneous ignition occurs for the entire warehouse contents, both for 8-m and 10-m clearance heights. For the case in which the source of ignition is located near the door of the warehouse (Location I), it is seen that the low level of heat feedback reflected from a single adjacent wall results in a slower fire growth. Only the storage contents in the adjacent areas ignite simultaneously. However, when the ignition source is located in the corner area of the warehouse (Locations III and IV), the stronger fire plumes formed in the corner area are able to reach the roof and spread horizontally underneath more rapidly, igniting more storage contents in the adjacent areas. As such, the warehouse with low clearance height can lead to the localized flashover of the entire storage contents.

The variation of the average temperature of the different group members illustrates the rapidly increasing temperature in all areas of the warehouse for the plastic content cases (see Figures 4.12-4.19). The maximum temperature for each case is found to be in the range of 850-900 °C. The clearance height of the warehouse and the location of the ignition source are observed to slightly affect the maximum temperature. The maximum temperature is reached most rapidly when the source of the ignition is at Location II (i.e., the middle of the warehouse) and the clearance height of the warehouse is 8 m. For the cases in which the entire storage contents are ignited simultaneously, only slight temperature variations are observed for different group members of the roof frames. However, for the fire scenarios with burning objects within certain areas, significant differences of the temperature values are observed between the burning and unburning zones. It is also observed that the variation of the clearance height of the warehouse from 8 m to 10 m produces insignificant effects on the overall temperature distribution of the roof structure.

For the case of wood storage contents, the behavior of the modeled fire is illustrated through Figures 4.20-4.27. Because of the slow heat release rate of the woods, only a low level of heat is feedback to nearby objects. As a result, the fire growth in this case rather occurs through direct radiation from the flames. Because slow fire growth is observed for all of the scenarios using wood storage contents, it is concluded that the ignition source and the clearance height of the warehouse are not the key factors to the behavior of the modeled fire. It can be observed from Figures 4.20-4.27 that significant temperature differences occur between the burning and unburning zones. High temperature values can be recorded only in the proximity of the location of the ignition source. These temperature differences are found to be in the range of 100-150 °C.

Note that the average temperature values for the roof frame members in Groups 1, 2, 9 and 10 are relatively low compared with the other groups because these group members are modeled to contact the surrounding air directly.

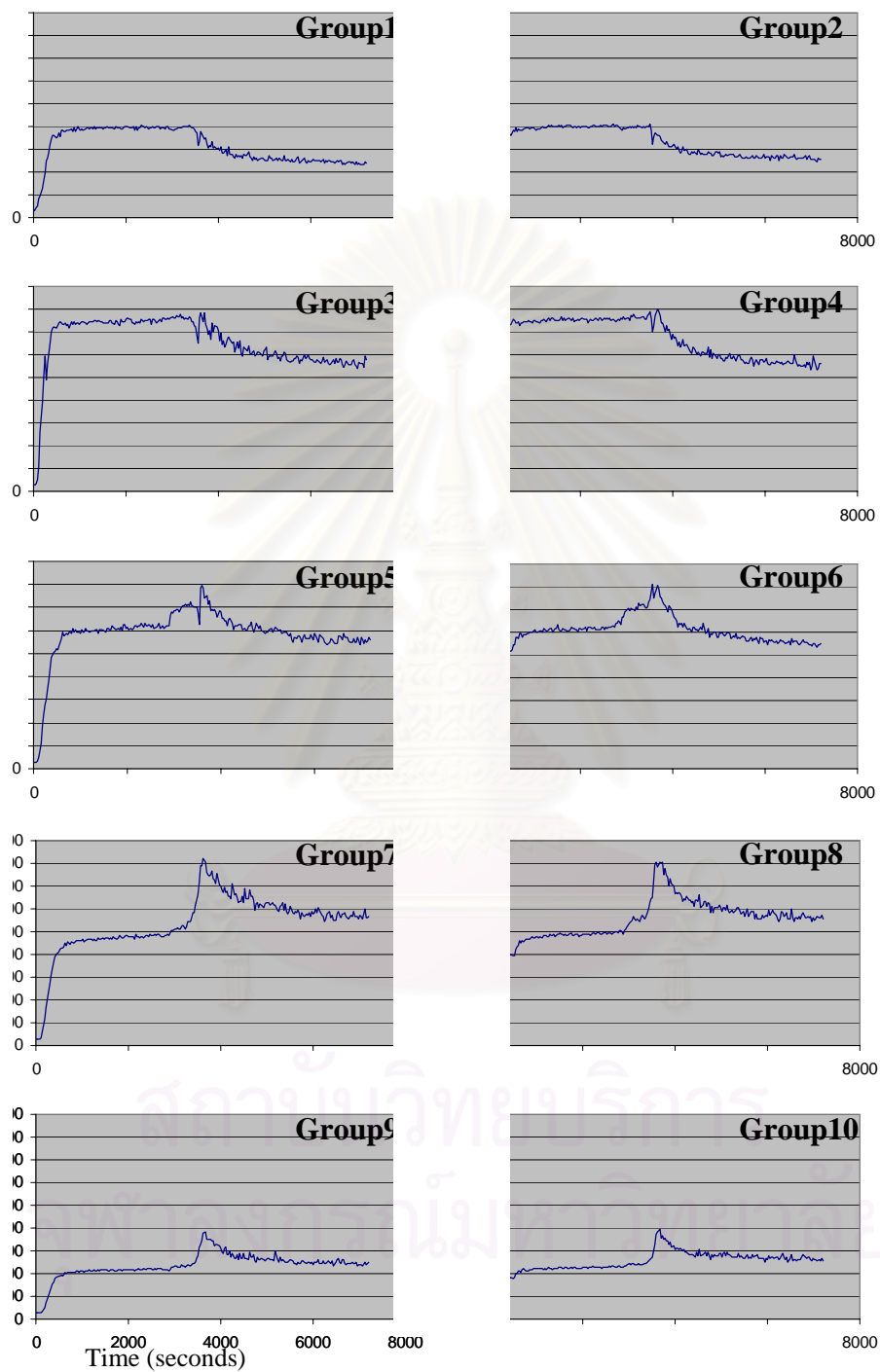


Figure 4.12 Temperature distribution for Case I-AL



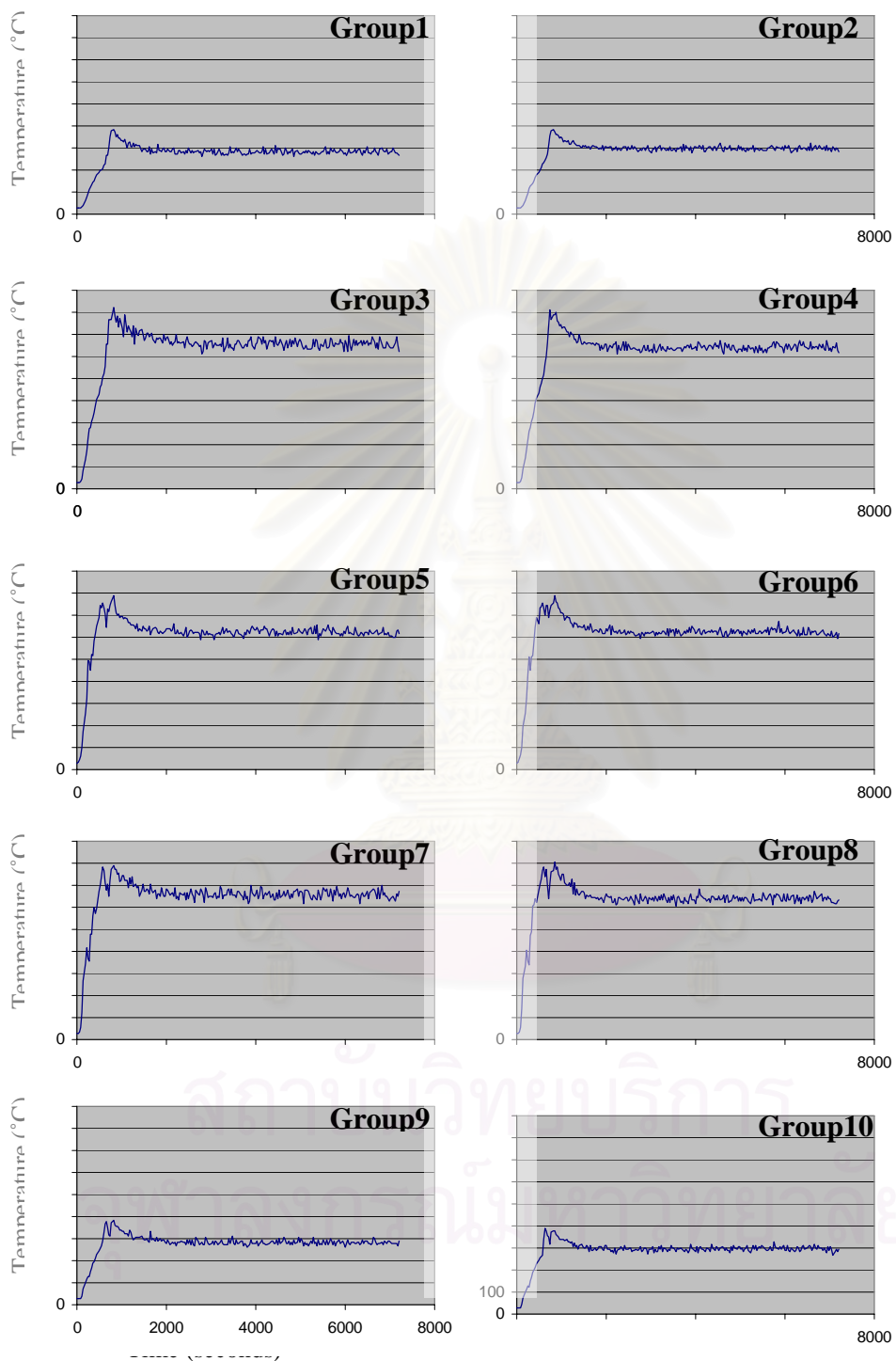


Figure 4.13 Temperature distribution for Case II-AL

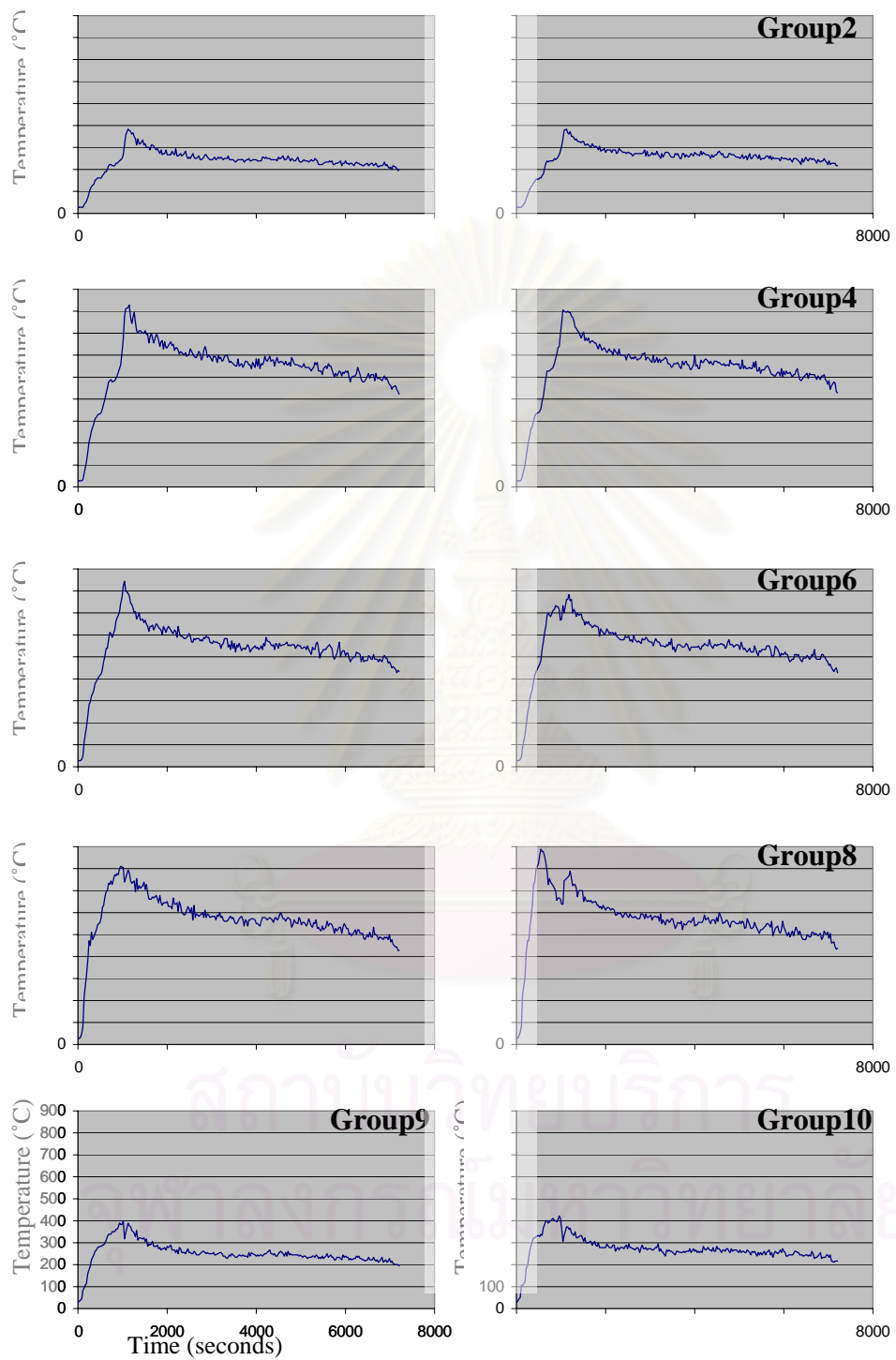


Figure 4.14 Temperature distribution for Case III-AL

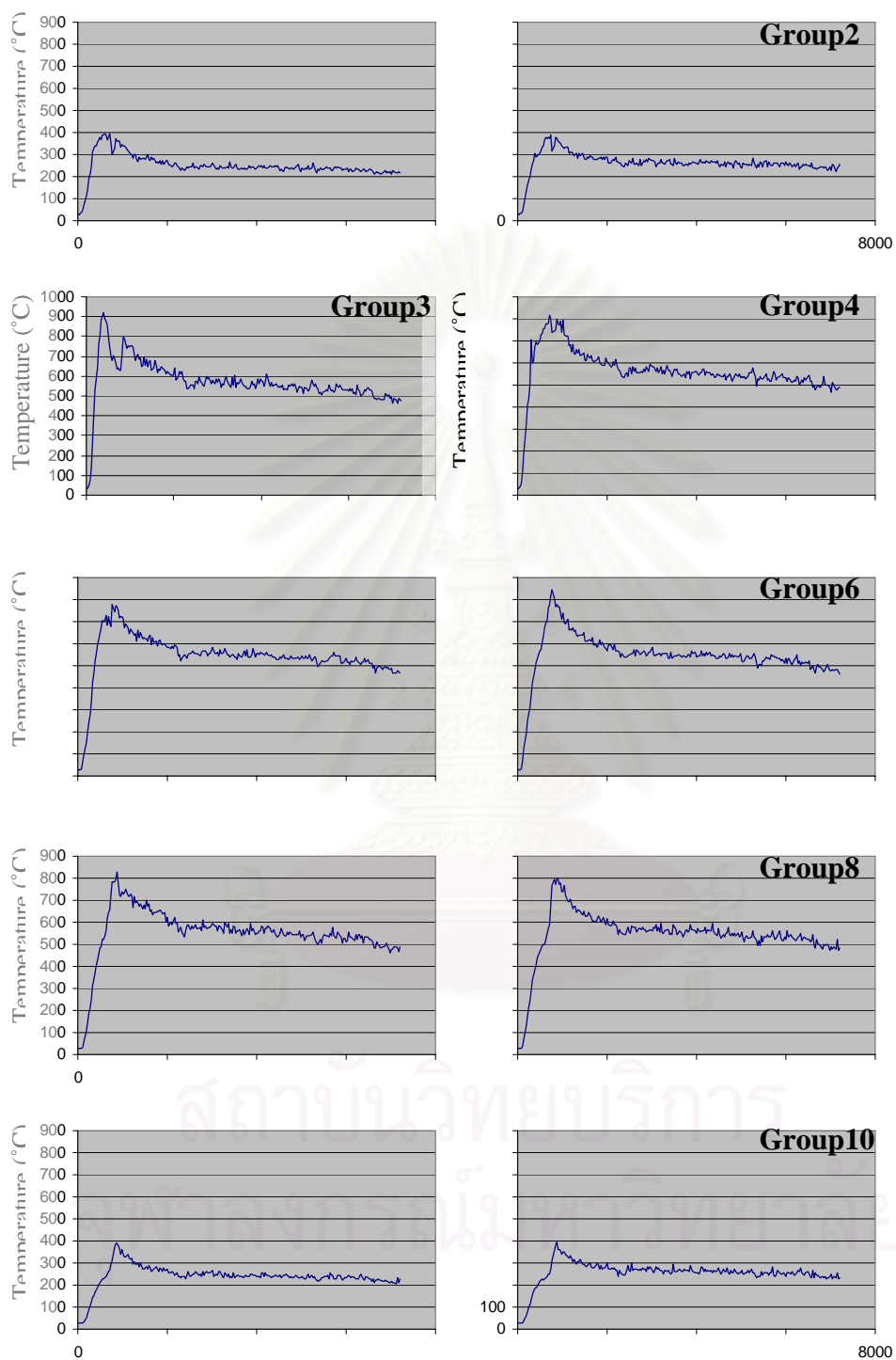


Figure 4.15 Temperature distribution for Case IV-AL

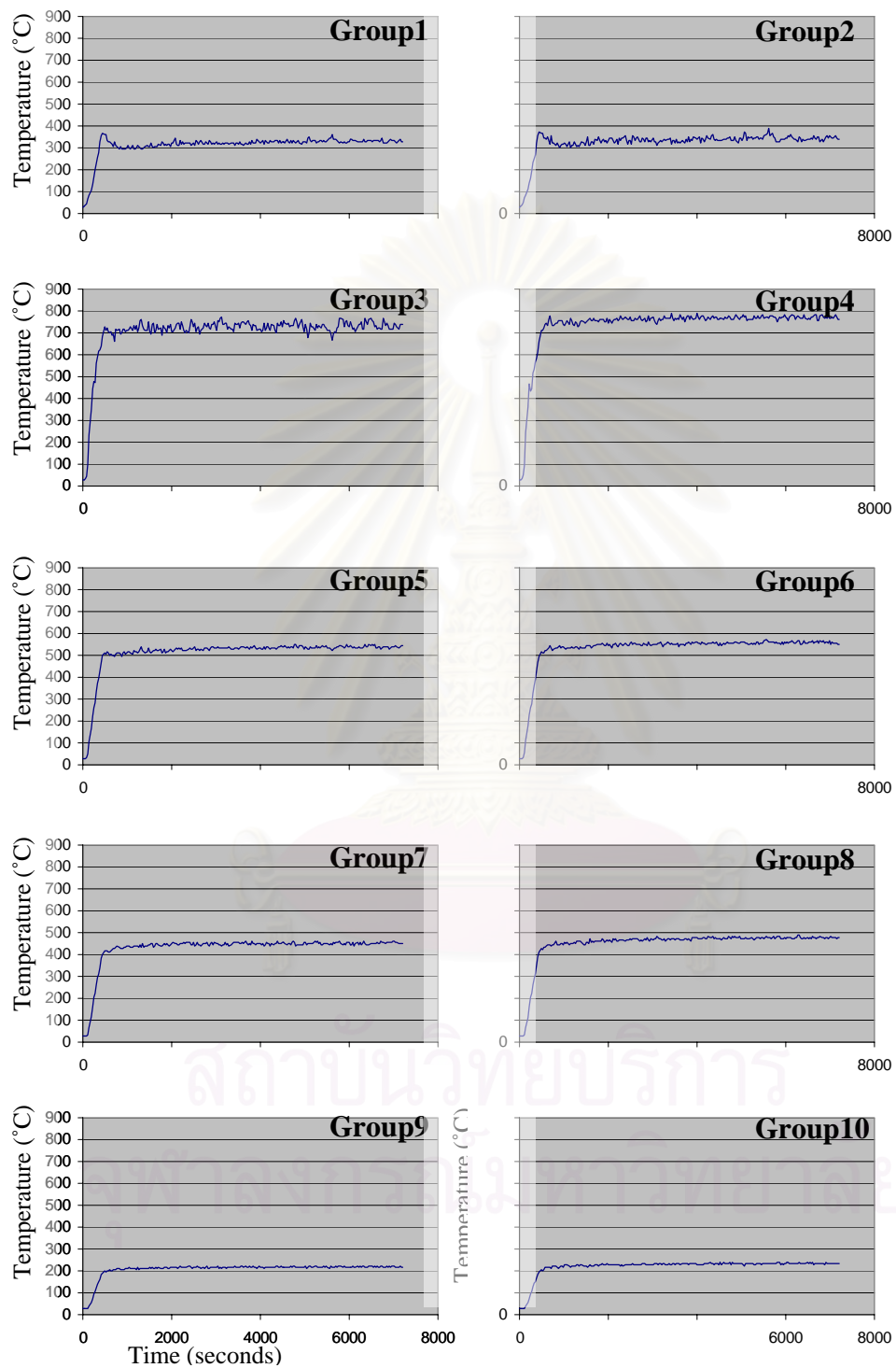


Figure 4.16 Temperature distribution for Case I-AH

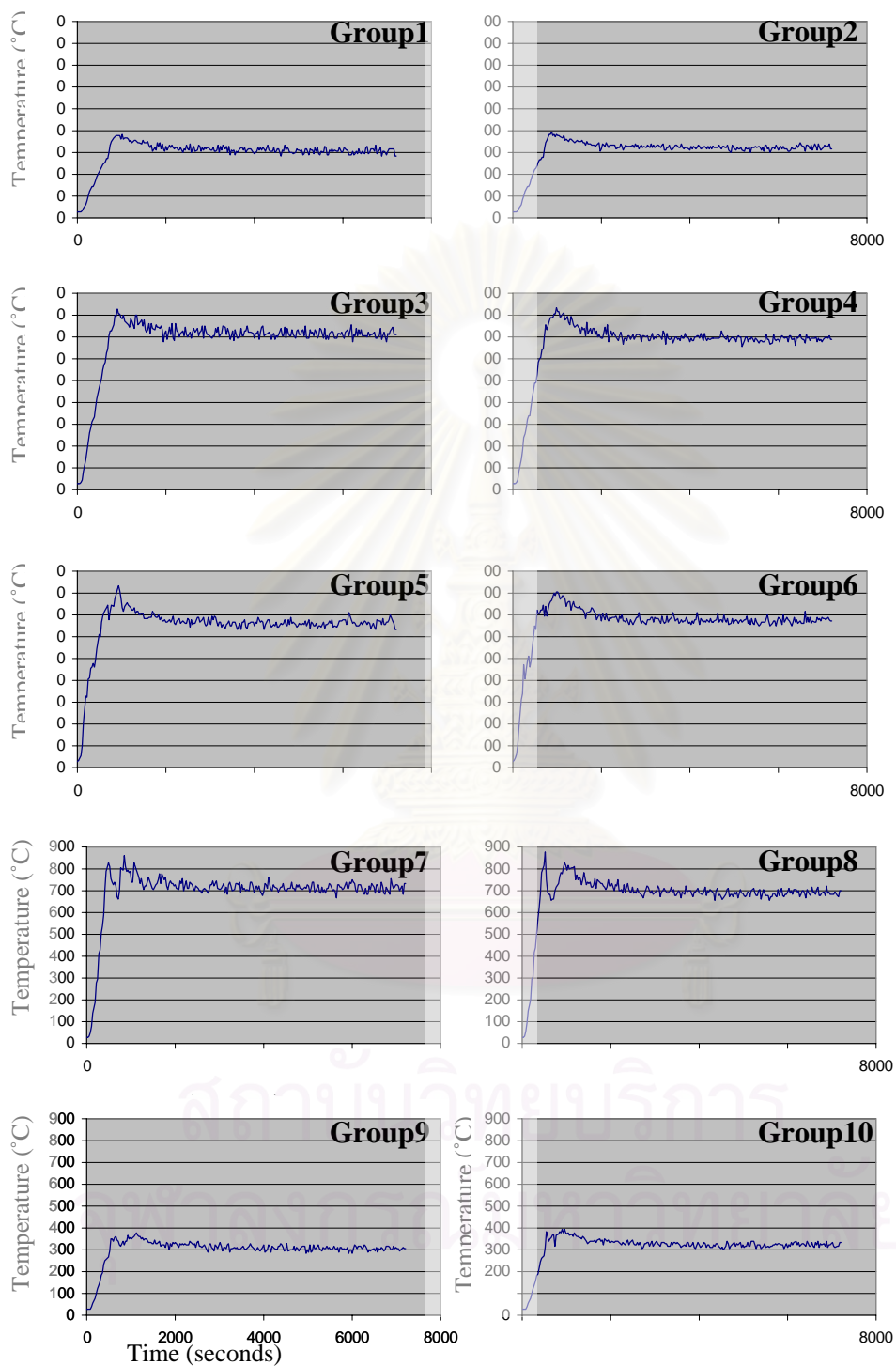


Figure 4.17 Temperature distribution for Case II-AH

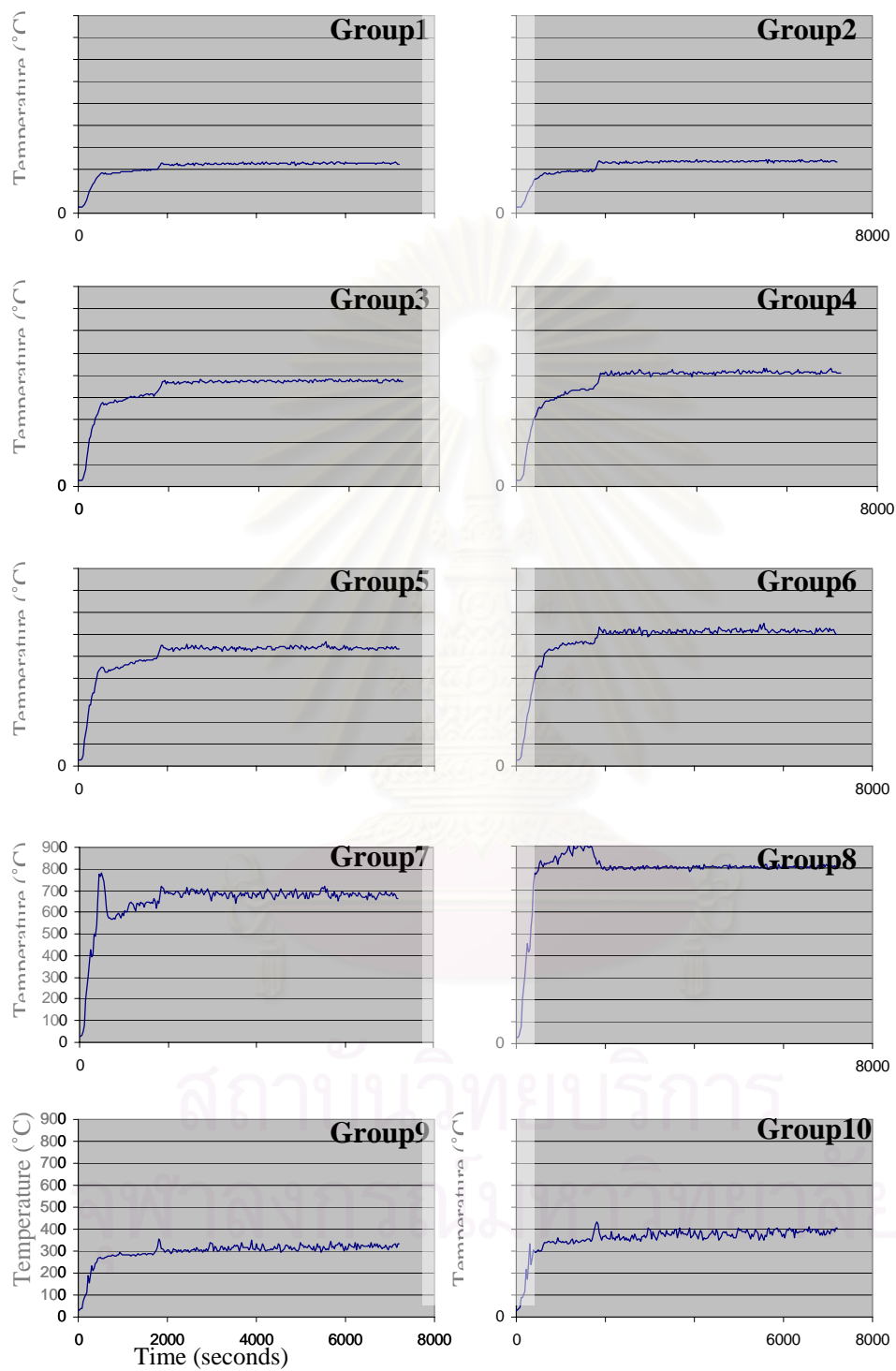


Figure 4.18 Temperature distribution for Case III-AH



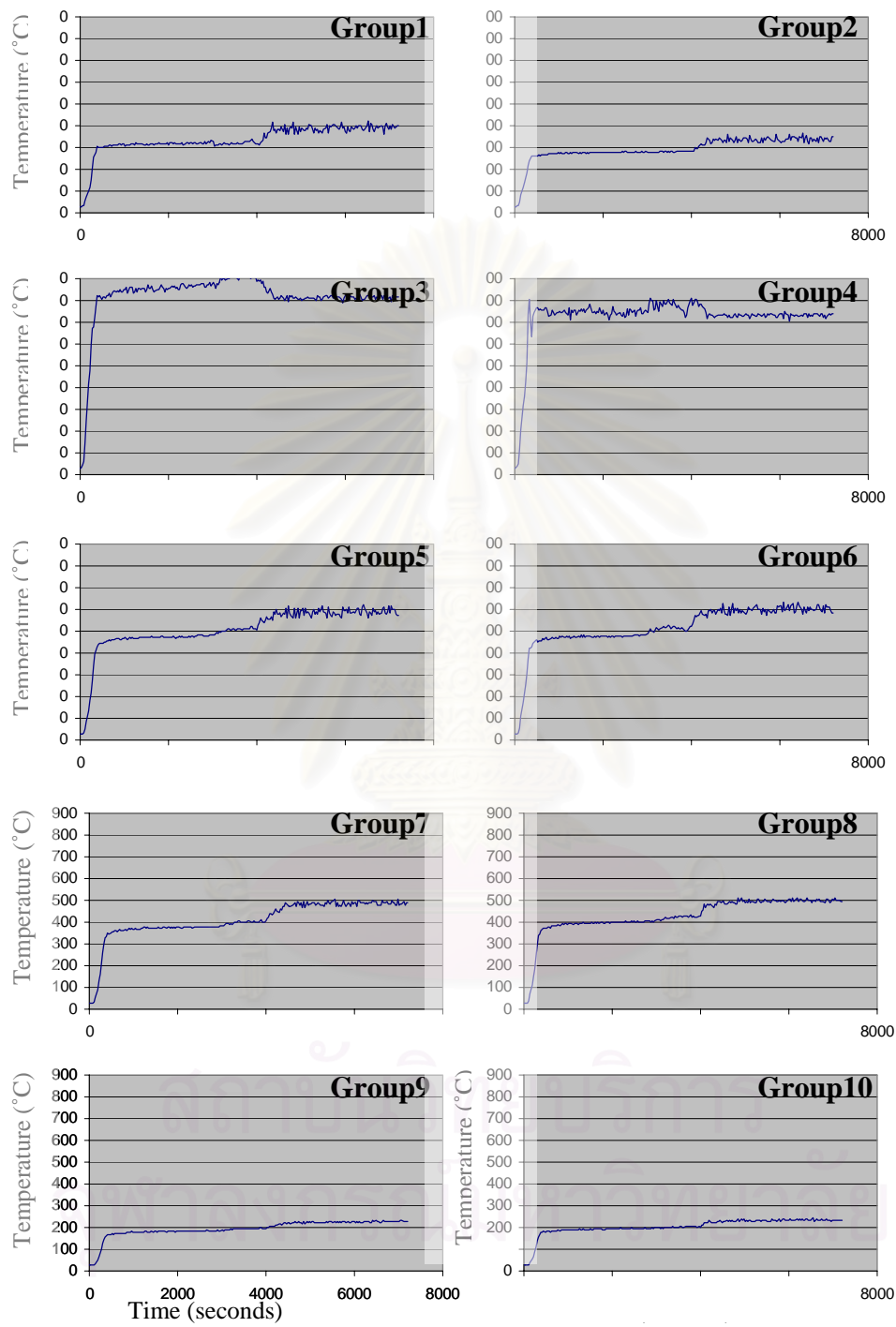


Figure 4.19 Temperature distribution for Case IV-AH

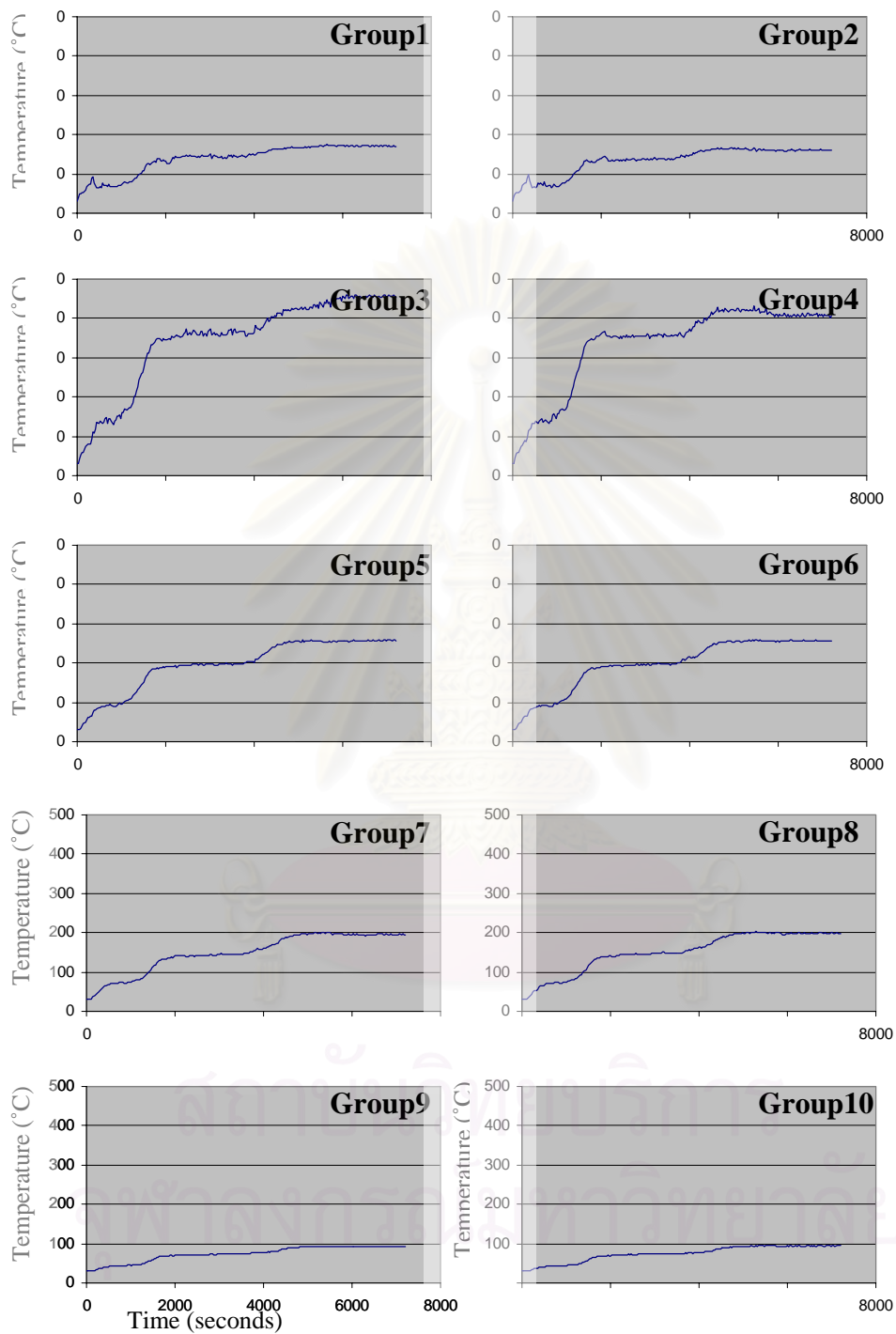


Figure 4.20 Temperature distribution for Case I-BL

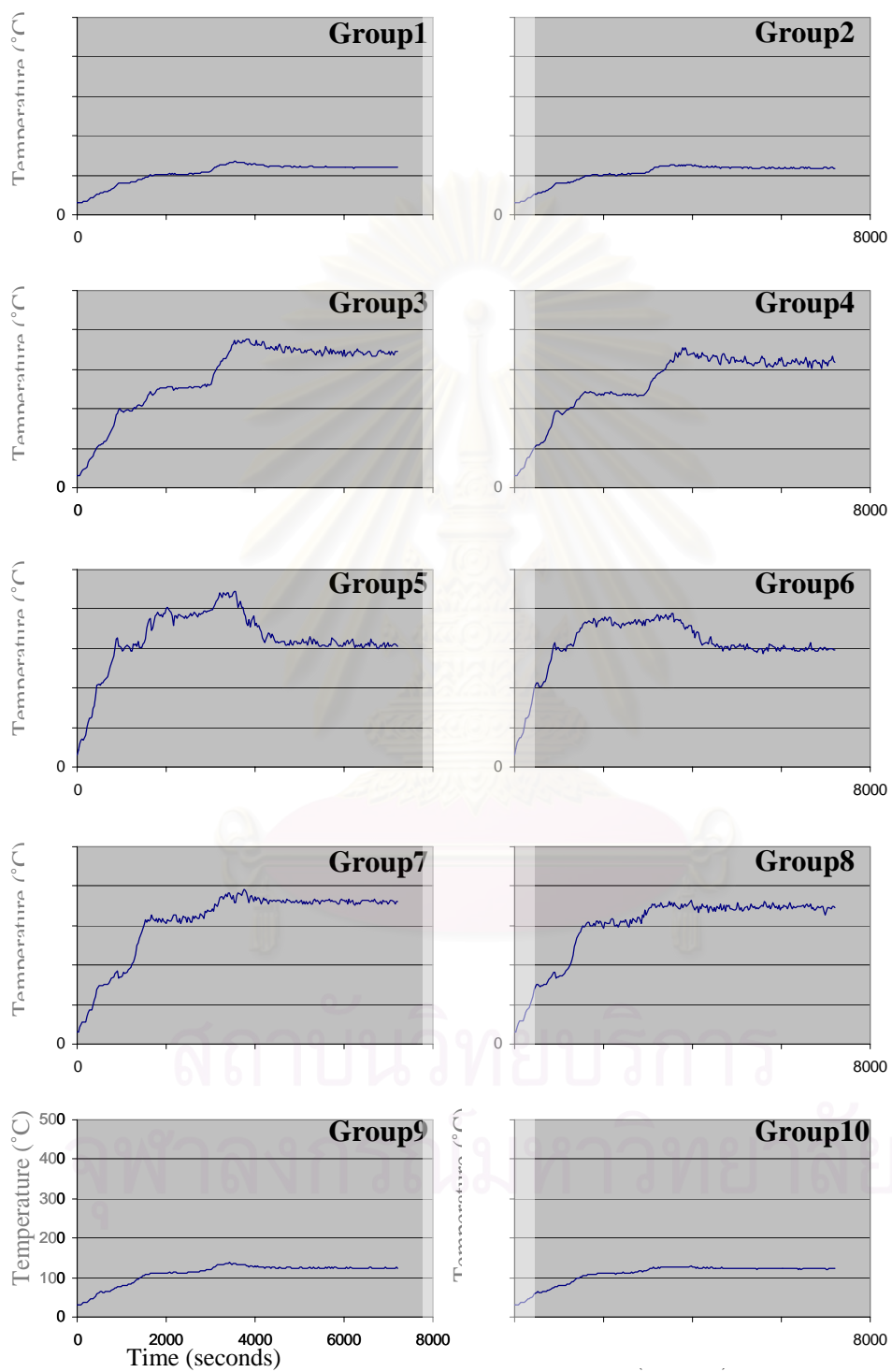


Figure 4.21 Temperature distribution for Case II-BL

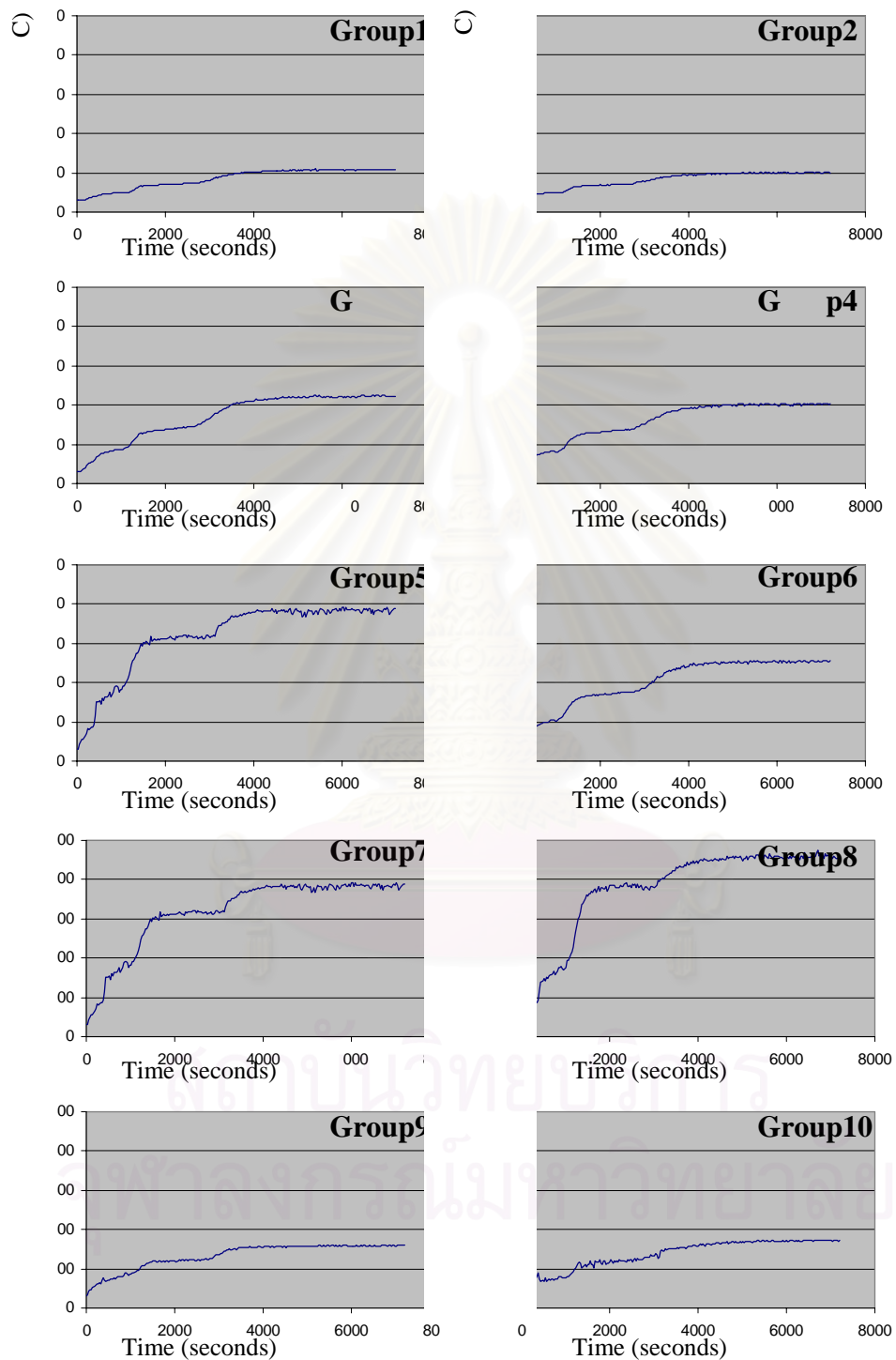


Figure 4.22 Temperature distribution for Case III-BL

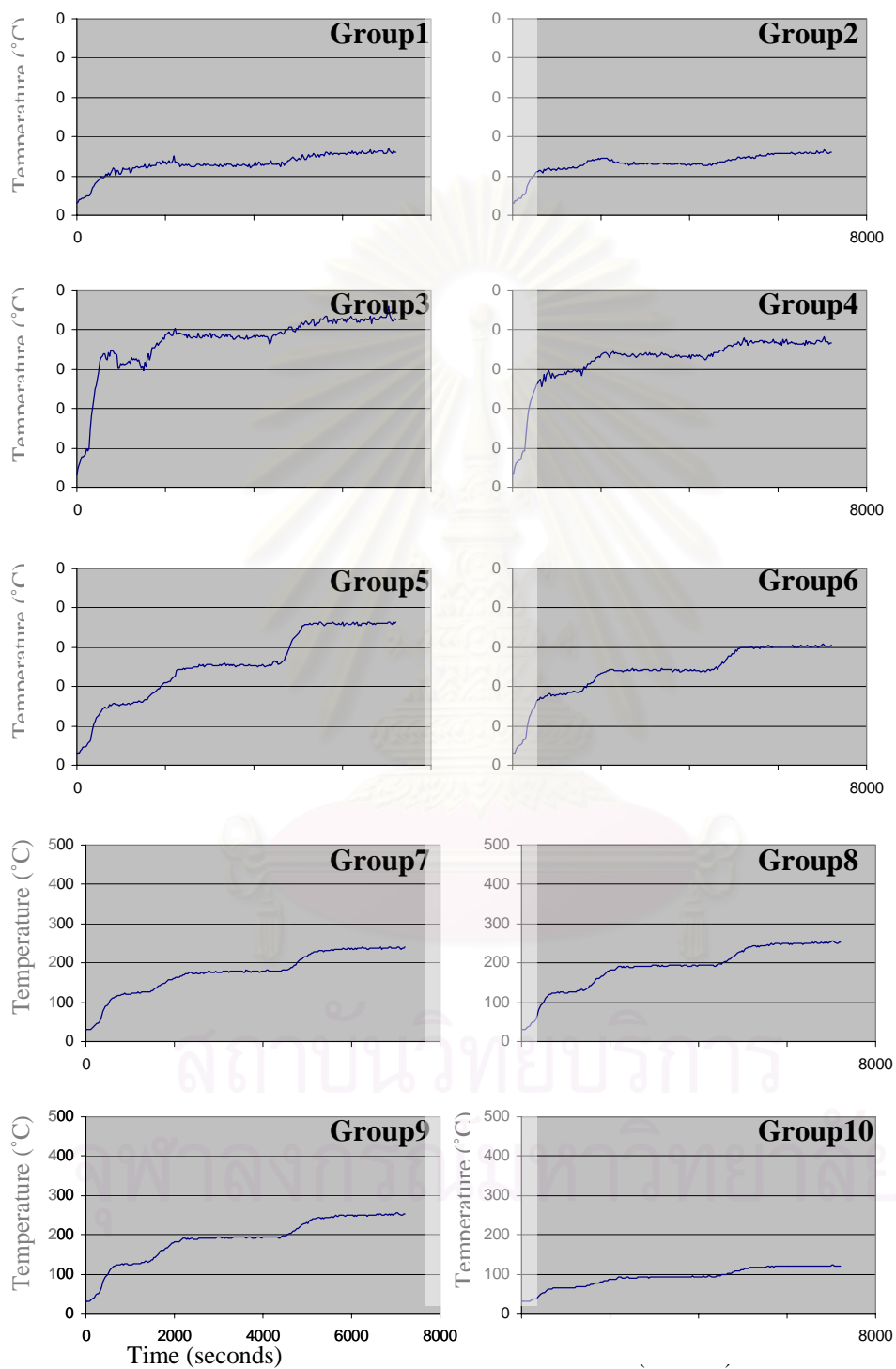


Figure 4.23 Temperature distribution for Case IV-BL

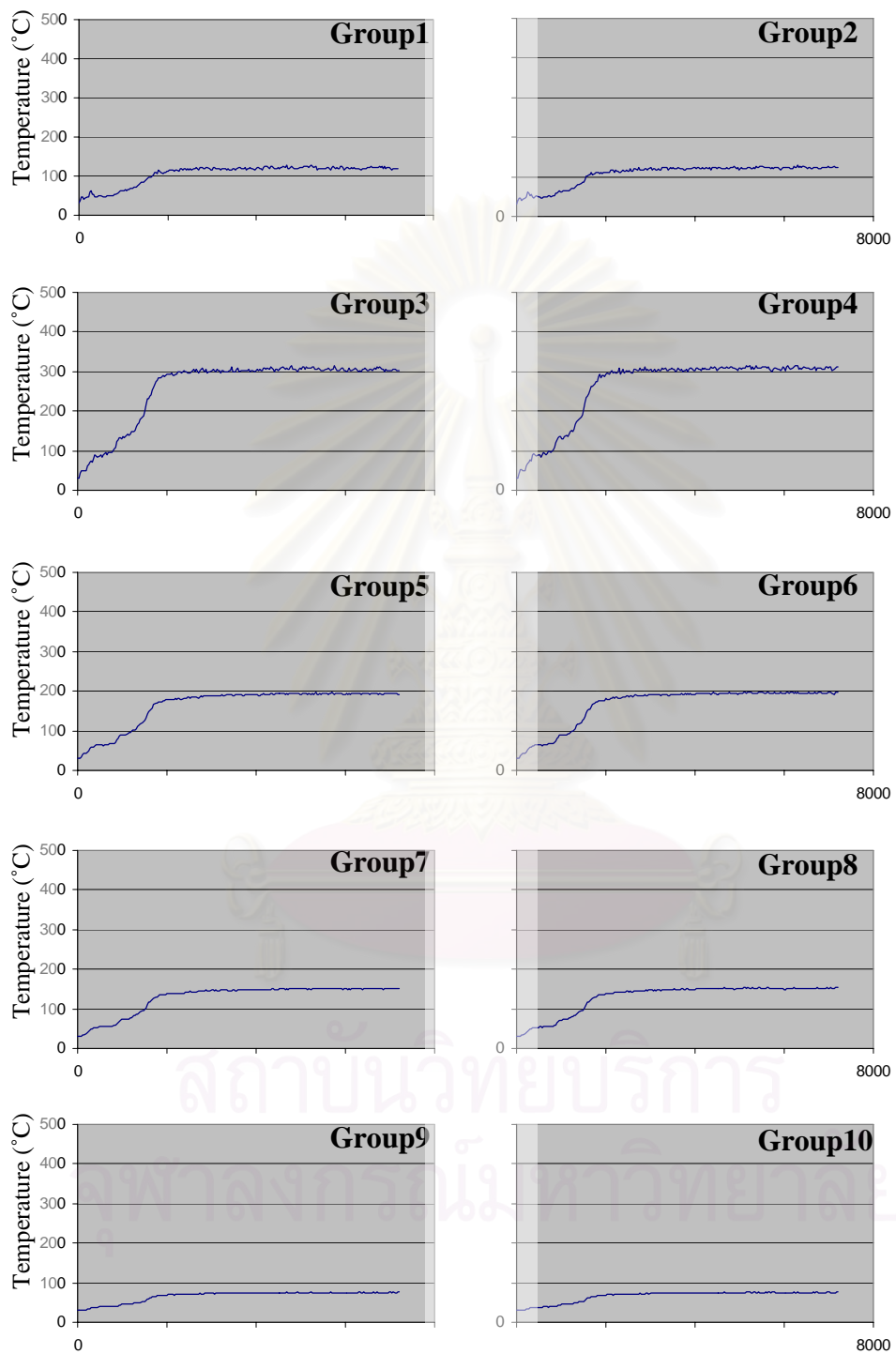


Figure 4.24 Temperature distribution for Case I-BH



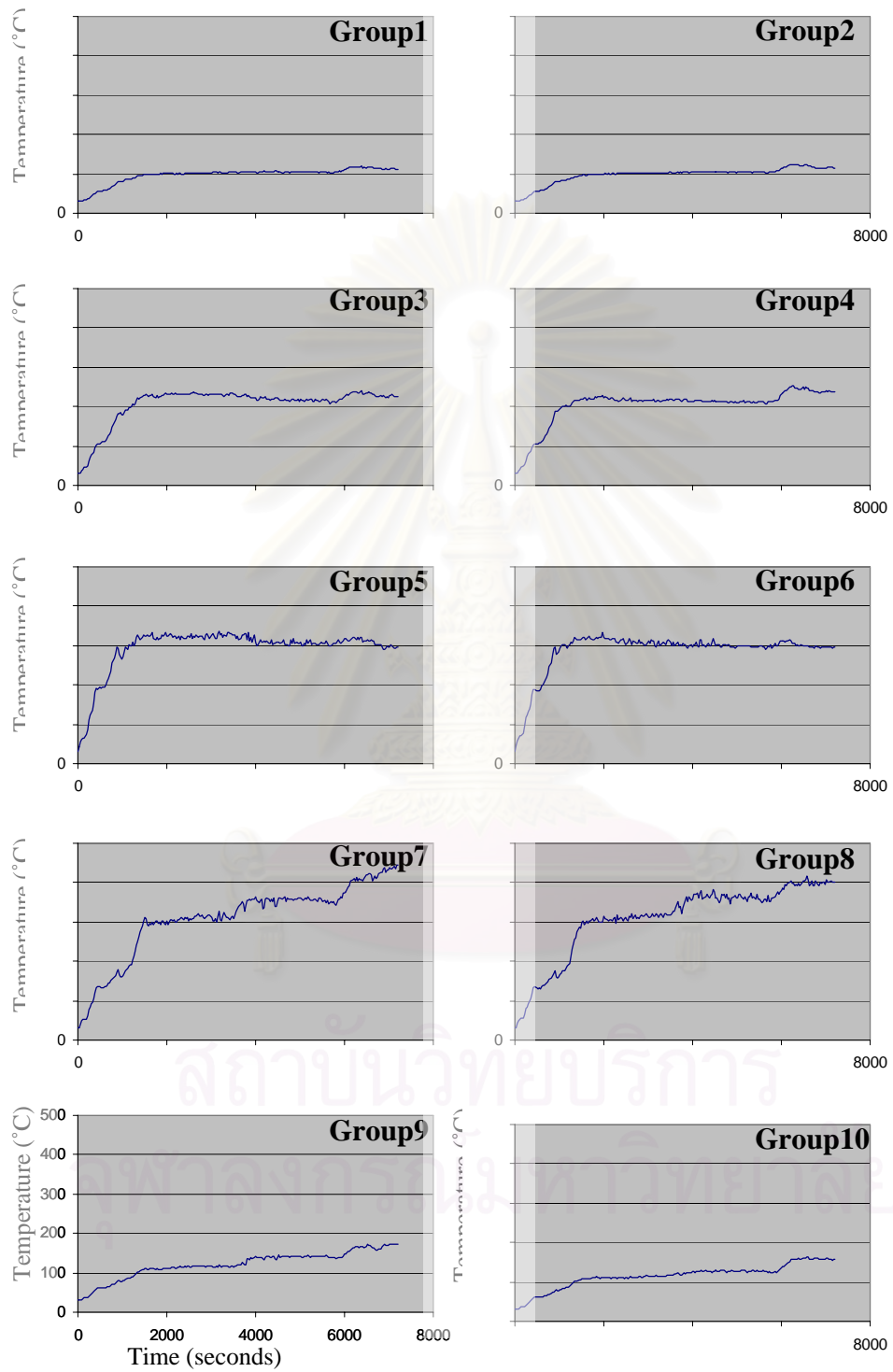


Figure 4.25 Temperature distribution for Case II-BH

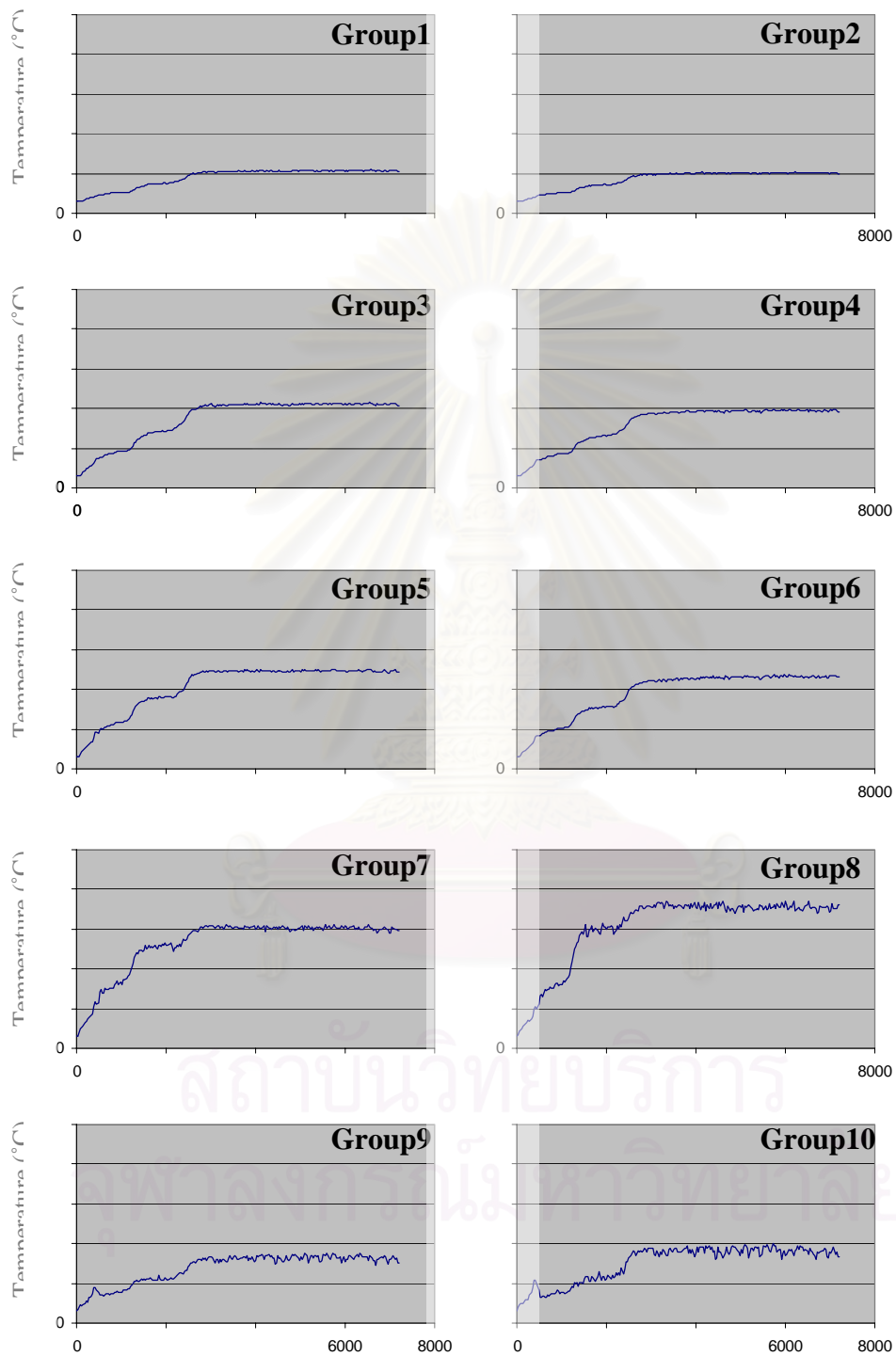


Figure 4.26 Temperature distribution for Case III-BH

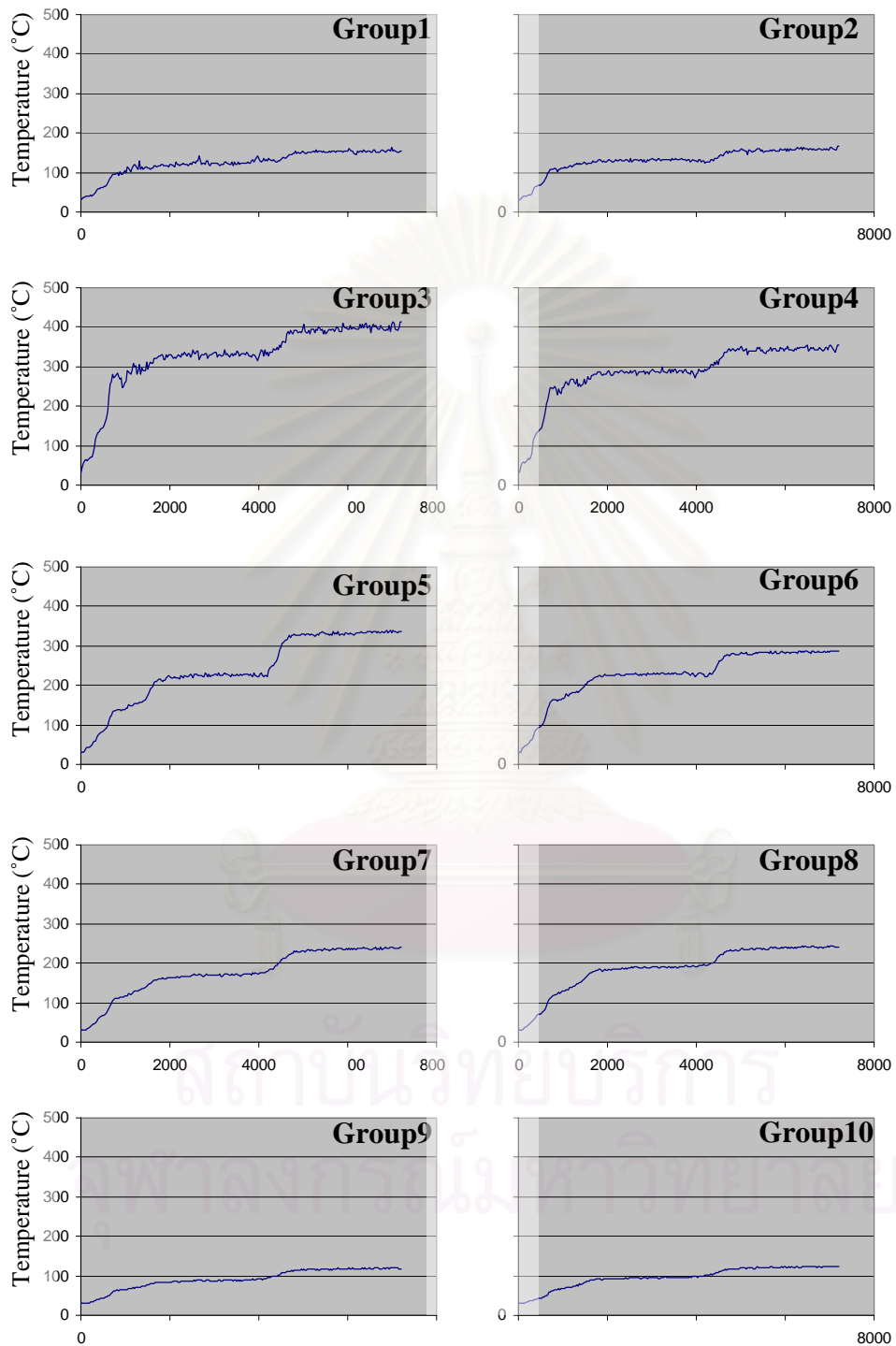


Figure 4.26 Temperature distribution for Case IV-BH

## 4.5 Structural Analysis Results

This section discusses the results obtained from analyzing the roof structure under the different fire scenarios investigated. The analysis adopts the nonlinear finite element method taking into consideration the decreasing mechanical properties and the expansion of steel with respect to the increasing temperature. The criteria for buckling and yielding listed in Tables 4.4 and 4.5 are employed to determine failure for each of the roof frame members. The coupled effects of compressive buckling and bending moments are investigated using Equations (2.26) and (2.27). To capture the various modes of structural failure for different fire scenarios, the maximum time in which the roof structure is subjected to fire is set to 120 minutes (7200 seconds).

Note that even though the roof structure consists of various components, i.e. the main roof frames, the longitudinal roof frames, bracing members and purlins, the structural system is deemed to fail only when the stresses within the top or bottom chords of the main roof frames reach their critical values.

### Case I-AHP

In this fire scenario, the ignition source is located between Span 1 and Span 2 of the main roof frames as illustrated in Figure 4.28. The structural analysis results are illustrated in Figures 4.29 and 4.30 in terms of the locations of failure of the roof members and the distribution of temperatures, stress and bending moments within the roof structure at 600, 800, 1000, 1200 and 1300 seconds. It is seen that upon the exposure to fire, the roof structure gradually elongates in both longitudinal and transverse directions. This elongation results in increasing compressive stresses in purlins which upon reaching their designated strength, fail in flexural-torsional buckling mode. Note that the sequence of failure not only depends on the different magnitudes of elongation, but also the reduced strength of the purlins due to the temperature variation. Because the purlins are restrained against elongation in the longitudinal direction at the supports of the roof structure, most of them are found buckling due to high compressive stresses.

The longitudinal and transverse elongations of the roof frames are partially resisted the bracing members which results in increasing tensile stresses. These tensile stresses are highly concentrated in the area at which the longitudinal elongations accumulate, i.e. Span 1 and Span 9. As a result, it is observed that the bracing member B13 in this area yields first at 800 seconds, followed by B12, B84 and B22, respectively.

Because longitudinal elongations accumulate at the edges of the roof structure, the main roof frames in these areas are laterally pushed. These pushing forces are counterbalanced by the in-plane elongation of the roof frames, reducing the compressive stresses in the top chords as observed in Figure 4.30. It is also observed from Figure 4.30 that the axial compression forces in the top chords of the main roof frames at Spans 2, 3 and 8 are relatively high compared with the other spans. This is due partly to the lateral pushing forces that are transferred to the main roof frames through the bracing members. For Span 2 and Span 3, the high temperature gradients between the upper and lower

frame members, which are located directly above the source of ignition (see Figure 4.29), induce higher tension and compression in the bottom and top chords, respectively. Note that upon yielding of the bracing members B12, B13 and B84, the compressive stresses in the top chords of Span 1 and Span 8 decrease, resulting in higher compression in Span 7.

The longitudinal and transverse thermal expansion of the overall roof structure is illustrated in Figure 4.31. The expansion of the roof structure in the longitudinal direction causes the main roof frames to sway horizontally with respect to their supports. This results in additional torsion, shear and moments due to the second-order ( $P-\Delta$ ) effect. The situation can be illustrated in Figure 4.32. In particular, the combination of the increasing compressive stresses, the deteriorating mechanical properties and the  $P-\Delta$  effects causes member 16 (top chord) of Span 3 to fail in flexural buckling as shown in Figure 4.29 at 1300 seconds. The failure of this member essentially indicates failure of the structural system.

The maximum thermal expansion of the roof structure is approximately 10 cm in the global  $X$  and  $Y$  directions. This expansion leads to an increase in the support reactions as illustrated in Figure 4.33. Note that the reactions are significantly increased from the normal temperature condition.

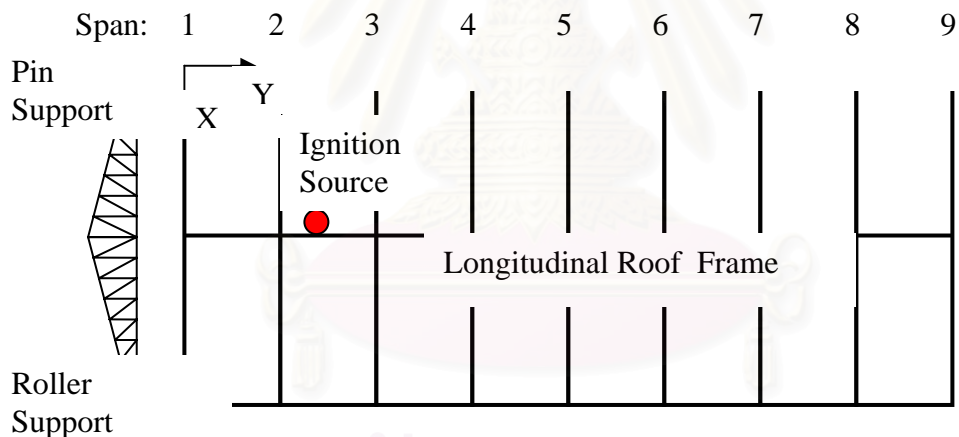


Figure 4.28 Location of the ignition source for Case I-AHP



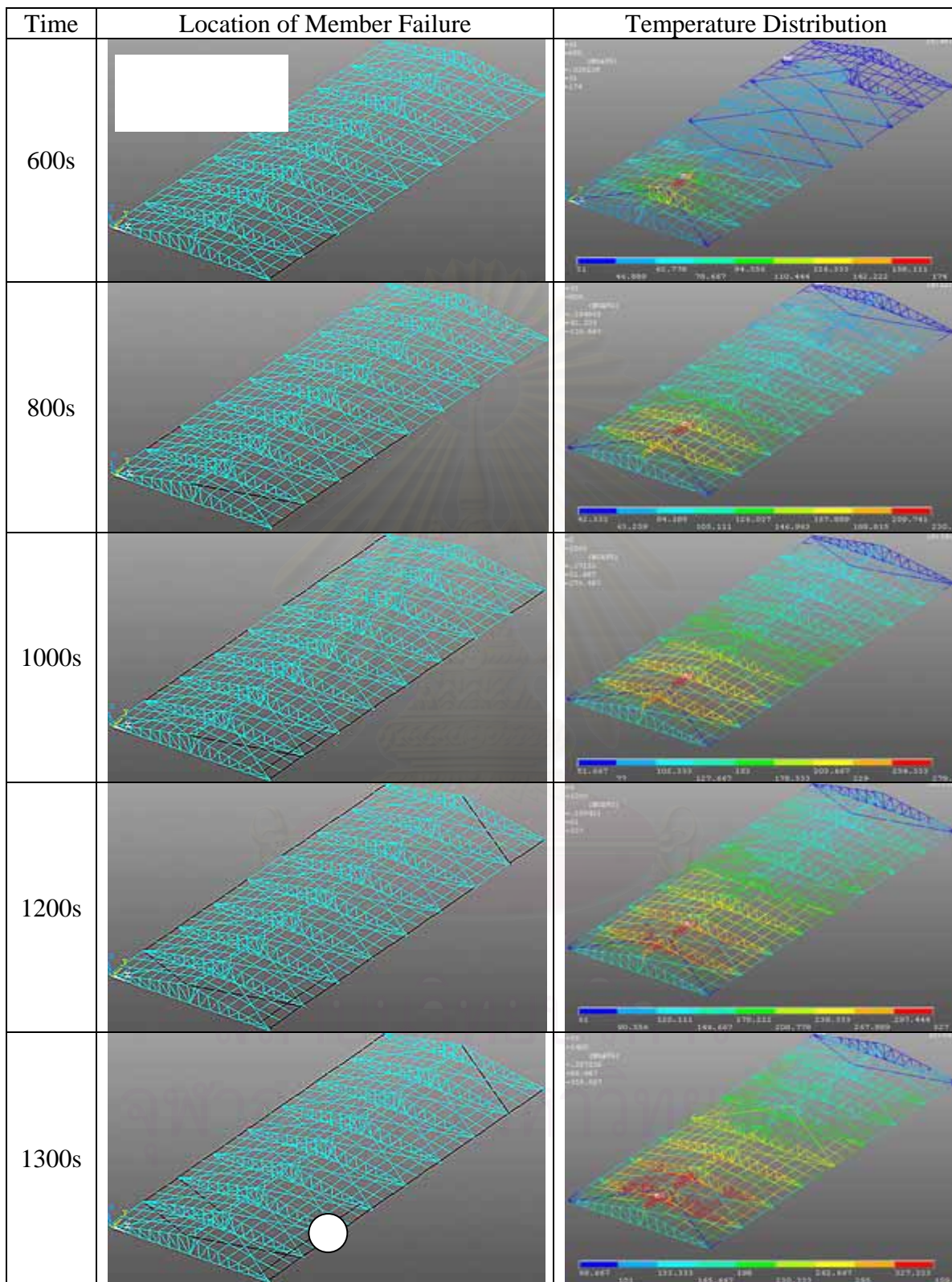


Figure 4.29 Location of member failure and temperature distribution at different time steps for Case I-AHP



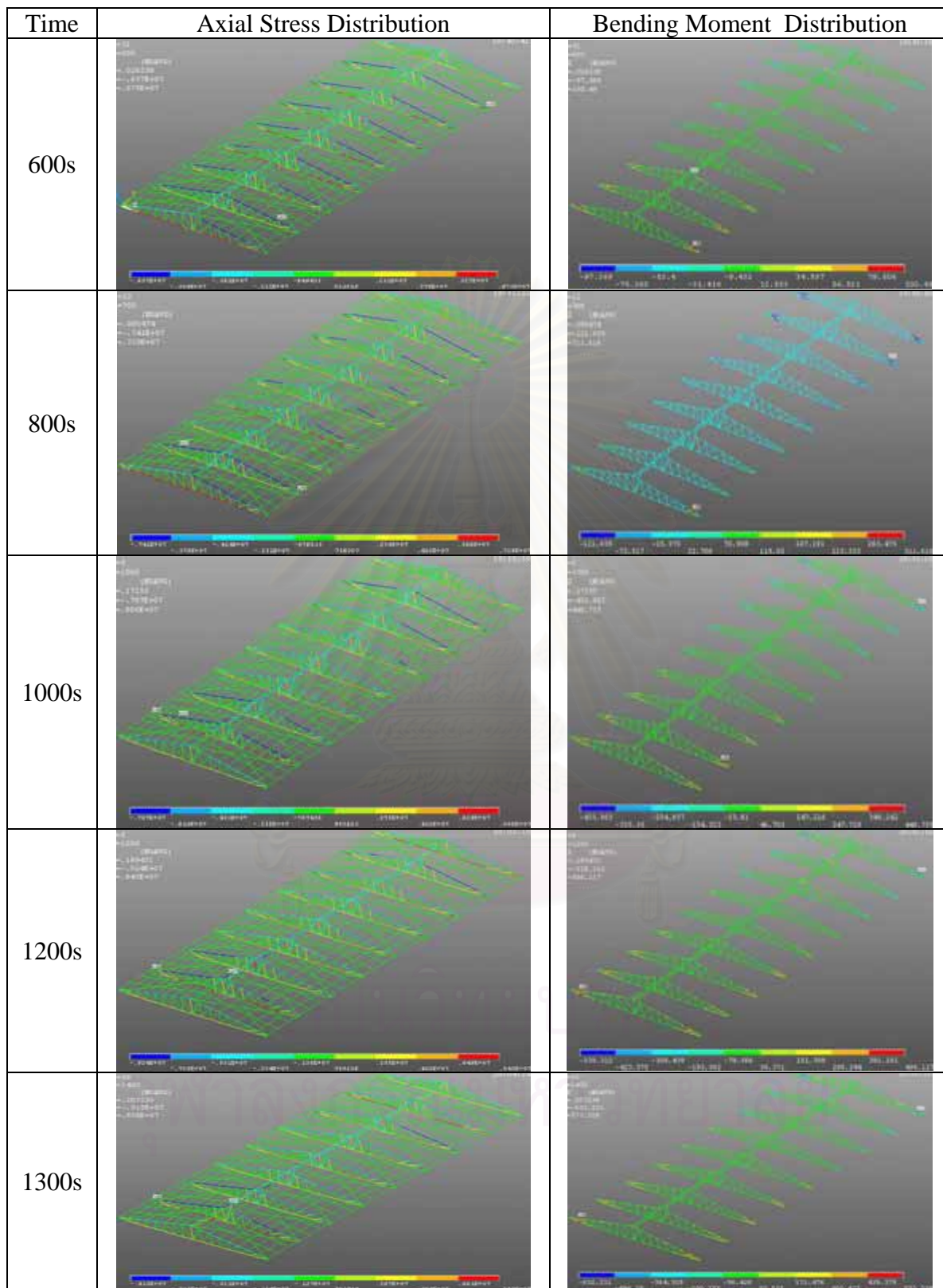


Figure 4.30 Distribution of stresses and bending moments at different time steps for Case I-AHP

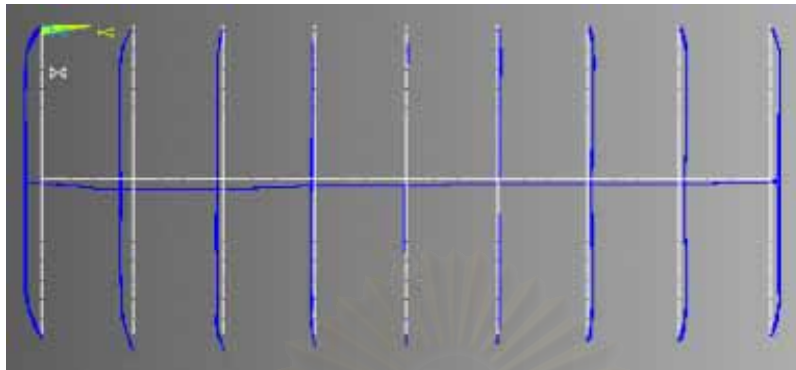


Figure 4.31 Longitudinal and transverse thermal expansion of the roof structure for Case I-AHP at 1400 seconds

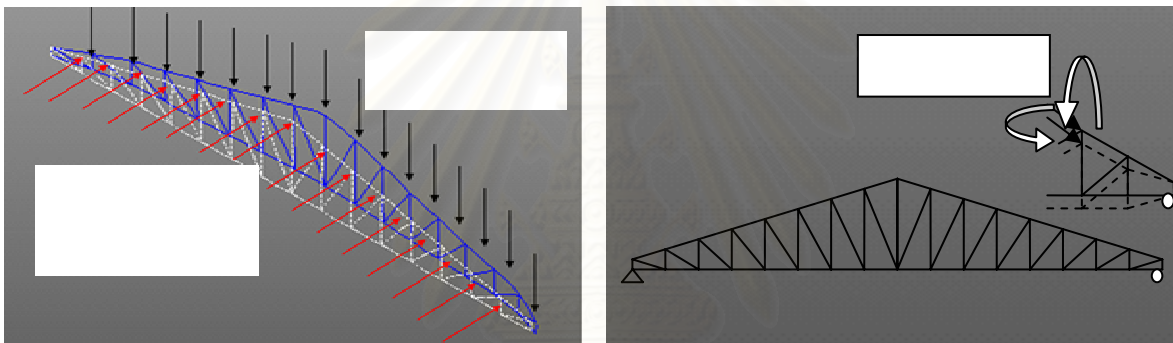


Figure 4.32 P- $\Delta$  effects for the main roof frame

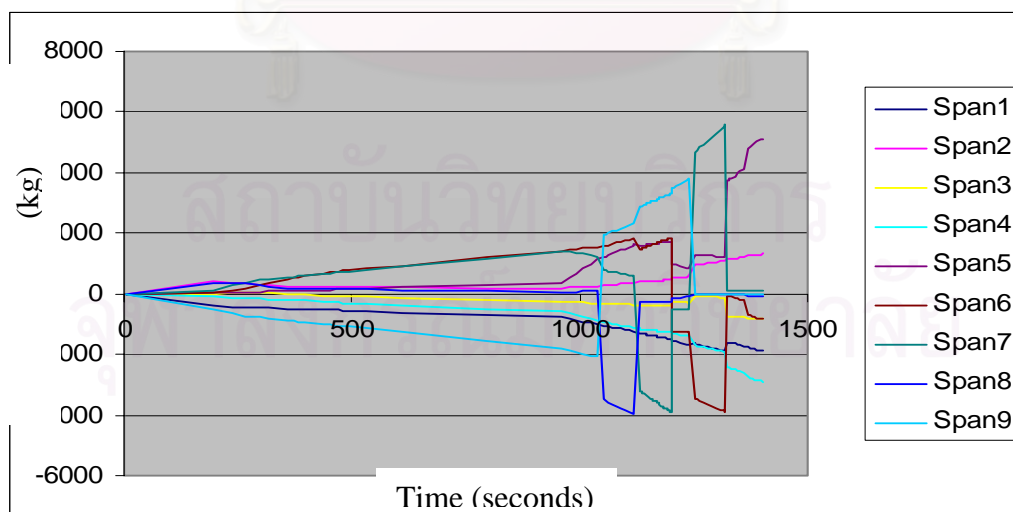


Figure 4.33 Variation of reaction in X-direction at pin supports of the main roof frames with respect to temperature for Case I-AHP

Similarly results are observed for Case I-ALP and Case I-BLU in which the sequence of member failure and the temperature distribution at structural failure are shown in Figures 4.34 and 4.35.

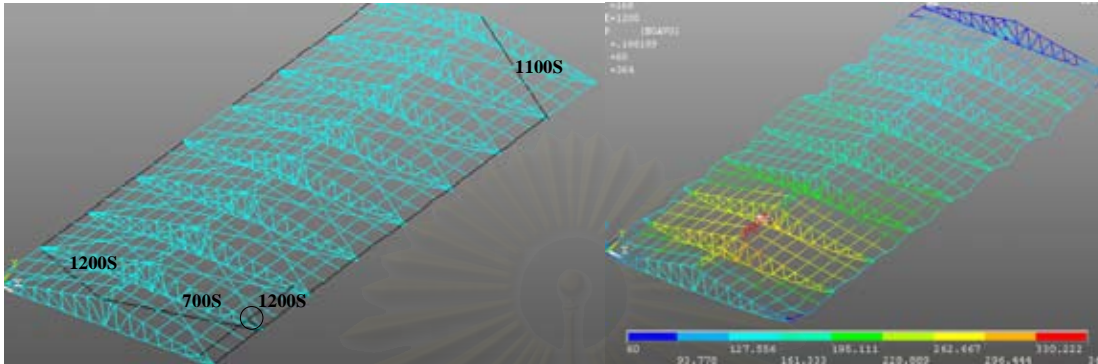


Figure 4.34 Sequence of failure for the structural members and temperature distribution of the structure at failure for Case I-ALP

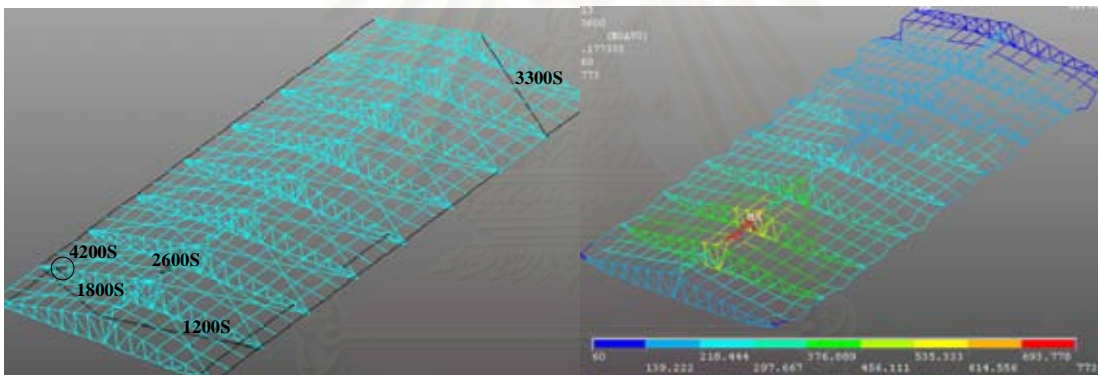


Figure 4.35 Sequence of failure for the structural members and temperature distribution of the structure at failure for Case I-BLU

### Case I-AHU

The sequence of failure for the roof frame members and the temperature distribution at different time steps are summarized in Figure 4.36. It is seen that large thermal expansion occurs around Span 1. This expansion, coupled with the P- $\Delta$  effects causes the bracing member B13 to fail at 230 seconds. Meanwhile because of the rapidly increasing temperature, the mechanical properties of the steel roof frames are expected to drop significantly. In particular, the longitudinal roof frame located between Span 2 and Span 3 reaches the temperature of 680 °C at 270 seconds, resulting in flexural buckling of the frame member. Likewise, member 7 of Span 2 fails at 400 seconds due to flexural buckling when its temperature reaches 650 °C. Case I-ALU yields the same sort of results, with the sequence of failure and the temperature distribution at structural failure shown in Figure 4.37



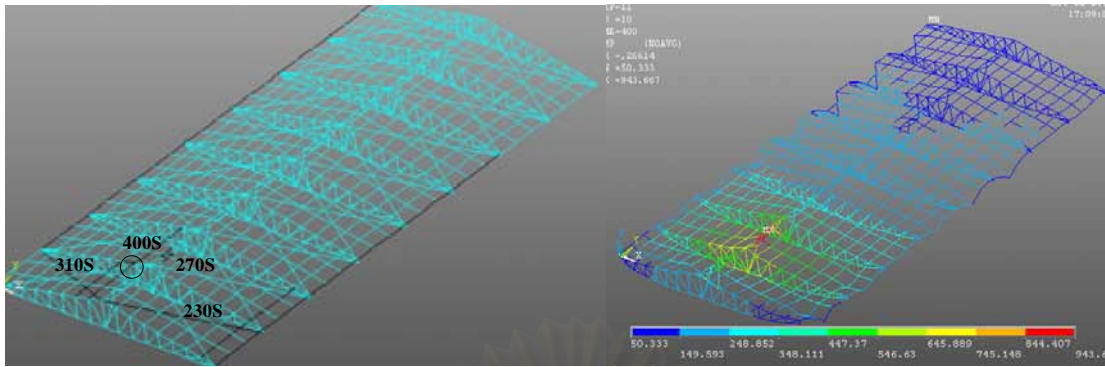


Figure 4.36 Sequence of failure for the structural members and temperature distribution of the structure at failure for Case I-AHU

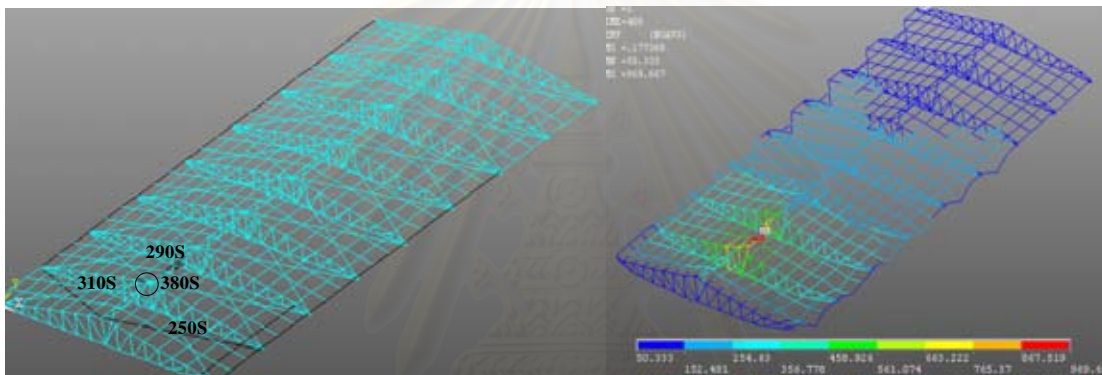


Figure 4.37 Sequence of failure for the structural members and temperature distribution of the structure at failure for Case I-ALU

#### Cases I-BHP, I-BHU and I-BLP

The top and bottom chords of the main roof frames do not fail after 7200 seconds burning period and thus the structure is not deemed to fail. The failure time of the structure for these cases is reported as 7200 seconds. The sequence of the failure for the structural members and the temperature distribution of the structure for Cases I-BHP, I-BHU and I-BLP are shown in Figures 4.38-4.40, respectively.

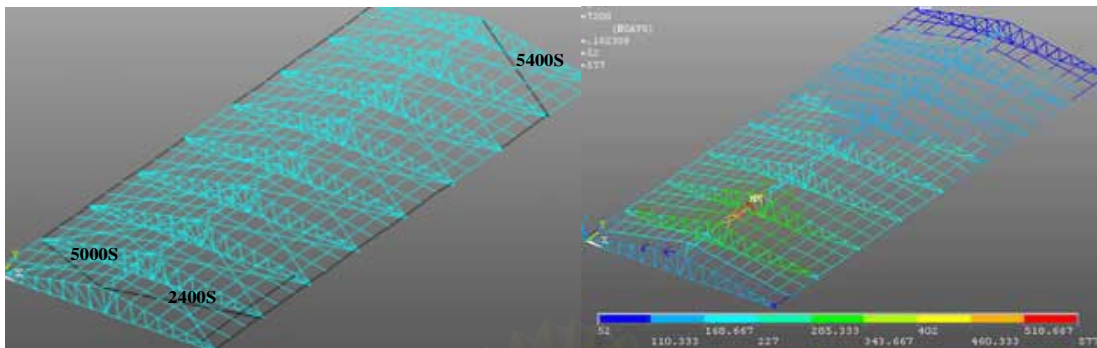


Figure 4.38 The sequence of the failure for the structural members and the temperature distribution of the structure at 7200 seconds for Case I-BHP

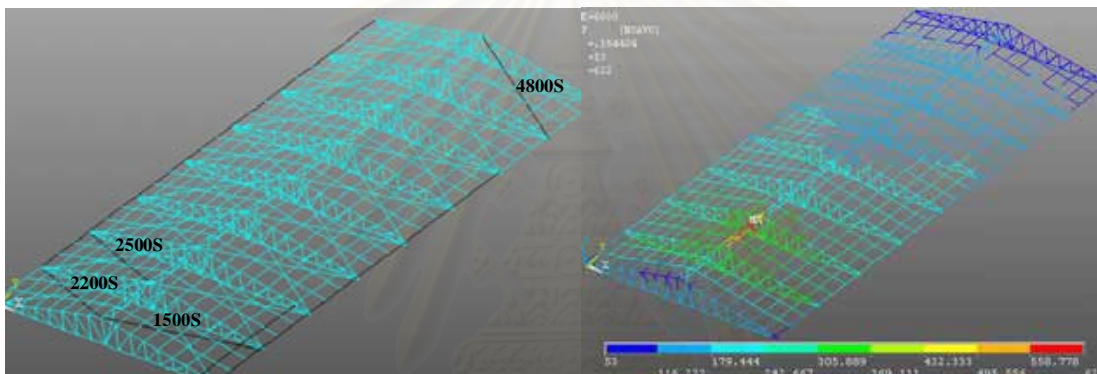


Figure 4.39 The sequence of the failure for the structural members and the temperature distribution of the structure at 7200 seconds for Case I-BHU

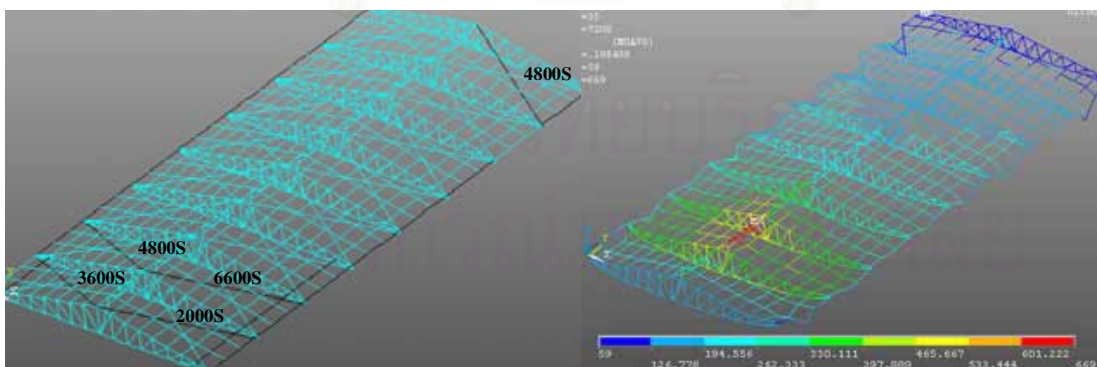


Figure 4.40 The sequence of the failure for the structural members and the temperature distribution of the structure at 7200 seconds for Case I-BLP

### Case II-AHP

In this fire scenario, the ignition source is located at the middle of the warehouse as illustrated in Figure 4.41. The structural analysis results are illustrated in Figures 4.42 and 4.43 in terms of the locations of failure of the roof members and the distribution of temperatures, stresses and bending moments within the roof structure at 700, 800, 950 and 1150 seconds. The thermal expansions of the main roof frames are similar to Case I-AHP as observed from the relatively low compressive stresses for the main roof frames at the middle of the warehouse. Again, it is found that the bracing members B13 and B84 first fail due to thermal expansion. Moreover, the  $P-\Delta$  effects at the supports of the main roof frame cause member 16 of Span 1 to fail at 1150 seconds.

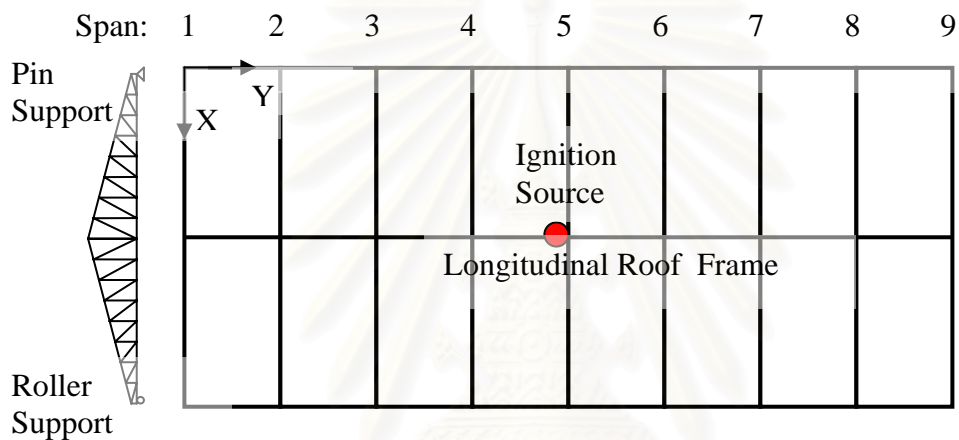


Figure 4.41 Location of the ignition source for Case II-AHP



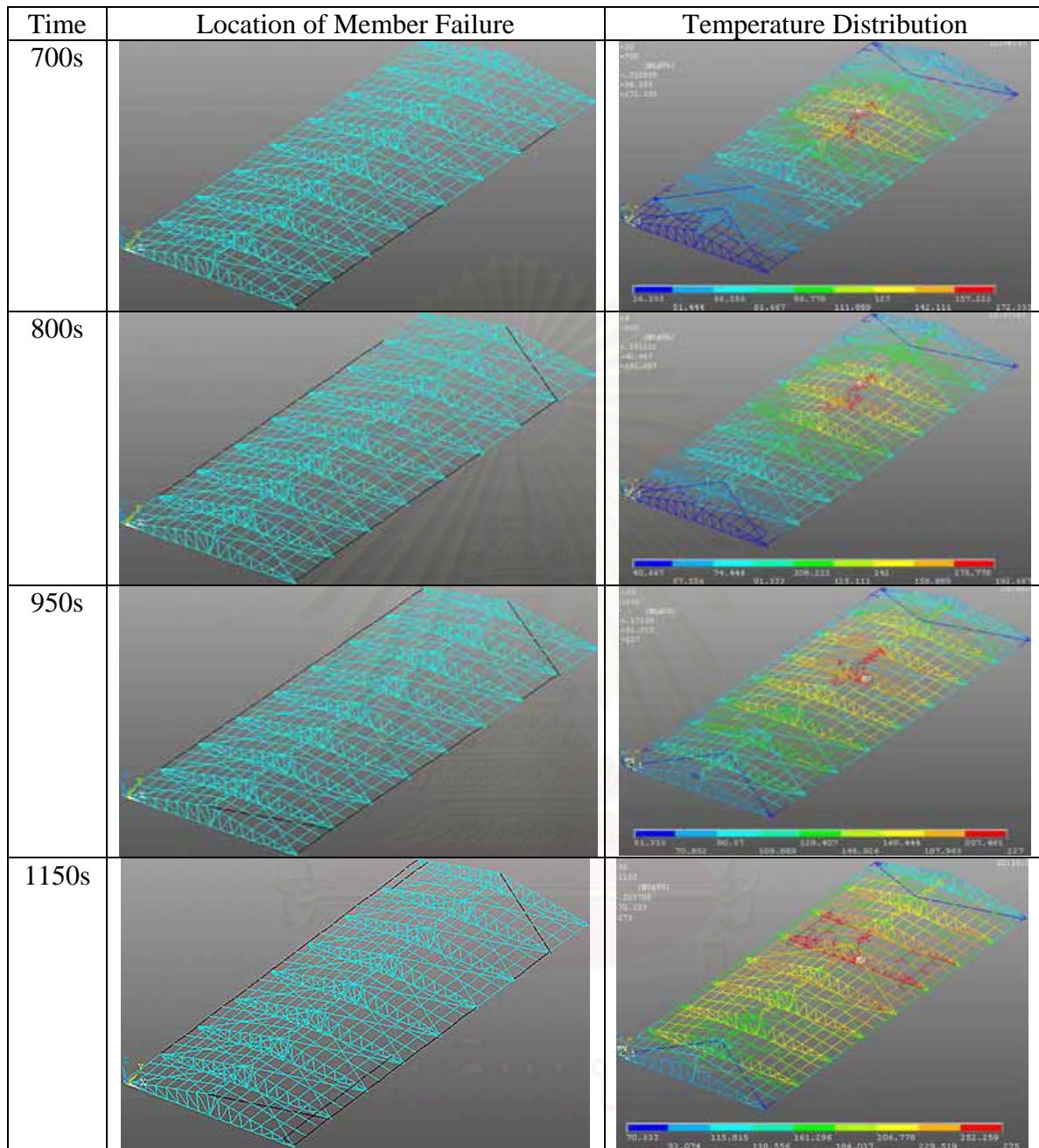


Figure 4.42 Location of member failure and temperature distribution at different time steps for Case II-AHP

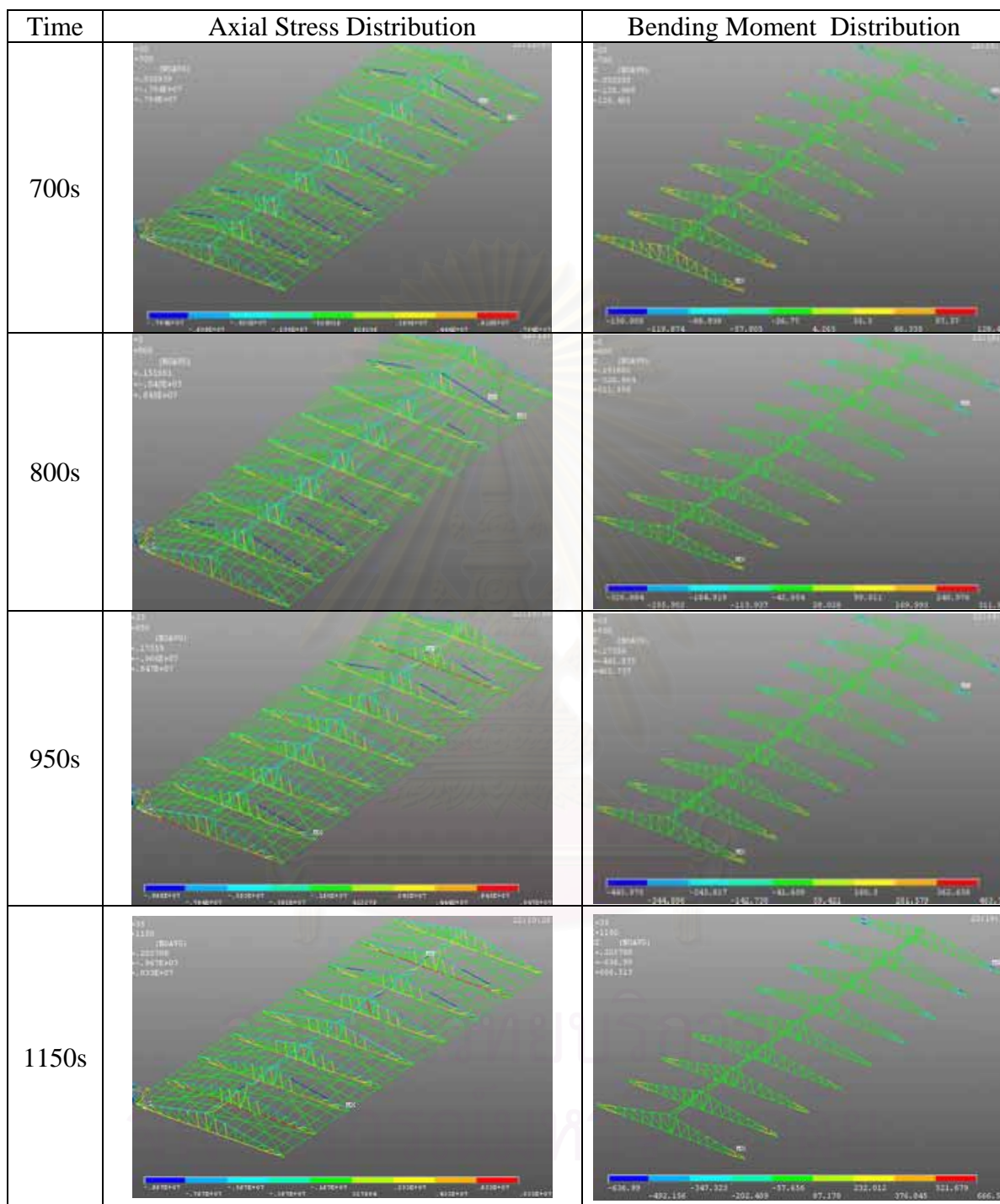


Figure 4.43 Distribution of axial stresses and bending moments at different time steps for Case II-AHP

Similarly results are observed for Cases II-ALP, II-AHU, II-BHU and II-BLU in which the sequence of member failure and the temperature distribution at structural failure are shown in Figures 4.44 to 4.47

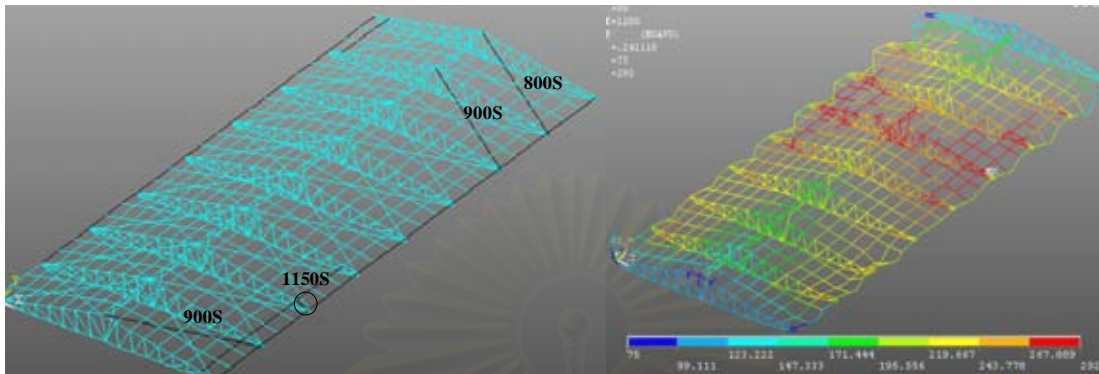


Figure 4.44 Sequence of failure for the structural members and temperature distribution of the structure at failure for Case II-ALP

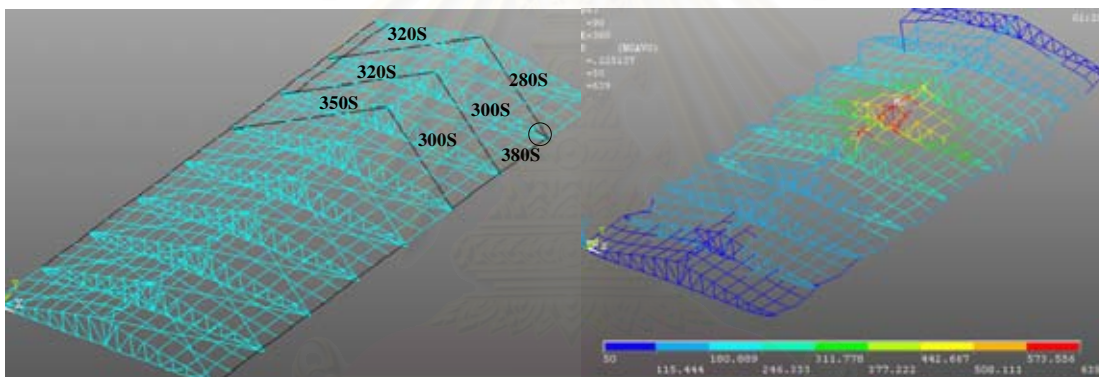


Figure 4.45 Sequence of failure for the structural members and temperature distribution of the structure at failure for Case II-AHU

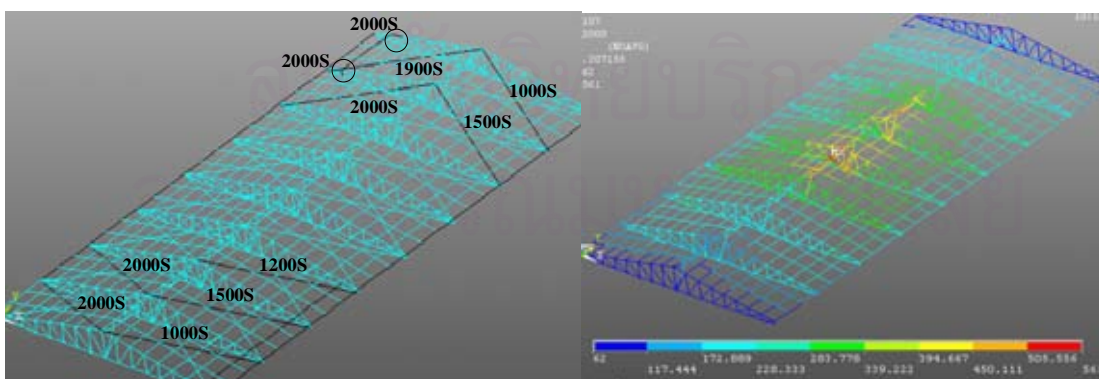


Figure 4.46 Sequence of failure for the structural members and temperature distribution of the structure at failure for Case II-BHU



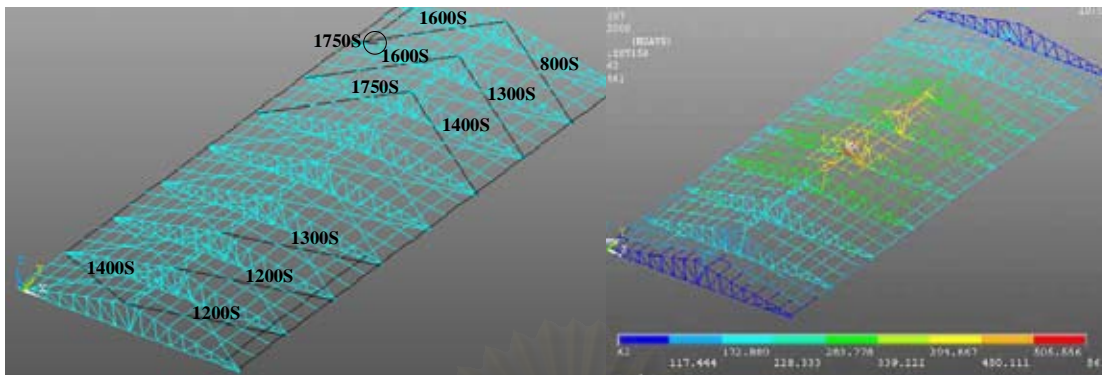


Figure 4.47 Sequence of failure for the structural members and temperature distribution of the structure at failure for Case II- BLU

### Case II-ALU

The sequence of failure for the roof frame members and the temperature distribution at different time steps are summarized in Figure 4.48. This expansion, coupled with the P- $\Delta$  effects causes the bracing member B84 to fail at 260 seconds. Meanwhile because of the rapidly increasing temperature, the mechanical properties of the steel roof frames are expected to drop significantly. In particular, the longitudinal roof frame located between Span 6 and Span 7 reaches the temperature of 600 °C at 270 seconds, resulting in flexural buckling of the frame member. Likewise, member 9 of Span 6 fails at 330 seconds due to flexural buckling when its temperature reaches 610 °C. Case II-ALU yields the same sort of results, with the sequence of failure and the temperature distribution at structural failure shown in Figure 4.48.

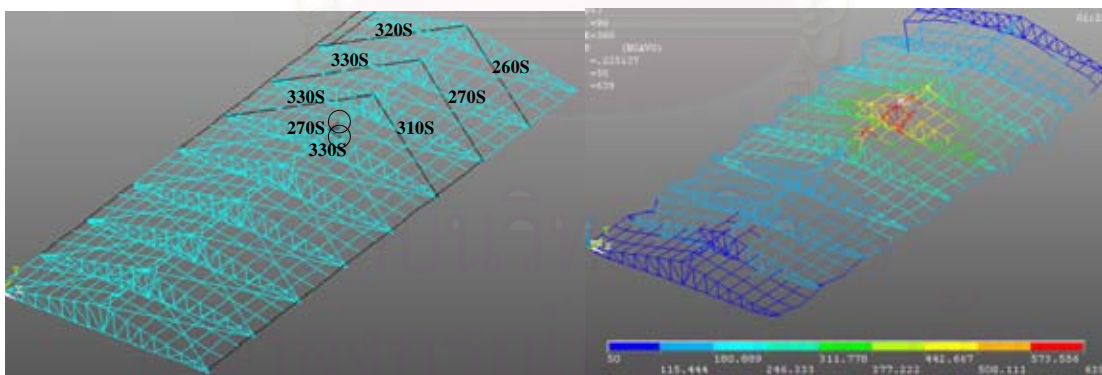


Figure 4.48 Sequence of failure for the structural members and temperature distribution of the structure at failure for Case II-ALU

### Cases II-BHP and II-BLP

The top and bottom chords of the main roof frames do not fail after 7200 seconds burning period and thus the structure is not deemed to fail. The failure time of the structure for these cases is reported as 7200 seconds. The sequence of the failure for the structural members and the temperature distribution of the structure for Cases II-BHP and Case II-BLP are shown in Figures 4.49 and 4.50, respectively.

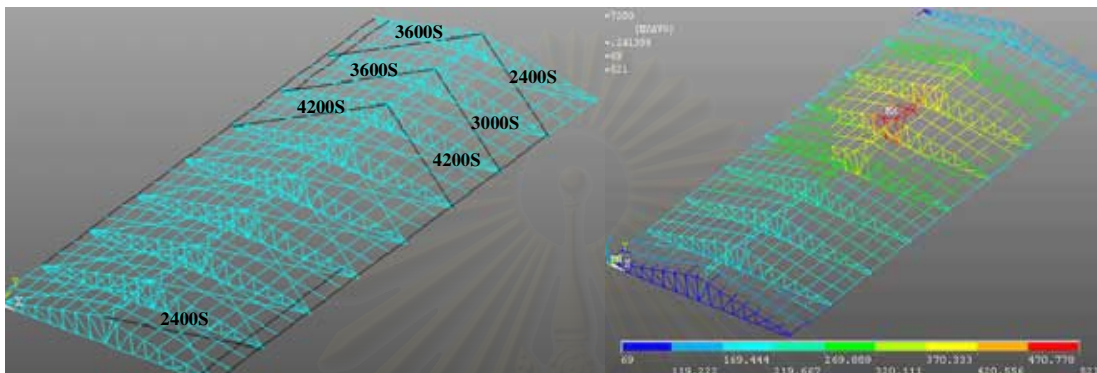


Figure 4.49 The sequence of the failure for the structural members and the temperature distribution of the structure at 7200 seconds for Case II-BHP

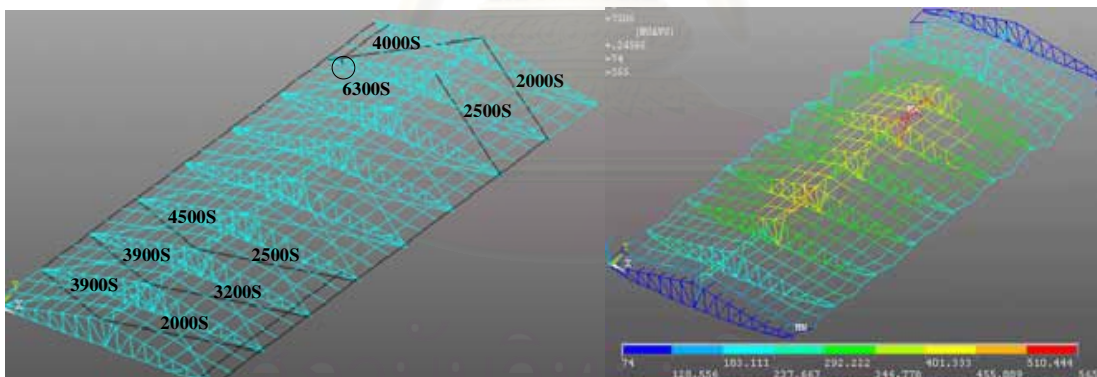


Figure 4.50 The sequence of the failure for the structural members and the temperature distribution of the structure at 7200 seconds for Case II-BLP

### Case III-AHP

In this fire scenario, the ignition source is located between Span 7 and Span 8 on the roller support side of the main roof frames as illustrated in Figure 4.51. The structural analysis results are illustrated in Figures 4.52 and 4.53 in terms of the locations of failure of the roof members and the distribution of temperatures, stresses and bending moments within the roof structure at 700, 800, 1000 and 1200 seconds. The thermal expansions of the main roof frames are similar to Case I-AHP as observed from the relatively low compressive stresses for the main roof frames at the middle of the warehouse. It is found that the bracing members B84 first fail due to thermal expansion followed by B81. Note that the bracing members B73 and B74 can not resist the elongation because they are subjected the high temperature which causes largely relative elongation. Moreover, the P- $\Delta$  effects at the supports of the main roof frame cause member 16 of Span 9 to fail at 1200 seconds.

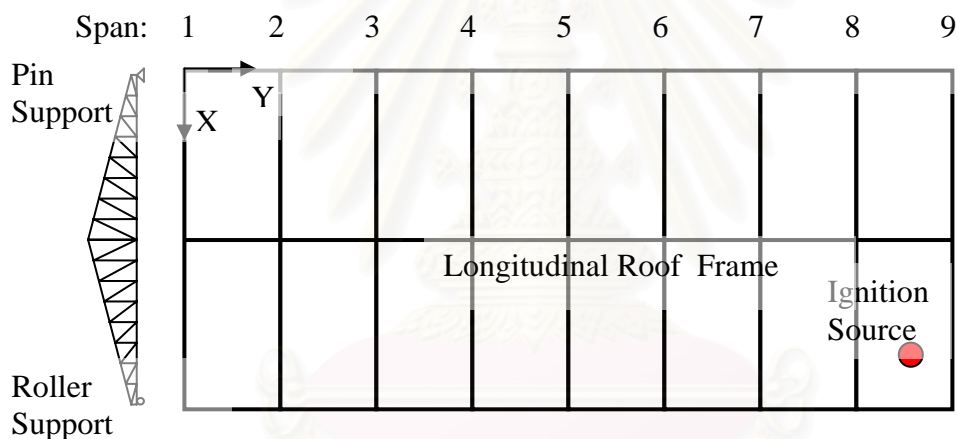


Figure 4.51 Location of the ignition source for Case III-AHP

สถาบันวิทยบริการ  
จุฬาลงกรณ์มหาวิทยาลัย



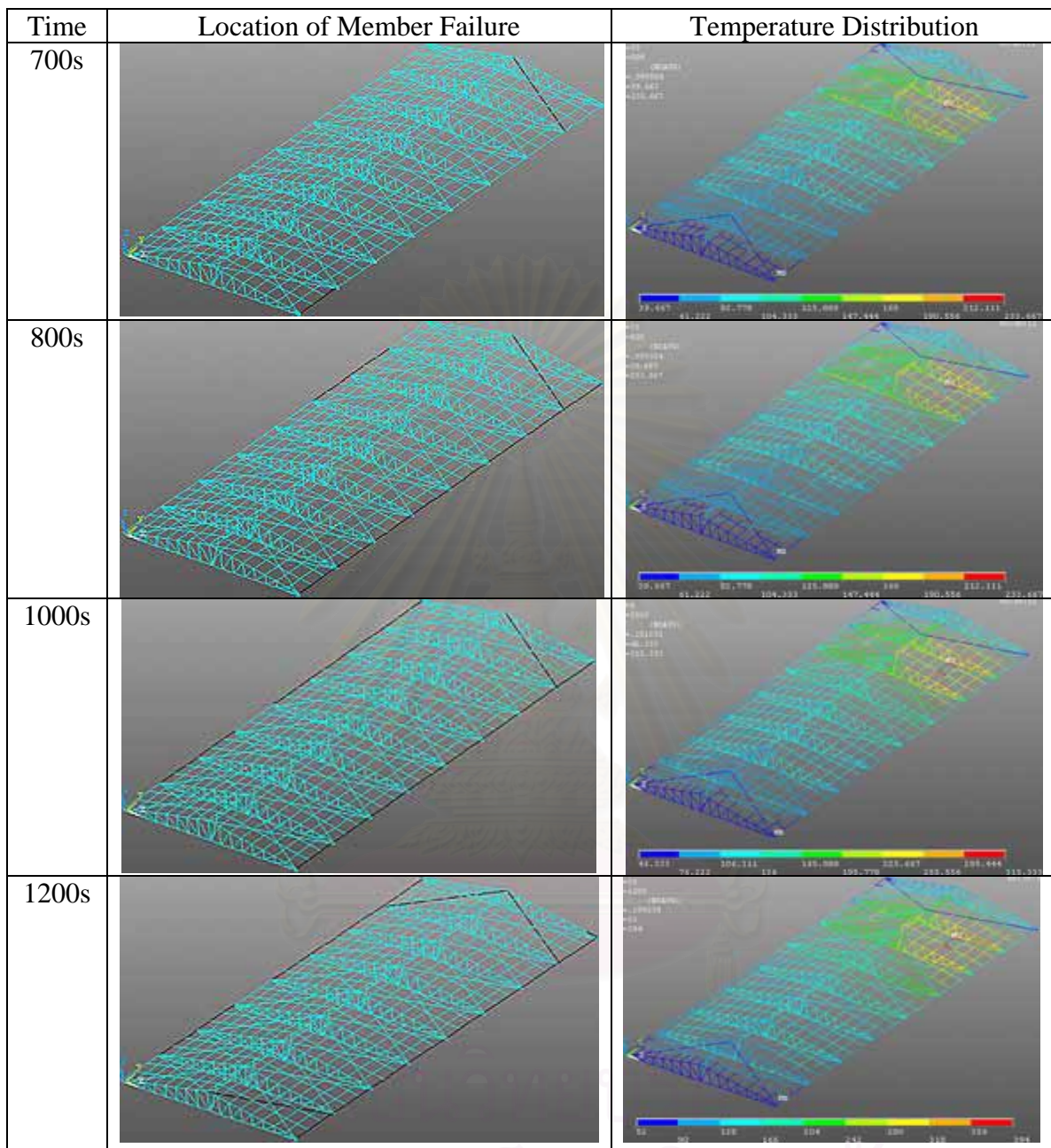


Figure 4.52 Location of member failure and temperature distribution at different time steps for Case III-AHP

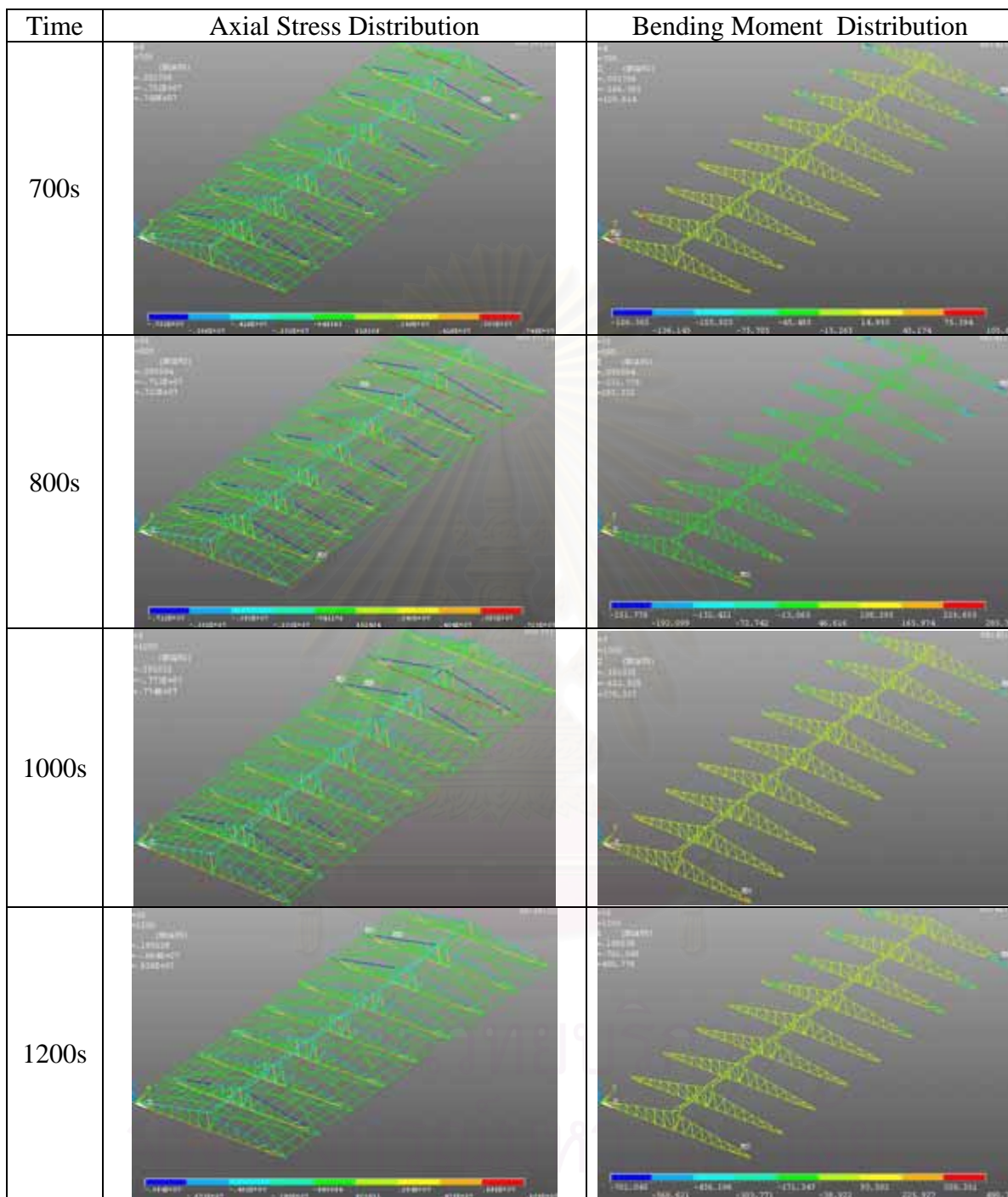


Figure 4.53 Distribution of axial stresses and bending moments at different time steps for Case III-AHP

Similarly results are observed for Cases III-ALP, III-AHU, III-ALU, III-BHU and III-BLU in which the sequence of member failure and the temperature distribution at structural failure are shown in Figures 4.54 to 4.58.

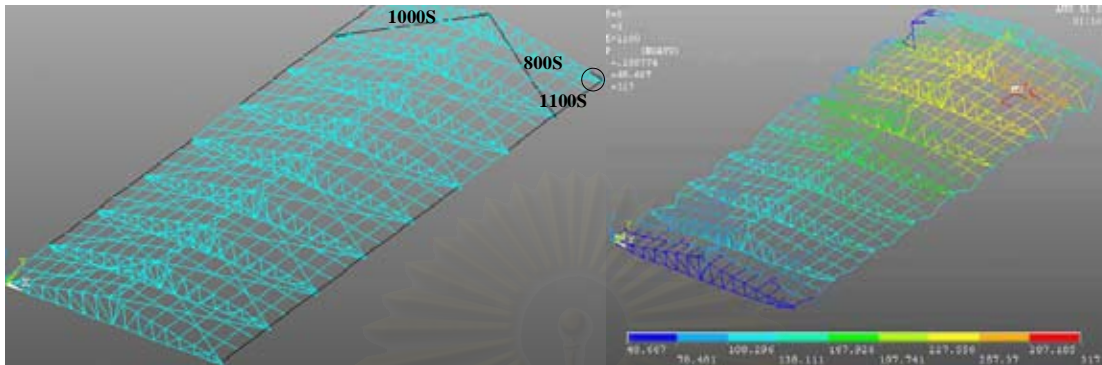


Figure 4.54 Sequence of failure for the structural members and temperature distribution of the structure at failure for Case III-ALP

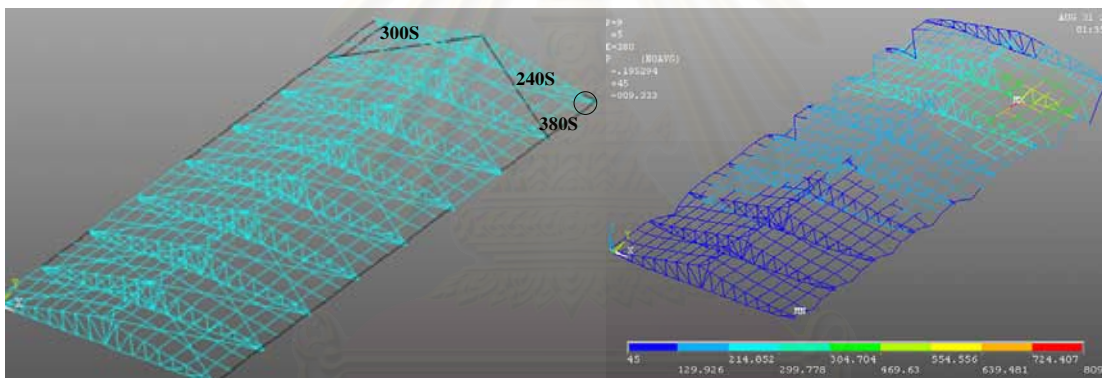


Figure 4.55 Sequence of failure for the structural members and temperature distribution of the structure at failure for Case III-AHU

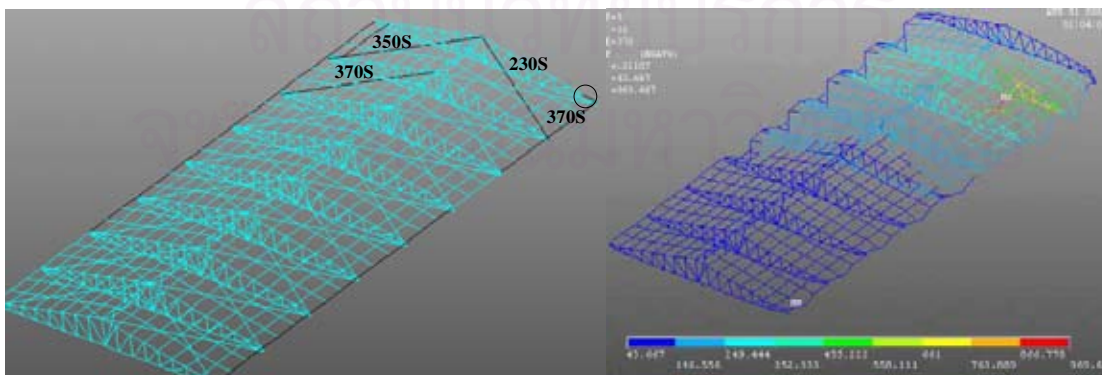


Figure 4.56 Sequence of failure for the structural members and temperature distribution of the structure at failure for Case III-ALU



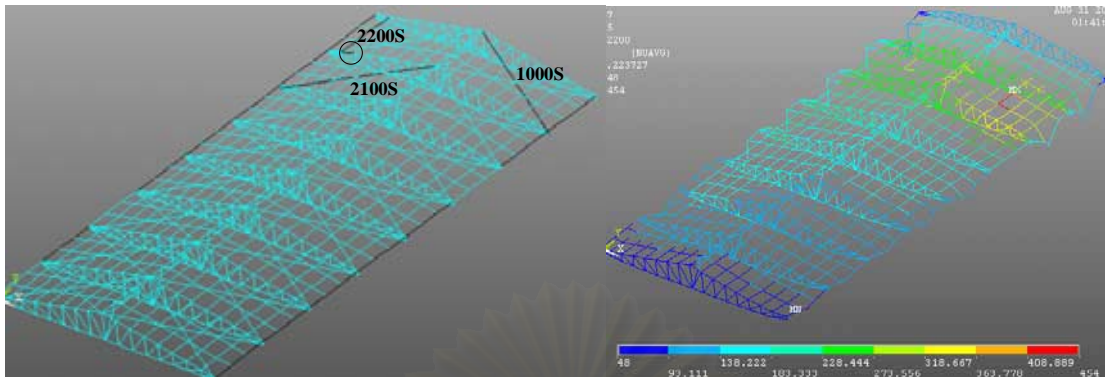


Figure 4.57 Sequence of failure for the structural members and temperature distribution of the structure at failure for Case III-BHU

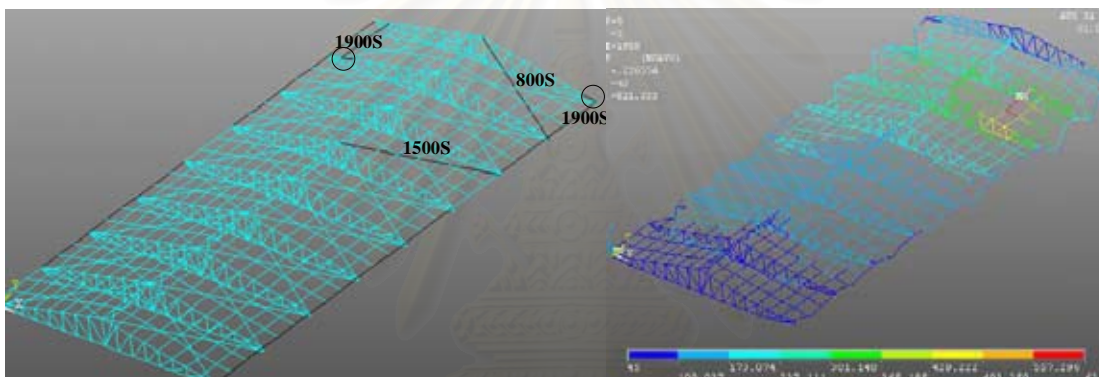


Figure 4.58 Sequence of failure for the structural members and temperature distribution of the structure at failure for Case III-BLU

### Cases III-BHP and III-BLP

The top and bottom chords of the main roof frames do not fail after 7200 seconds burning period and thus the structure is not deemed to fail. The failure time of the structure for these cases is reported as 7200 seconds. The sequence of the failure for the structural members and the temperature distribution of the structure for Cases III-BHP and Case III-BLP are shown in Figures 4.59 and 4.60, respectively.

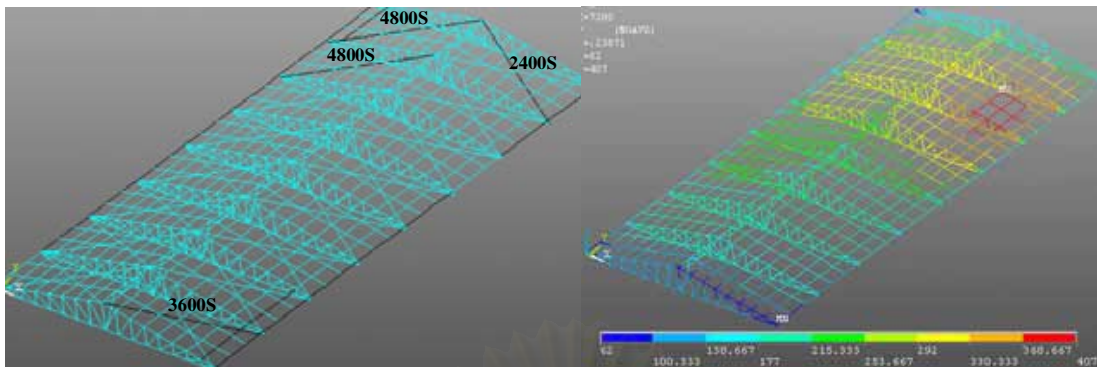


Figure 4.59 The sequence of the failure for the structural members and the temperature distribution of the structure at 7200 seconds for Case III-BHP

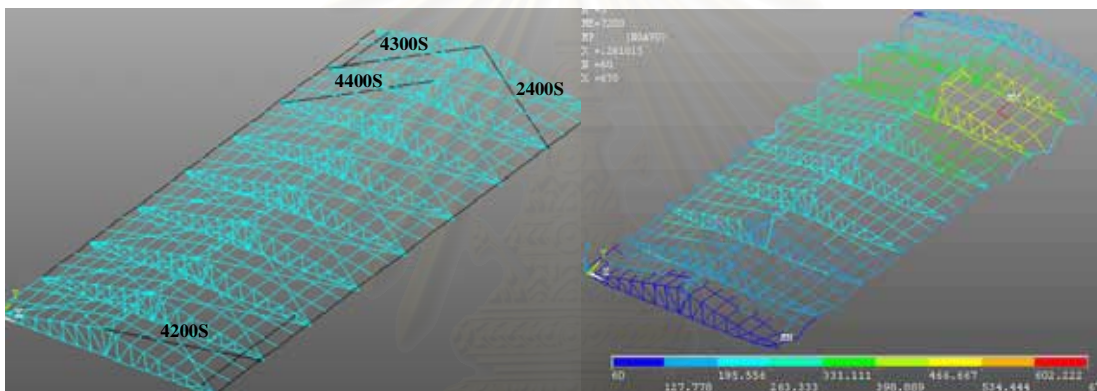


Figure 4.60 The sequence of the failure for the structural members and the temperature distribution of the structure at 7200 seconds for Case III-BLP

สถาบันวิทยบริการ  
จุฬาลงกรณ์มหาวิทยาลัย



### Case IV-AHP

In this fire scenario, the ignition source is located between Span 1 and Span 2 on the pin support side of the main roof frames as illustrated in Figure 4.61. The structural analysis results are illustrated in Figures 4.62 and 4.63 in terms of the locations of failure of the roof members and the distribution of temperatures, stresses and bending moments within the roof structure at 700, 900, 1300 and 1500 second. The thermal expansions of the main roof frames are similar to Case I-AHP as observed from the relatively low compressive stresses for the main roof frames at the middle of the warehouse. Again, it is found that the bracing members B13 first fail due to thermal expansion. The bracing members B21 and B22 can not resist the elongation because they are subjected the high temperature which causes largely relative elongation. Moreover, the  $P-\Delta$  effects at the supports of the main roof frame cause member 1 of Span 1 to fail at 1500 seconds.

Note that Location IV case is similar to Location III case, however Location IV case tends to more time to failure because the sub span of this case directly resists the transverse elongation while the third case, the maximum temperature is located at the pin support side of the main roof frames which free elongate.

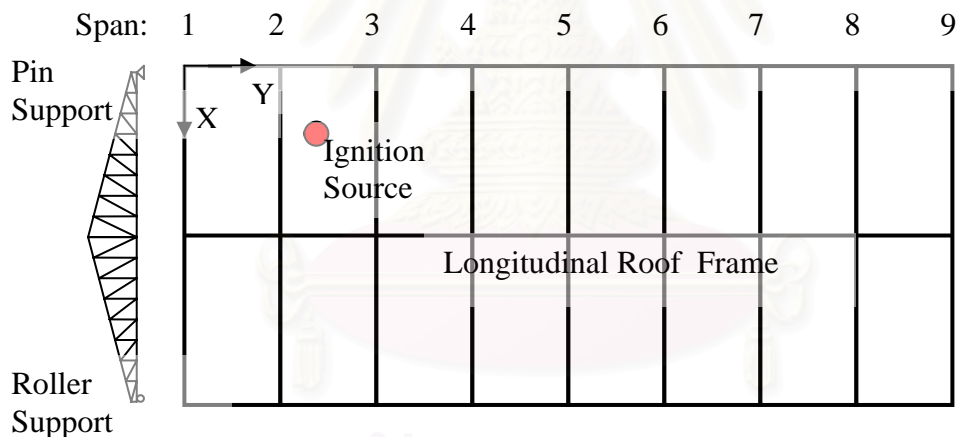


Figure 4.61 Location of the ignition source for Case IV-AHP

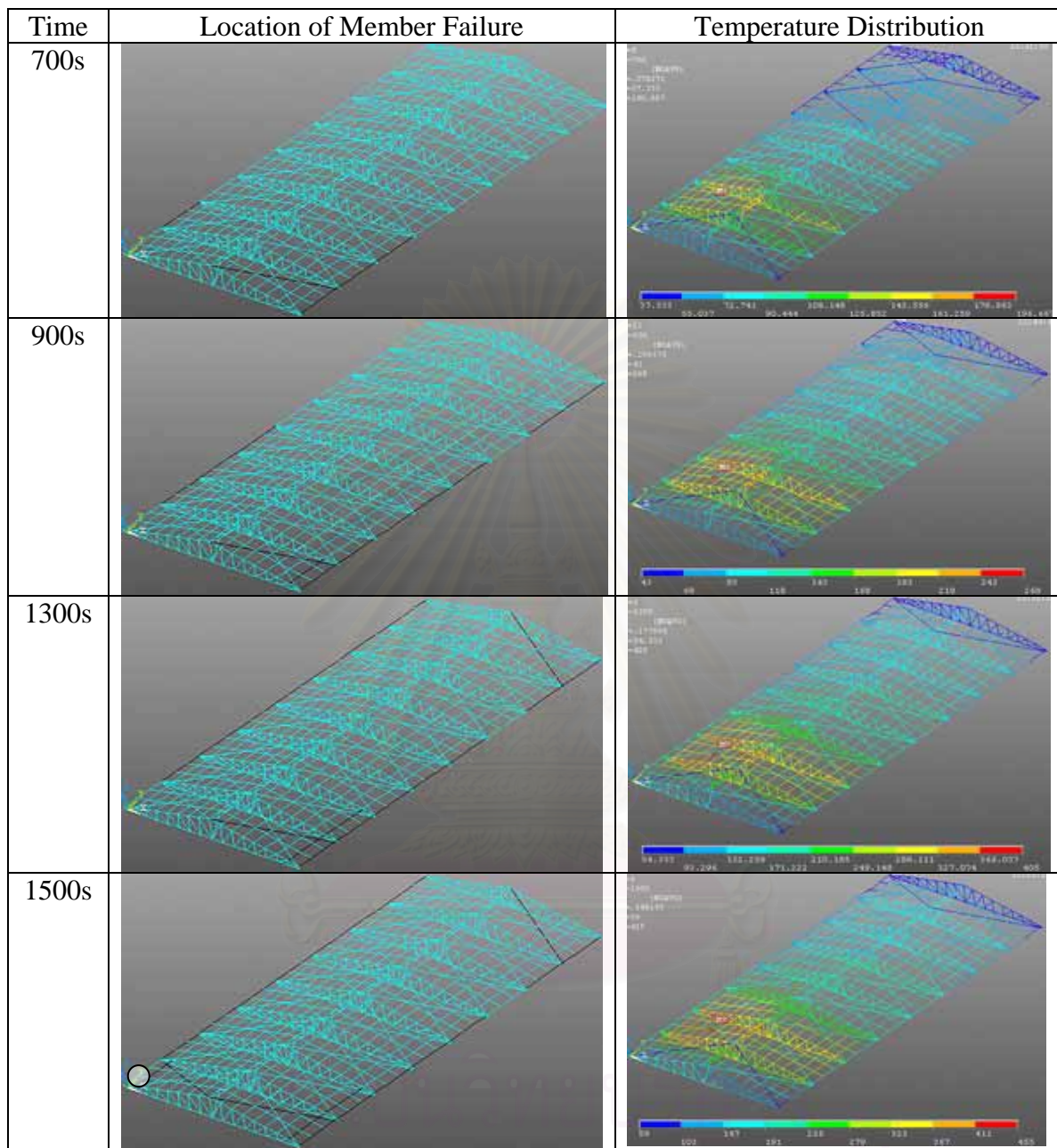


Figure 4.62 Location of member failure and temperature distribution at different time steps for Case IV-AHP

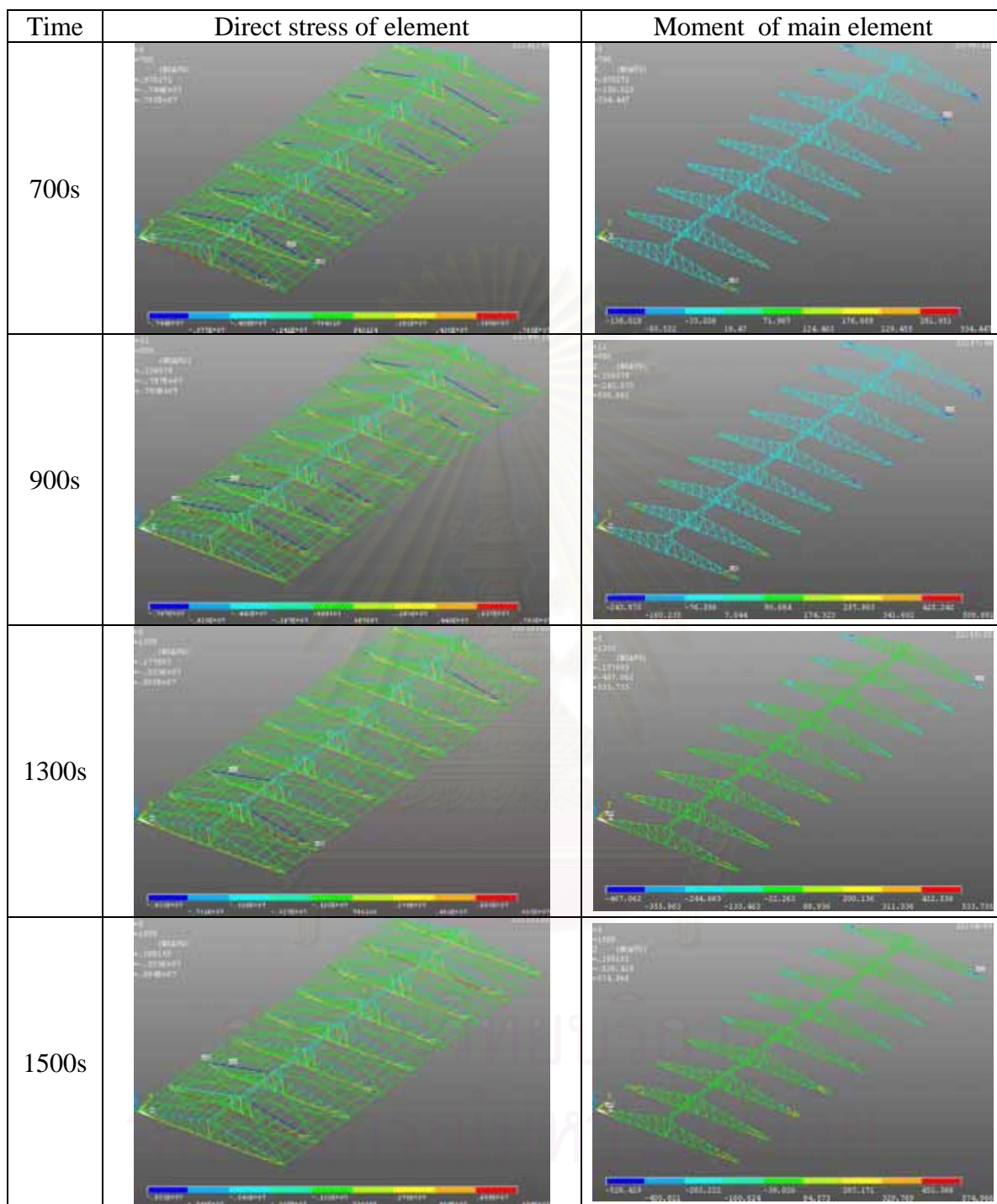


Figure 4.63 Distribution of axial stresses and bending moments at different time steps for Case IV-AHP

Similarly results are observed for Cases IV-ALU, IV-ALP, IV-BHU and IV-BLU in which the sequence of member failure and the temperature distribution at structural failure are shown in Figures 4.64-4.67.

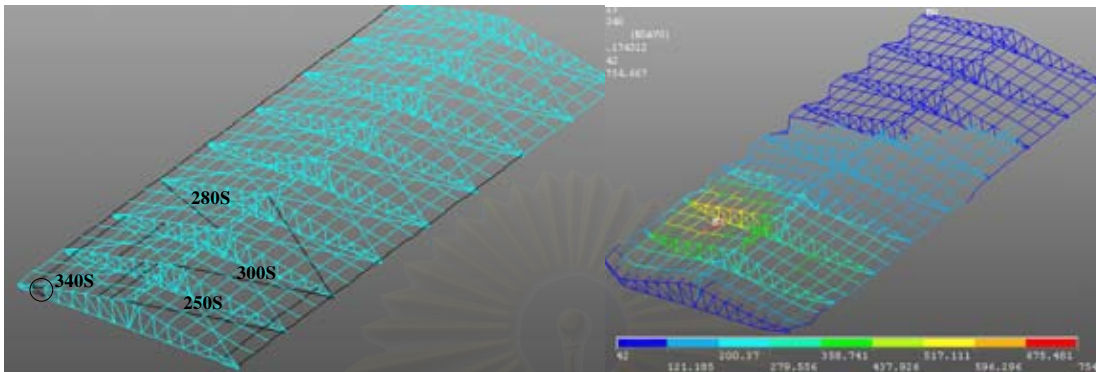


Figure 4.64 Sequence of failure for the structural members and temperature distribution of the structure at failure for Case IV-ALU

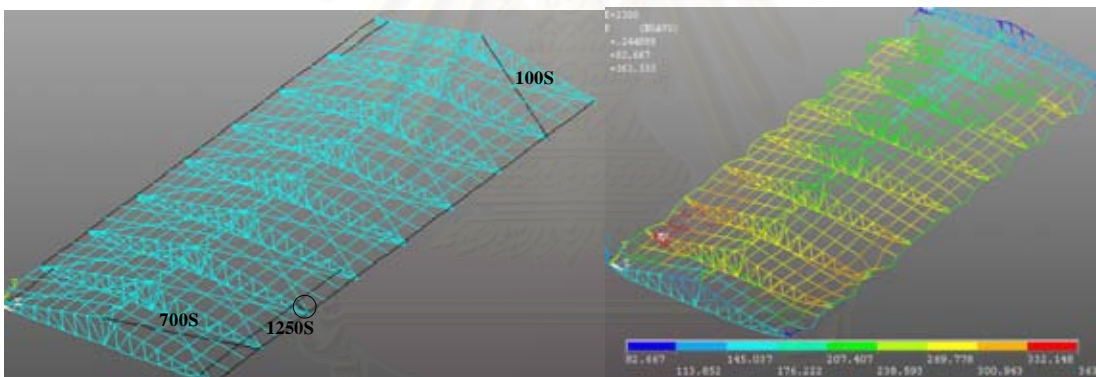


Figure 4.65 Sequence of failure for the structural members and temperature distribution of the structure at failure for Case IV-ALP



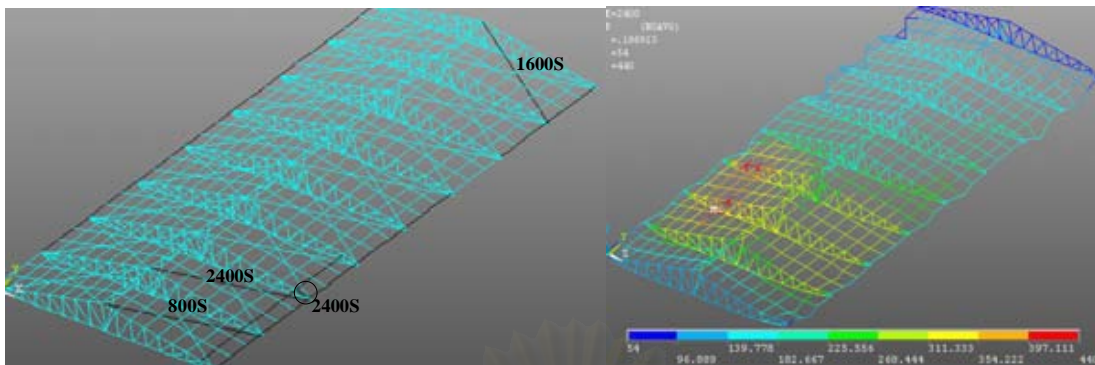


Figure 4.66 Sequence of failure for the structural members and temperature distribution of the structure at failure for Case IV-BHU

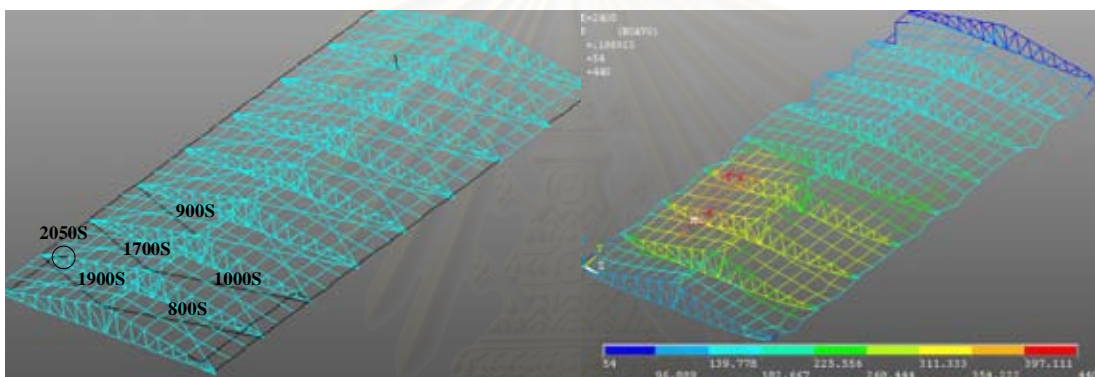


Figure 4.67 Sequence of failure for the structural members and temperature distribution of the structure at failure for Case IV-BLU

#### Case IV-AHU

Because of the rapidly increasing temperature, the mechanical properties of the steel roof frames are expected to drop significantly. In particular, the purlins located between Span 2 and Span 3 on the pin support side of the main roof frames reaches the temperature of over 900 °C at 360 seconds which is over limitation of the analysis, resulting in error of the structural analysis.

#### Cases IV-BHP and IV-BLP

The top and bottom chords of the main roof frames do not fail after 7200 seconds burning period and thus the structure is not deemed to fail. The failure time of the structure for these cases is reported as 7200 seconds. The sequence of the failure for the structural members and the temperature distribution of the structure for Cases IV-BHP and Case IV-BLP are shown in Figures 4.68 and 4.69, respectively.



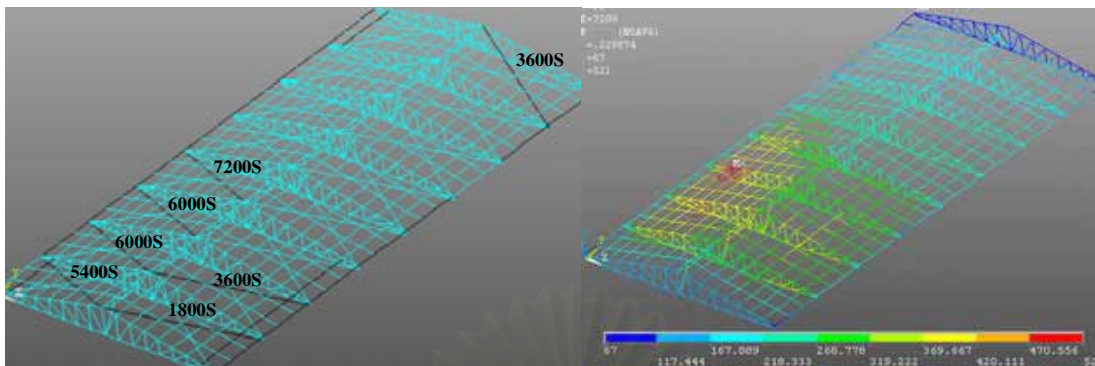


Figure 4.68 The sequence of the failure for the structural members and the temperature distribution of the structure at 7200 seconds for Case IV-BHP

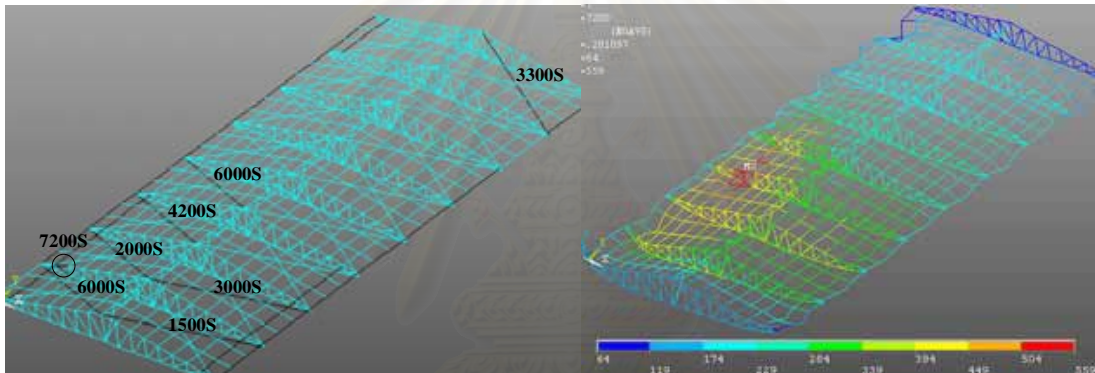


Figure 4.69 The sequence of the failure for the structural members and the temperature distribution of the structure at 7200 seconds for Case IV-BLP

### Summary of Structural Analysis Results

The results obtained from the various fire scenarios are summarized in terms of the structural failure mode and time in Table 4.6. Based on the simulation results, it is found that the fuel type and fire protection of steel roof members significantly affect the time to failure. The scenarios in which the wood fuels are used and the roof members are protected yield considerably longer time to failure compared with the cases in which the plastic fuels are used and the steel is unprotected. The clearance height of the roof structure and the location of the ignition source are considered supplementary factors to the structural failure time. The 10-m clearance height slightly extends the failure time because of a slower feedback of heat from the burning contents. The variation of the location of the ignition source results in different fire and structural behaviors. It is seen that Location I tends to give the longest time to failure compared with the other locations.

In summary, the structural failure is due to three key causes. The first cause is the increasing axial compression due to thermal expansion. The second cause is the significant drop of the mechanical properties of steel due to the increasing temperature. The last is the  $P-\Delta$  effects from the movements of the structure.



สถาบันวิทยบริการ  
จุฬาลงกรณ์มหาวิทยาลัย

Table 4.6 Summary of structural failure mode and time

Case	Failure time (second)	Failure Mode		
		Location Member/ Span	Temperature (°C)	Remarks
I-ALU	380	7/2	600	*
II-ALU	330	9/6	610	*
III-ALU	370	16/9	70	**
IV-ALU	340	2/1, 18/1	80	**
I-AHU	400	8/2	650	*
II-AHU	380	16/8	150	**
III-AHU	380	16/9	160	**
IV-AHU	-	-	-	***
I-ALP	1200	16/2	250	**
II-ALP	1150	16/3	240	**
III-ALP	1100	16/9	130	**
IV-ALP	1250	16/3	280	**
I-AHP	1300	16/3	340	**
II-AHP	1150	16/1	240	**
III-AHP	1200	16/9	130	**
IV-AHP	1500	2/1	120	**
I-BLU	4,200	2/2	380	**
II-BLU	1,750	2/8	270	**
III-BLU	1,900	16/9, 2/8	200,270	**
IV-BLU	2,050	15/1	150	**
I-BHU	>7200	-	-	-
II-BHU	2,000	2/9	90	**
III-BHU	2,200	2/8	250	**
IV-BHU	2,400	16/3	280	**
I-BLP	>7200	-	-	-
II-BLP	>7200	-	-	-
III-BLP	>7200	-	-	-
IV-BLP	>7200	-	-	-
I-BHP	>7200	-	-	-
II-BHP	>7200	-	-	-
III-BHP	>7200	-	-	-
IV-BHP	>7200	-	-	-

\* Significant drop of steel mechanical properties  
\*\* Significant P-Δ effect  
\*\*\* Analysis error

## CHAPTER V

### CONCLUSIONS

Various fire scenarios are simulated in the current study to investigate the behavior of the steel roof structure for a typical warehouse. The location of the ignition source, the fuel type and the clearance height of the roof structure are taken as the varying parameters. The different fire scenarios are modeled using the FDS program and the behavior of the steel roof frames is examined through nonlinear finite element analysis.

Based on the fire modeling results, it is found that the fuel types significantly affect the behavior of the modeled fire in terms of the fire growth and the spread of flames. The plastic contents result in a rapid fire growth as well as a localized flashover due to the significant feedback of heat from the flames. The wood contents result in a considerably slower fire growth that occurs through direct radiation from the flames to nearby objects. On the other hand, the clearance height of the roof and the location of the ignition source are found to have slight effects on the fire behavior.

Through the use of the simulation study, various aspects of the structural behavior under fire are observed. The failure of the roof structure is due to three key factors: the increasing axial compression due to thermal expansion; the significant drop of the mechanical properties of steel due to the increasing temperature; and the  $P-\Delta$  effects from the movements of the structure. In addition, the failure time of the roof structure depends upon the fuel type and whether or not the roof members are protected from fire. The highest risk is found for the cases of plastic storage contents without fire protection for the steel roof frame members.

It should be noted that even though the proposed approach may be used as a framework for fire risk assessment of steel structures in accordance with the fire safety regulations. Further studies should be conducted to verify the assumptions adopted as well as to overcome the limitations of the proposed procedure.

## REFERENCES

- Anchor, R.D., Malhotra H.L., Purkiss, J.A. (1986) Design of Structures Against Fire. London : Elsevier Applied Science Publishers, Great Britain.
- ANSI/AISC 360-05. (2005). Specification for Structural Steel Buildings, American, Chicago: Institute of Steel Construction.
- ANSYS (2001) Theory Manual, version 5.7.
- ASTM. (2001). Standard Test Methods For Fire Tests of Building Construction and Material, ASTM E119. West Conshohocken, PA.: American Society of Testing and Materials.
- Brockenbrough, R.L. (1970). Theoretical stresses and strains from heat curving. Journal of Structural Division, American Society of Civil Engineers, 96, ST7.
- Buchanan, A.H. (1999). Structural Design for Fire Safety. New Zealand: University of Canterbury.
- CIB W14. (1986). Design Guide: Structural Fire Safety. Fire Safety Journal,10,2.
- EC3. (1995). Design of Steel Structures. ENV 1993-1-2: General Rules– Structural Fire Design. Brussels: European Committee for Standardisation.
- ECCS. (1983). European Recommendations for the Fire Safety of Steel Structures, Calculation of the Fire Resistance of Load Bearing Elements and Structural Assemblies Exposed to Standard Fire. Elsevier, Brussels: European Commission for Constructional Steelwork.
- ECCS. (1985). Design Manual on the European Recommendations for the Fire Safety of Steel Structures. Elsevier, Brussels: European Commission for Constructional Steelwork.
- Elliot, D.A. (1981). Protection of Structural Steelwork. England: Constrado
- Feeney, M.J. (1998). Design of Steel Framed Apartment and Hotel Buildings for Fire. Australasian Structural Engineering Conference
- Forney, G.P. and McGrattan, K.B. (2003). User's Guide for Smokeview Version 3.1, Technical Report NISTIR 6980. Gaithersburg, Maryland: National Institute of Standards and Technology
- Franssen, J.M., Schleich, J.B.,Cajot, L.G., Azpiazu, W. (1996). A Simple Model for the Fire Resistance of Axially Loaded Members – Comparison with Experimental Results. Journal of Constructional Steel Research, 37,3:175-204.
- Gamble, W.L. (1989). Predicting Protected Steel Member Fire Endurance Using Spread-Sheet Programs. Fire Technology, 25,3: 256-273.
- Gilvery, K.R., Dexter, R.J. (1997). Evaluation of Alternative Methods for FireRating Structural Elements, NIST-GCR-97-718. Gaithersburg, Maryland: National Institute of Standards and Technology.



- Gorenc, B., Tinyou, R., Syam, A. (1996). *Steel Designers Handbook*, 6th Edition. Sydney, Australia: UNSW Press
- Huggett, C. (1980). Estimation of the Rate of Heat Release by Means of Oxygen Consumption Measurements, *Fire and Materials*, 4: 61–65.
- Lie, T.T. (1992). *Structural Fire Protection*, American Society of Civil Engineers. Manual of Practice No.78.
- Lewis, K. R. Lewis. (2000). *Fire Design of Steel Members*. Christchurch, New Zealand: University of Canterbury.
- Martin, L.H., Purkiss, J.A. (1992). *Structural Design of Steelwork to BS 5950*. Huddersfield, Great Britain: Edward Arnold
- Milke, J.A. (1999). Performance-Based Analysis of Fire Resistance of Construction Assemblies, Proceedings – Third International Conference on Fire Research and Engineering, Society of Fire Protection Engineers. Bethesda, MD, USA.
- Mcgrattan, K.B., Baum, H.R., Rehm, R.G., Forney G.P. Floyd J.E., Prasad K., and Hostikka S. (2002). *Technical Reference Guide for Fire Dynamics Simulator Version 3.*, Technical Report NISTIR 6783, 2002 Edition. Gaithersburg, Maryland: National Institute of Standards and Technology.
- Melinek S.J.(1989). Prediction of the Fire Resistance of Insulated Steel. *Fire Safety Journal*, 10: 127-134.
- Melinek S.J., Thomas P.H. (1987). Heat Flow to Insulated Steel. *Fire Safety Journal*, 12: 1-8.
- Quintiere, J.G., Marzo, M. and Becker, R. A. (2002). Suggested cause of the induced collapse of the World Trade Towers. *Fire Safety Journal*, 37: 707–716.
- Rehm, R.G. and Baum, H.R. (1978). The equations of motion for thermally driven, buoyant flows. *Journal of Research of the NBS*, 83: 297–308.
- RadCal, W. Grosshandler. (1993). *A Narrow Band Model for Radiation Calculations in a Combustion Environment*, NIST Technical Note (TN 1402). Gaithersburg, Maryland: National Institute of Standards and Technology.
- Sakumoto, Y., Nishigaki, T. and Kohno, M., (2002). *Fire resistance of steel Frame.*, Tsukuba, Japan: Building Research institute.
- Stanzak, W.W. (1990). *Structural Fire Protection – an Engineering Approach* Technical Paper 377. Canada: National Research Council of Canada
- Troitzsch, J. (2004). *Fire tests of the roofing system for the Passenger Terminal Building of the Suvarnabhumi Airport*, Expert Opinion No.: 04-05, Hightex Engineering GmbH.



**APPENDIX: FDS RESULTS**

สถาบันวิทยบริการ  
จุฬาลงกรณ์มหาวิทยาลัย

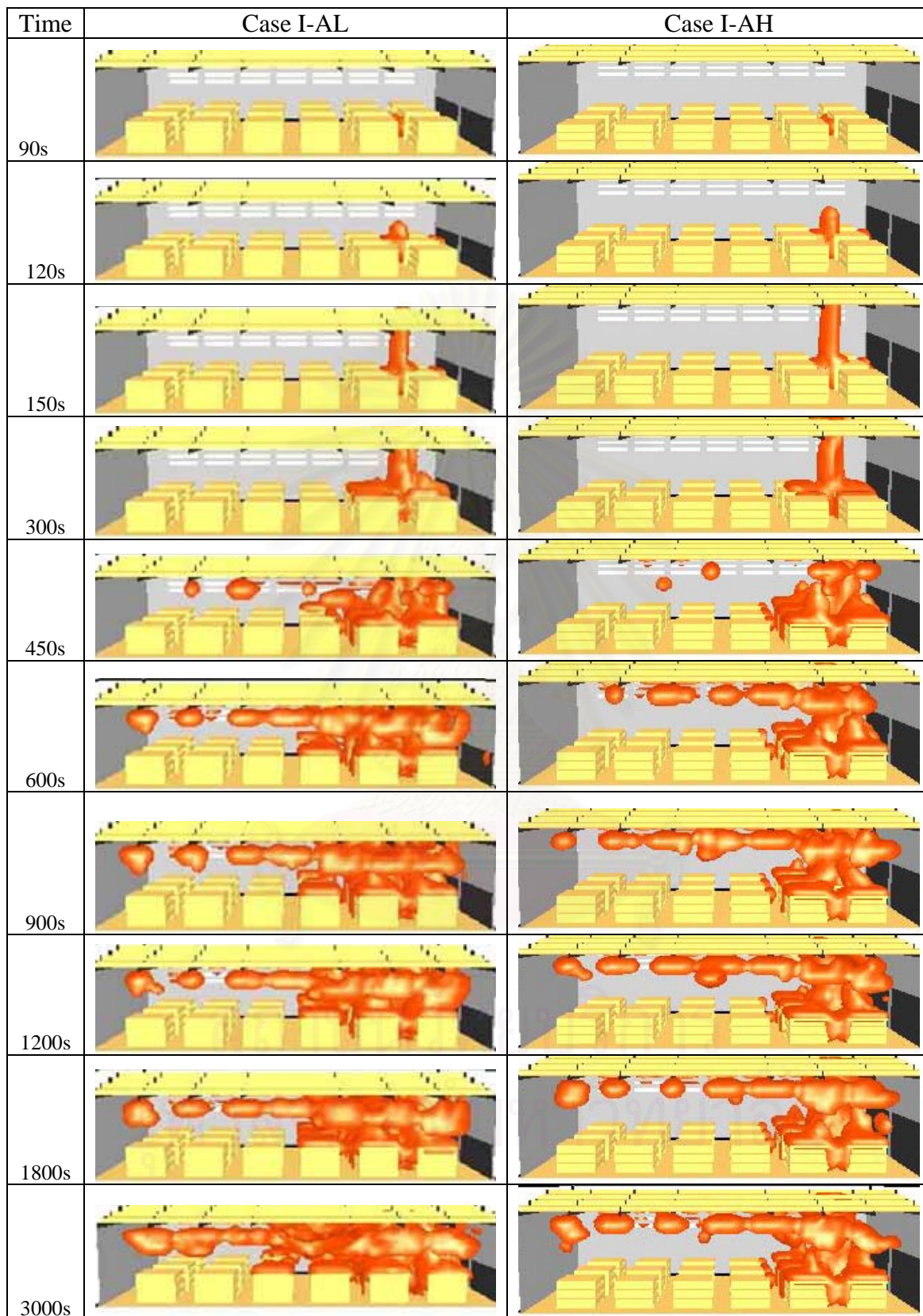


Figure A-1 FDS modeled fire at different time steps for Case I-AL and Case I-AH



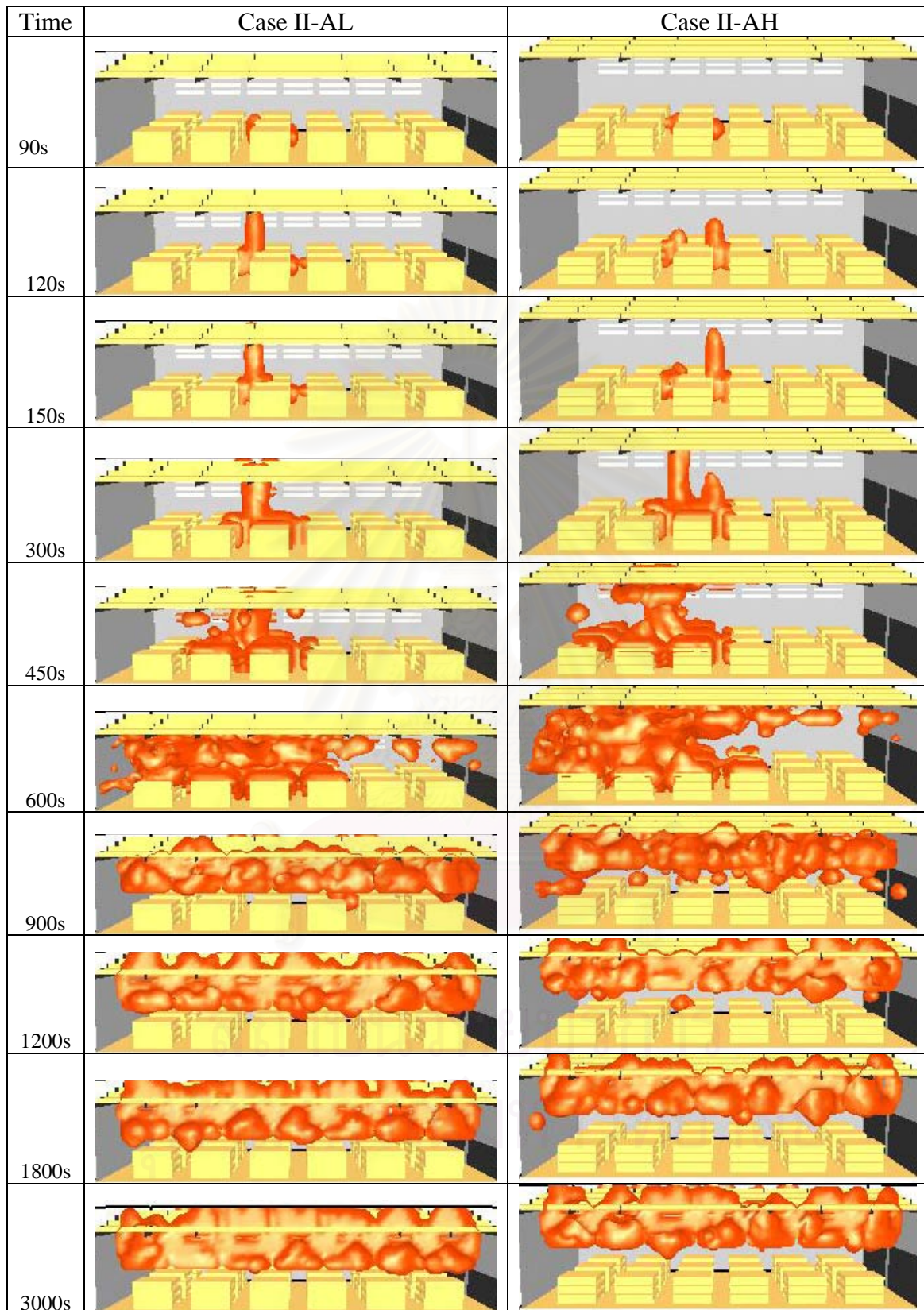


Figure A-2 FDS modeled fire at different time steps for Case II-AL and Case II-AH

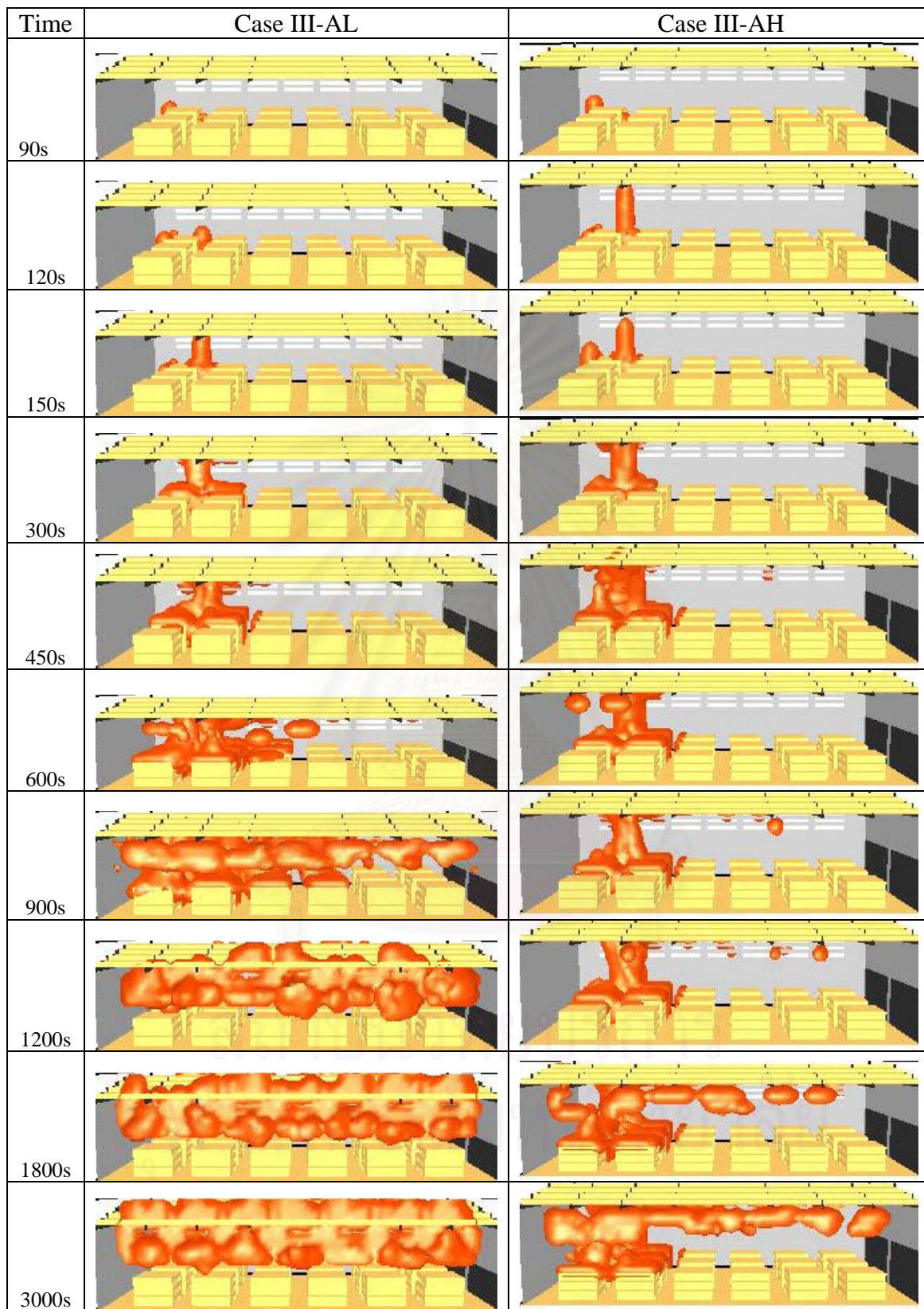


Figure A-3 FDS modeled fire at different time steps for Case III-AL and Case III-AH



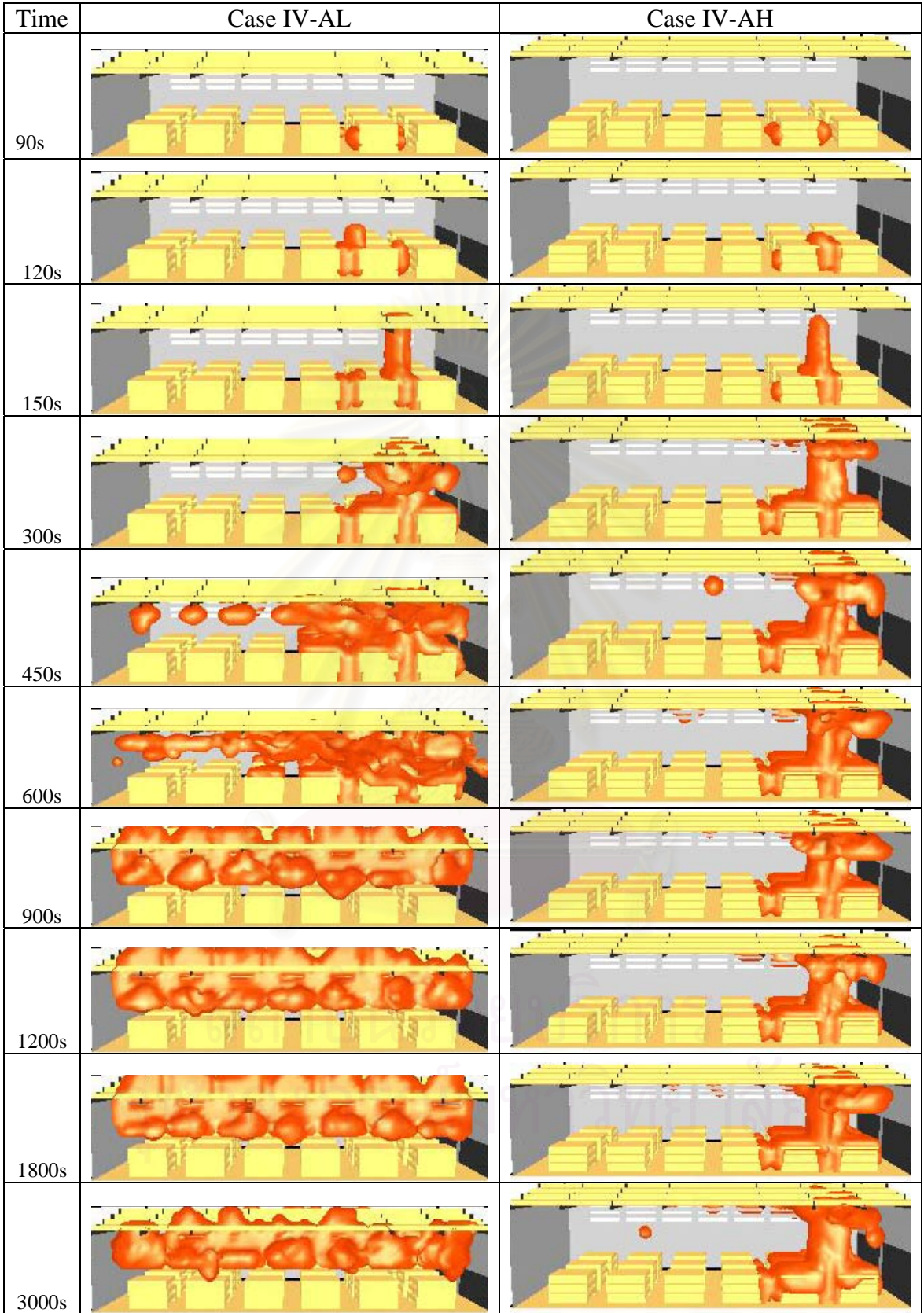


Figure A-4 FDS modeled fire at different time steps for Case IV-AL and Case IV-AH

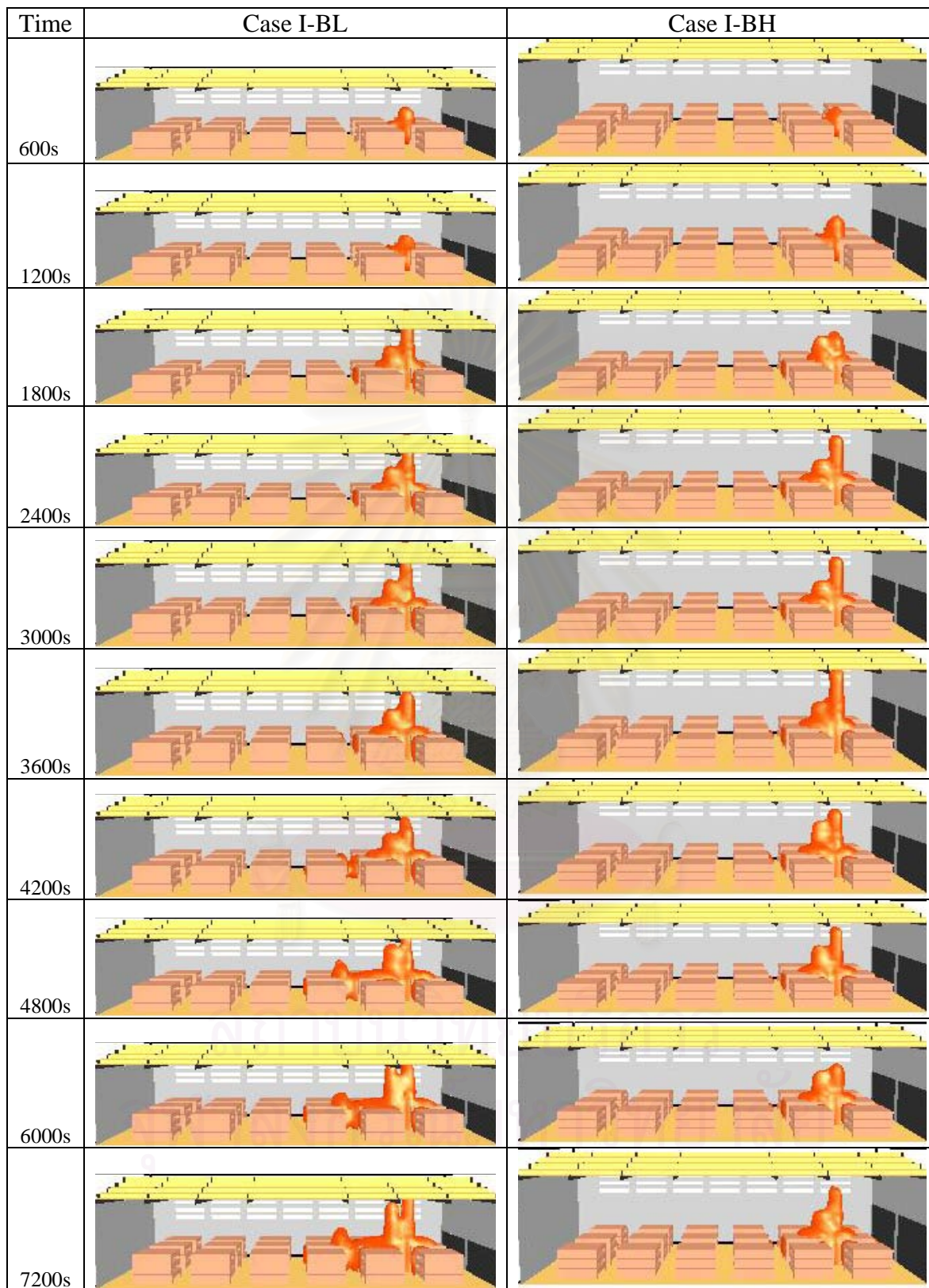


Figure A-5 FDS modeled fire at different time steps for Case I-BL and Case I-BH



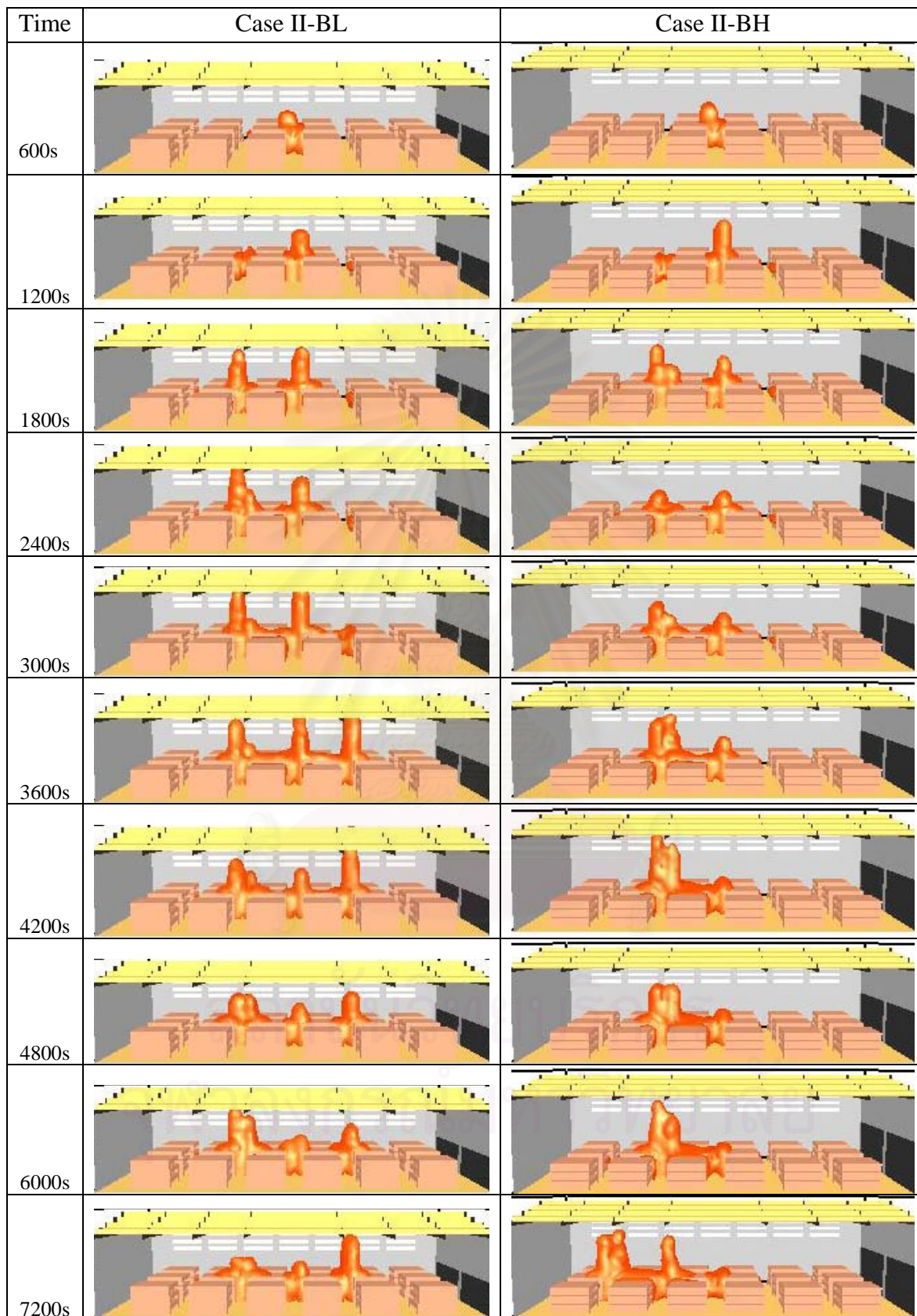


Figure A-6 FDS modeled fire at different time steps for Case II-BL and Case II-BH

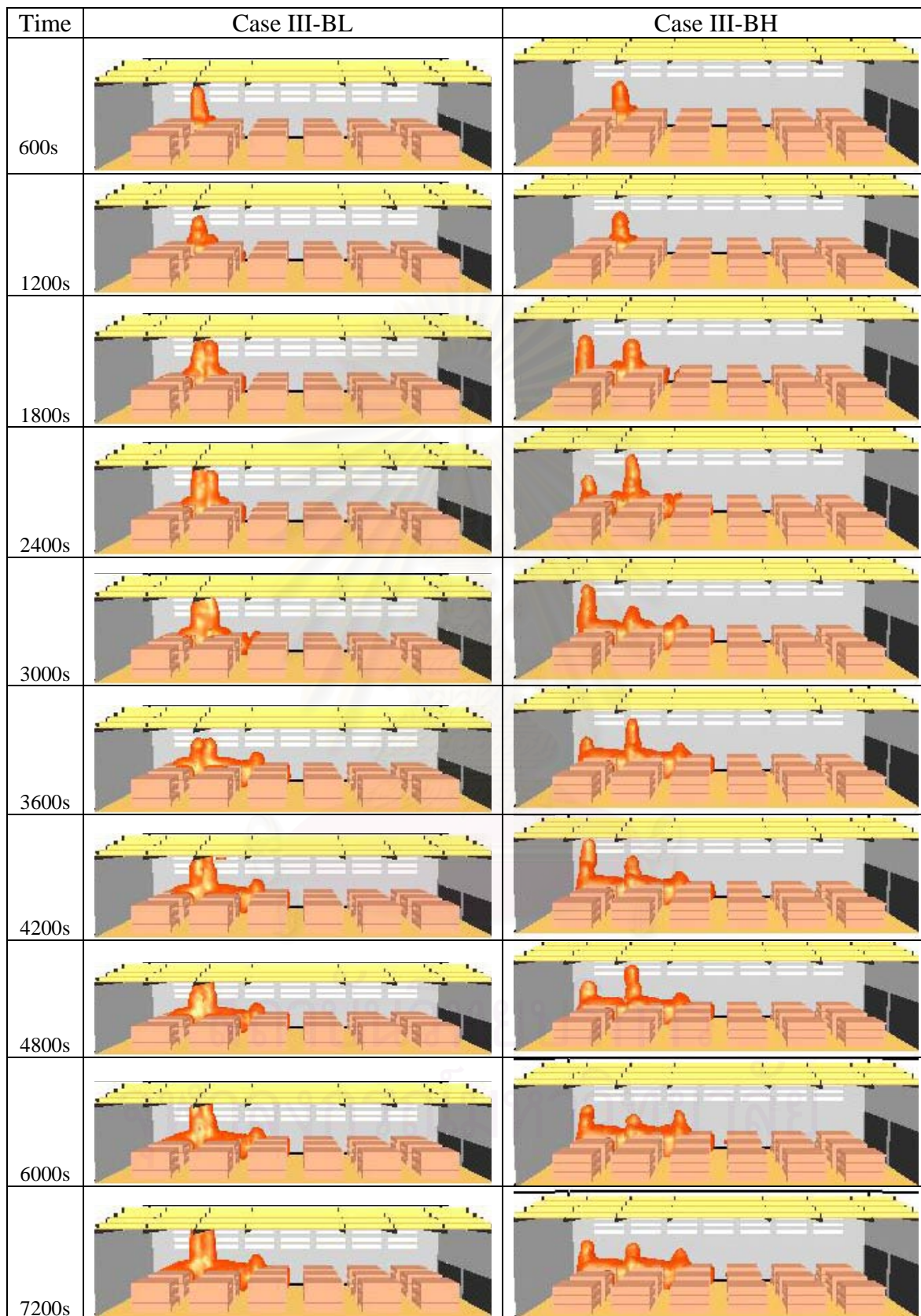


Figure A-7 FDS modeled fire at different time steps for Case III-BL and Case III-BH



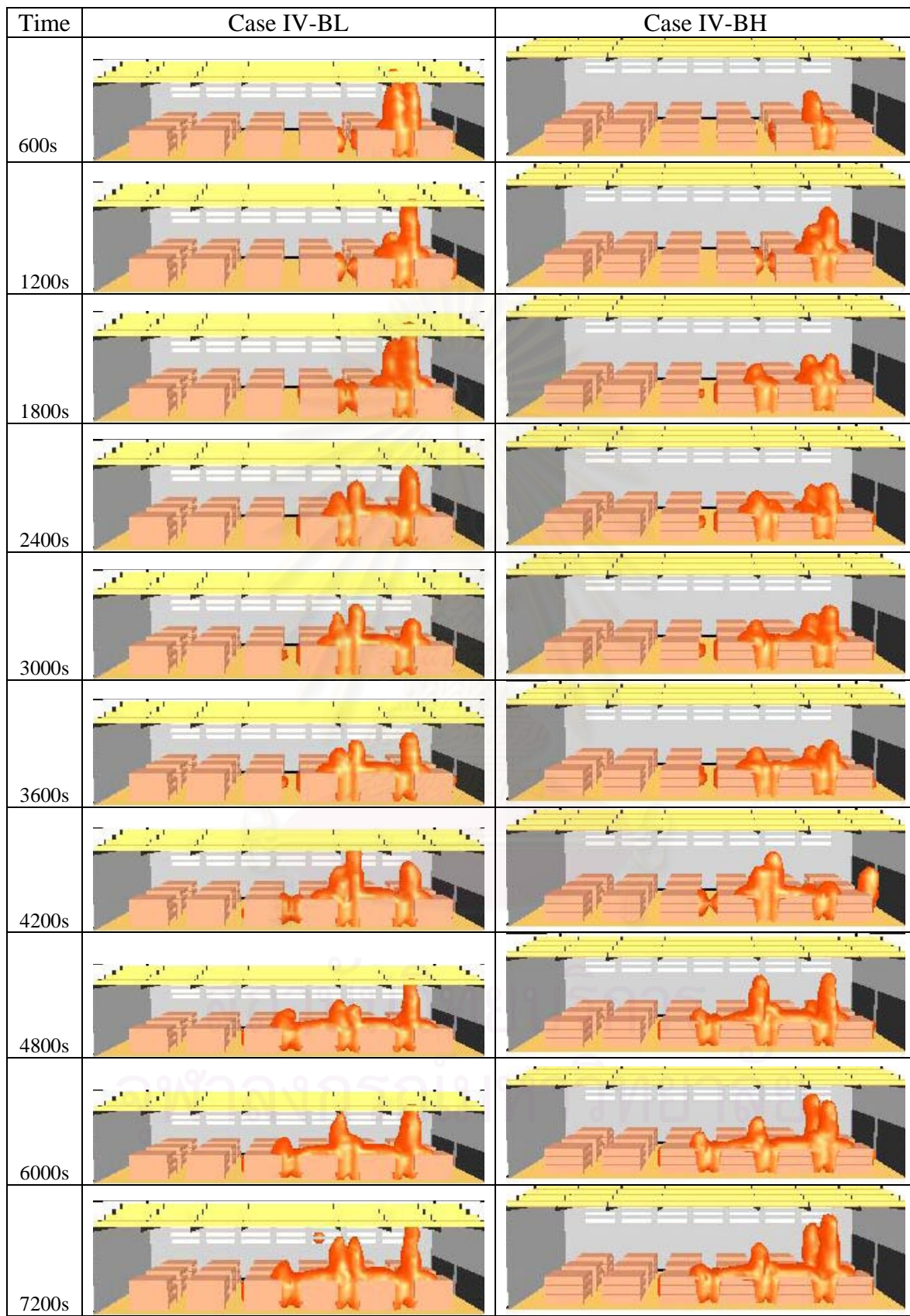


Figure A-8 FDS modeled fire at different time steps for Case IV-BL and Case IV-BH



**VITA**

Mr. Pattamad Panedpojaman was born in Songkhla in 1980. He graduated from the Faculty of Engineering, King Mongkut's Institute of Technology Ladkrabang in 2002. He continued his study for the Master of Engineering degree in Civil Engineering at Chulalongkorn University in 2003.



สถาบันวิทยบริการ  
จุฬาลงกรณ์มหาวิทยาลัย